String-net models in condensed matter systems



Curt William von Keyserlingk

St John's College

University of Oxford

A thesis submitted for the degree of

Doctor of Philosophy

Trinity 2014

String-net models in condensed matter systems

Curt William von Keyserlingk

St John's College
University of Oxford

A thesis submitted for the degree of
Doctor of Philosophy

Trinity 2014

We study a class of three dimensional exactly solvable models of topological matter first put forward by Walker and Wang. While these are not models of interacting bosons or fermions, they may well capture the topological behaviour of some strongly correlated systems.

In this work we give a full pedagogical treatment of a special simple case of these models, which we call the 3D semion model: We calculate its ground state degeneracies for a variety of boundary conditions, and classify its low-lying excitations. While point defects in the bulk are confined in pairs connected by energetic strings, the surface excitations are more interesting: the model has deconfined point defects pinned to the boundary of the lattice, and these exhibit semionic braiding statistics. The surface physics is reminiscent of a $\nu = 1/2$ bosonic fractional quantum Hall effect in its topological limit. Our special example of the 3D semion model captures much of the behaviour of more general 'confined Walker-Wang models'. We contrast the 3D semion model with the closely related 3D version of the toric code (a lattice gauge theory) which has deconfined point excitations in the bulk. We discuss how more general Walker-Wang models can have a combination of fermionic or bosonic deconfined excitations in the bulk, and excitations which are deconfined on the surface but confined in the bulk.

Having classified the spectra and surface properties of a number of these models, we construct a topological field theory which describes a subset of them exactly. Moreover, we argue that some Walker-Wang models capture the low-energy long-wavelength behaviour of certain gapped phases of axion electrodynamics which, in turn, are believed to be germane to certain condensed matter systems with strong spin-orbit coupling.

Acknowledgements

I am immensely grateful to my supervisor Steve Simon. In addition to sharing his great insight, he has always been available when I have needed his sound advice. I would also like to thank Fiona Burnell for her guidance, and for teaching me so much about our field.

I have benefitted enormously from collaborations with Gareth Conduit, Frank Pollmann and Siddhardh Morampudi. I am also indebted to Max Metlitski, Duncan Haldane, John Chalker, Fabian Essler, Xiao-Liang Qi, Simon Davenport, Zohar Ringel, Eliot Kapit, Neil Robinson, Fenner Harper, Thomas Scaffidi and especially Adam Nahum for useful conversations and interesting questions.

This thesis is dedicated to my late father, Curt Edward Arthur von Keyserlingk.

Relation to preprints and publications

Chapter 2 is based on published work [1]. Chapter 3 is based on the preprint [2], along with parts of the published work [3].

Contents

1 Introduction **1**

1.1 Topological order in 2D and Levin-Wen Lattice models 2

1.1.1 The toric code 4

1.1.1.1 Ground States 4

1.1.1.2 Excitations 8

1.1.1.3 Graphical representation of operators as strings . . . 9

1.1.2 The doubled semion model 10

1.1.2.1 Ground States 13

1.1.2.2 Excitations 14

1.2 This thesis 16

2 Walker-Wang models **18**

2.1 Introduction 18

2.2 Simple 3D topological lattice models on closed manifolds 21

2.2.1 The 3D toric code 21

2.2.1.1 Ground states of the toric code on $\mathbb{T}^3$ 22

2.2.1.2 Excitations in the toric code 23

2.2.2 The 3D semion model 27

2.2.2.1 Ground state of 3D semion model on $\mathbb{T}^3$ 27

2.2.2.2 Bulk excitations in the 3D semion model 31

2.2.2.3 Connection between confinement and non-degeneracy 33

2.3 3D topological lattice models on manifolds with boundary 34

2.3.1 The toric code on the solid doughnut 35

2.3.1.1 Excitations 35

2.3.2 The 3D semion model on the solid doughnut 36

2.3.2.1 Surface excitations in the 3D semion model on a manifold with boundary 38

2.3.2.2 Other boundary conditions 39

2.4 General Walker-Wang models 41
2.4.1 The general Walker-Wang Hamiltonian, and excitations 41
2.4.1.1 Hamiltonians 42
2.4.1.2 3DSem in the more general language 45
2.4.2 Modular tensor categories and excitations 45
2.4.3 Confined Walker-Wang models on various manifolds 48
2.4.3.1 The 3-torus 49
2.4.3.2 The solid doughnut $D^2 \times S^1$ 51
2.5 Connection to models with surface quantum Hall anyons 51
2.5.1 Bosonic $\nu = 1/2$ surface Hall state 53
2.5.2 Fermionic $\nu = 1/3$ surface Hall state 53
2.5.2.1 Excitations of the $\mathbb{Z}_3^{(2)} \times \mathbb{Z}_2^{(1)}$ model 55
2.5.2.2 The $\mathbb{Z}_3^{(2)} \times \mathbb{Z}_2^{(1)}$ model on the 3-torus 56
2.5.2.3 The $\mathbb{Z}_3^{(2)} \times \mathbb{Z}_2^{(1)}$ model on the solid doughnut 57
2.5.2.4 More general surface quantum hall states 58
2.6 Conclusion 58

3 Walker-Wang models and axion electrodynamics 60
3.1 Dyon condensed phases of U(1) electrodynamics with a theta term . 62
3.1.1 Gapped phases and condensation 64
3.1.2 Physics in the dyon condensed phases 67
3.1.2.1 k even, $p = k$ 68
3.1.2.2 k odd, $p = 2k$ 68
3.1.3 An effective topological action for the dyon condensed phases 71
3.1.4 Walker-Wang models 72
3.2 Discrete $bF + bb$ theories and Walker-Wang models 73
3.2.1 Topological gauge theory on the lattice 74
3.2.2 Hamiltonian for $bF + bb$ theory for $k = 1, p = 2$ 76
3.3 A case study: Relating the $k = 1, p = 2$ dyon condensate to the fermionic toric code. 79
3.3.1 Ground states 80
3.3.2 Excitations 80
3.3.3 Connection to $k = 1, p = 2$ dyon condensate degrees of freedom 82
3.3.4 Connection to wave function of bosonic topological insulators 83
3.4 Deconfined surface anyons at the boundary between confining phases 85
3.5 Discussion and conclusions 87

4 Conclusions **89**

A Appendices for Chapter 2 **92**

A.1 MTC's are non-degenerate on manifolds without boundary 92

A.2 All string operators are confined in MTC's 94

A.3 Explicit forms for operators in the 2D DSem model 97

A.3.1 String operators, and their endpoints. 99

A.4 Topological entanglement entropy in 3DSem 100

A.5 Surface plaquette operators of the 3D semion model with rough boundary 105

A.6 Trace methods 106

A.6.1 2D ground state degeneracies via trace method 106

A.6.2 3D ground state degeneracies via trace method 108

B Appendices for Chapter 3 **112**

B.1 Hamiltonian formulation of $bF + bb$ theory for $k \in \mathbb{Z}, p = 2k$ 112

B.1.1 Trotter decomposition 112

B.1.2 The effective Hamiltonian 115

B.1.3 Connection to $\mathbb{Z}_p^{(1)}$ Walker-Wang models on the point-split lattice 119

B.2 $k = \text{even}, p = k$ 119

Bibliography **121**

Chapter 1

Introduction

The visible world is a frightfully complicated mix of many microscopic atoms and molecules. Despite this underlying complexity, principles and patterns emerge on larger scales. In particular, many systems can be organised into phases, where any two systems in the same phase have different microscopic parameters but the same behaviour at large distances.

What are the different possible phases of matter? This question is central to the theoretical study of condensed matter, but the answer remains elusive, in part due to our scant understanding of strongly interacting field theories. However, significant progress has been made on a related problem: What are the distinct gapped quantum phases of matter with very short ranged correlations? In other words, which many body Hamiltonians can we smoothly interpolate (or adiabatically tune) between without closing a gap in the spectrum? In particular, are there exotic gapped phases which *cannot* be adiabatically tuned to mundane (or 'trivial') phases, like insulators or paramagnets? The answer to the last question, perhaps surprisingly, is 'yes'.

A prominent example is the fractional quantum Hall effect (FQHE) [4, 5], arising in two-dimensional systems of electrons at low temperature and high magnetic field. While electron-electron correlations are exponentially decaying and the bulk is gapped, this state of matter is certainly not a mundane electronic insulator: Its transverse response σ_{xy} is quantised in fractional units of e^2/h; it has a chiral edge theory which cannot be realised as a purely $(1+1)$D state of matter; its lowest lying excitations are believed to carry a rational fraction of the fundamental electron charge and exhibit anyonic statistics; and, it has a ground state degeneracy depending on the topology of the underlying manifold. Whereas a trivial band insulator is captured by a theory of gapped fermions, many of the defining features of the FQHE are captured by an emergent Chern-Simons 'topological quantum field theory' (TQFT). The fractional quantum Hall effect is just one of many 'topologically ordered' states of

matter [6, 7], which are gapped but which have anyonic excitations, and a topological ground state degeneracy, described by TQFT's.

Not all exotic gapped states are topologically ordered in the same sense as the FQHE. The integer quantum Hall effect is an old example; it is distinguished from a trivial insulator by its quantised transverse conductivity $\sigma_{xy} = \text{integer} \times e^2/h$ and its gapless chiral edge theory. Both of these features are captured by an 'integer level' Chern-Simons theory, which is a TQFT but does not possess anyonic excitations or the topological ground state degeneracy present in topologically ordered states.

With the benefit of hindsight, it is unsurprising that TQFT's are germane to exotic short-range correlated states of matter. Let us consider the heuristic phase diagram in Fig. 1.1. The solid lines denote phase boundaries, and the arrows denote flow under coarse graining. The attractive fixed points of such a flow are indeed short range correlated states. Thus, we can hope to at least partly classify the various phases of exotic insulators and paramagnets by studying field theories which are fixed under coarse graining. TQFT field theories, by construction, have this property.

In this thesis, we explore a subset of the possible exotic gapped states by examining the properties of newly discovered Walker-Wang (WW) models of TQFT's in $(3+1)$D.[1] While some of the WW models have been known for some time, others are new. In particular, we highlight the existence of 'confined Walker-Wang models' which have no deconfined particles in their bulk, but realise a novel discrete chiral topological order on their surfaces. Moreover, we partly bridge the gap between these abstract TQFT's and more traditional field theories of bosons and fermions, with a view to understanding the possible gapped states of condensed matter systems in $(3+1)$D.

Before attacking the $(3+1)$D models, which form the main thrust of this thesis, in the following section we provide a pedagogical introduction to the simpler, more well known $(2+1)$D string-net (or Levin-Wen) models, concentrating on particular examples.

1.1 Topological order in 2D and Levin-Wen Lattice models

While 3D lattice models are the main focus of this work, it is useful to first review their 2D analogues — starting with some very simple examples. This will establish much

[1] In this context, the WW models are known as 'string-net models' because they can be described as models of fluctuating quantum mechanical strings.

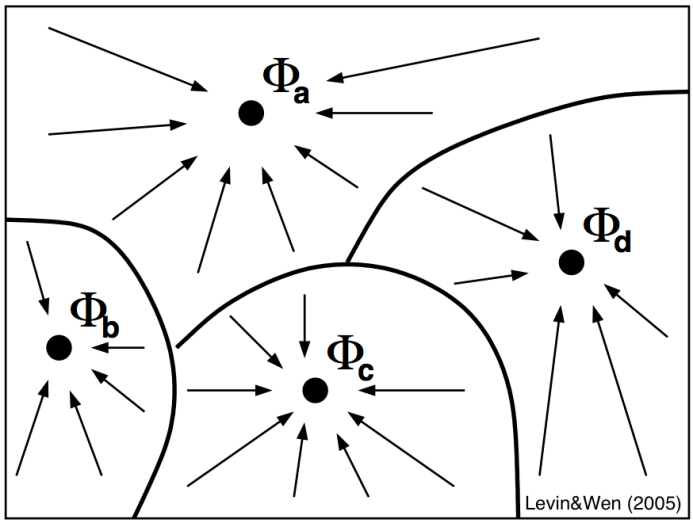


Figure 1.1: A very heuristic phase diagram. The arrows denote the flows of systems under coarse graining, while the black dots represent fixed points of this flow, many of which are characterised by string-net models.

of the necessary notation for the 3D case, as well as giving a flavour for topological order in 2D.

Much is understood about two dimensional systems with topological order. They have the following interrelated properties [6, 7]: (i) degenerate ground states [2], the number of which depends on the topology of the manifold; (ii) the emergence of point-like excitations with anyonic statistics; (iii) a constant, universal contribution to the entanglement entropy which can be isolated using the procedures in [8, 9]. These three properties are shared by some topological quantum field theories (TQFT's). For the purposes of this work, TQFT's are 'Chern-Simons'-type gauge theories with continuous groups, or their discrete group analogues 'Dijkgraaf-Witten' (or DW) models [10].

In what follows we will study the properties of two distinct $(2+1)$D DW models with discrete gauge group $\mathbb{Z}_2$. They are more commonly known as the toric code (or Ising gauge theory) and doubled semion (or DSem) models respectively. Both TC and DSem can be formulated as lattice models, where each bond takes one of two possible states (which we can call spin-down and spin-up). Both the toric code and the doubled semion model can be thought of as quantum loop gases in that the bonds with down spins must form closed loops. While in this aspect the two models are quite similar, their Hamiltonians are distinct, and as a result their spectra are

[2] On finite size systems, the putatively degenerate states become closer in energy exponentially quickly as the size of the system is increased.

different. While the toric code is just a simple $\mathbb{Z}_2$ gauge theory with Ising charges and fluxes, the doubled semion model harbours two opposite chirality species of semionic excitations (i.e., excitations which give berry phase $\pm i$ under exchange).

In Sec. 1.1.1 we introduce the well-known toric code [11, 12], and then calculate its ground state degeneracies and classify its low-lying excitations; experts may wish to skip this section. Then in Sec. 1.1.2 we do the same for the doubled semion model [12], paying particular attention to the types of defects that arise and how they differ from those found in the toric code. The notation and techniques introduced in this section provide a firm foundation for our study of the 3D models in Sec. 2.2.

1.1.1 The toric code

The Hilbert space of the toric code consists of a two-state system $\sigma^z = \pm 1$ on each edge of a honeycomb lattice as shown in Fig. 1.2. The Hamiltonian is given by

$$H = -\sum_v \underbrace{\prod_{i \in s(v)} \sigma_i^z}_{B_v} - \sum_p \underbrace{\prod_{i \in \partial p} \sigma_i^x}_{B_p}, \tag{1.1}$$

where $\sum_v$ runs over all vertices, and $\sum_p$ over all plaquettes, $s(v)$ is the set of three edges attached to v and ∂p is the set of six edges bounding plaquette p (see Fig. 1.2). The vertex operator B_v takes value ± 1 depending on whether there are an even/odd number of down-spins on the edges coming into vertex v. The plaquette operator B_p flips the spins on every edge of a plaquette p and commutes with B_v because it flips a *pair* of spins at each vertex v. Since clearly $[B_v, B_{v'}] = [B_p, B_{p'}] = 0$, the Hamiltonian is a sum of commuting operators, allowing us to write down its ground states exactly.

1.1.1.1 Ground States

Using the fact that all B_v and B_p have eigenvalues ± 1 we see that a lower bound on the ground state energy is obtained when

$$\prod_{i \in s(v)} \sigma_i^z = 1 \text{ for all } v \qquad \prod_{i \in \partial p} \sigma_i^x = 1 \text{ for all } p\,. \tag{1.2}$$

Any state which satisfies all of these conditions is automatically a ground state because it saturates a lower bound on the Hamiltonian. Remarkably such states exist. Henceforth we work with a basis of states for which the spins on the edges of the lattice are σ^z eigenstates, and we choose a 'loop gas' representation of these states as diagrams with only down-spin edges coloured. The first condition in Eq. (1.2) ensures

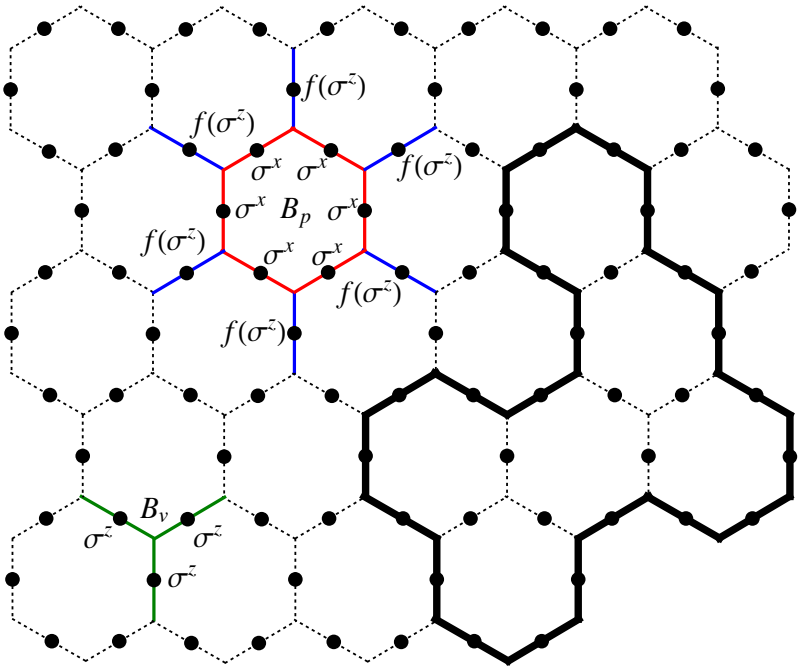


Figure 1.2: This figure shows a region of the lattice for the 2D models, where we have represented the spin degree of freedom on each edge with a black dot. Bold black edges represent $\sigma^z = -1$ spin configurations, while dashed edges represent $\sigma^z = +1$. The figure also indicates the edges involved in the definition of B_v; the three green edges in $s(v)$ are acted on with σ^z matrices as shown. The edges involved in B_p differ between the toric code and the DSem model. In the toric code B_p acts on the six red edges in ∂p with σ^x matrices as shown, and does not act on the six blue edges in $s(p)$ i.e. $f(\sigma^z) = 1$. In the DSem model, in addition to acting on the red edges with σ^x, the plaquette operator also acts on the six blue edges in $s(p)$ with $f(\sigma^z) = i^{(1-\sigma^z)/2}$.

that there are an even number of down-spins on the edges attached directly to any vertex, so the ground state must be made of a superposition of spin configurations which all involve only non-intersecting closed loops. The second condition in Eq. (1.2) tells us that any two spin configurations that are related to each other by flipping all the edges of a plaquette appear with the same coefficient in the ground state. This has three important consequences: Given two spin configurations obeying the first constraint in Eq. (1.2), if the loop gas pictures of these spin configurations can be related by deforming loops over plaquettes (as shown in Figure 1.3b), by removing contractible loops (as shown in Figure 1.3c), or by fusing loops together (as shown in Figure 1.3d), then the spin configurations appear in the ground state with the same amplitude. This is because the actions of deforming loops, removing contractible loops and fusion can all be implemented by applying a sequence of B_p operators, and $B_p = +1$ on the ground state. As a concrete example, if four configurations differ

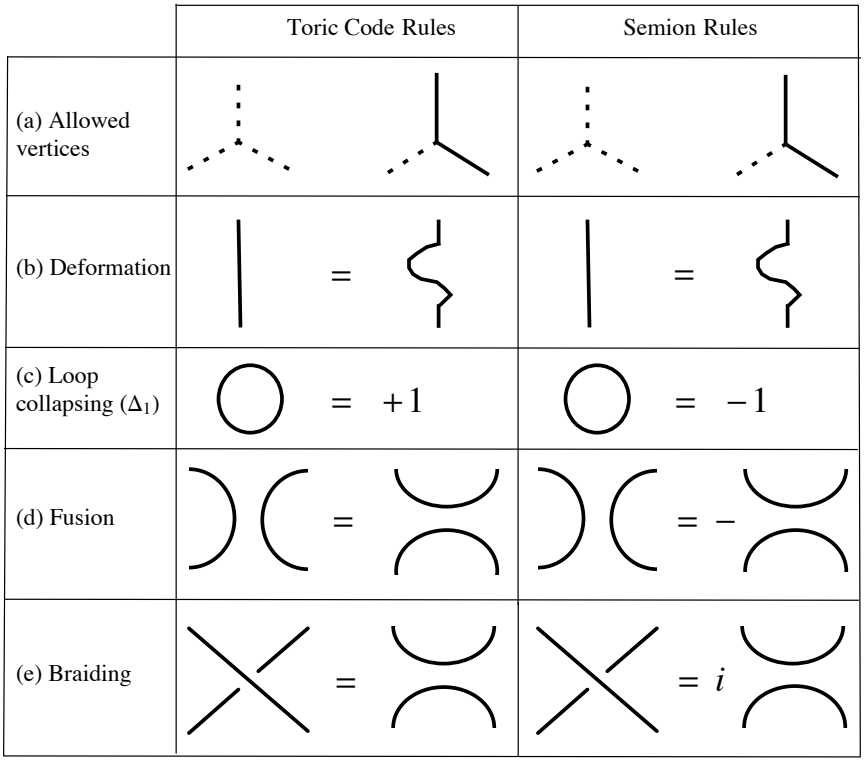


Figure 1.3: This figure shows the graphical rules for the toric code and DSem models. Row (a) represents the fact that the ground state only involves vertices with $B_v = 1$. The diagrams in (b)-(d) serve two purposes. Firstly, they tell us the relative amplitudes of loop gas configurations in the ground state e.g. row (c) tells us that configurations related by removing a closed loop occur with the same amplitude in the toric code ground state, but with a relative minus sign in the DSem ground state. Second, these diagrams provide a neat graphical mnemonic for the definitions of string operators.

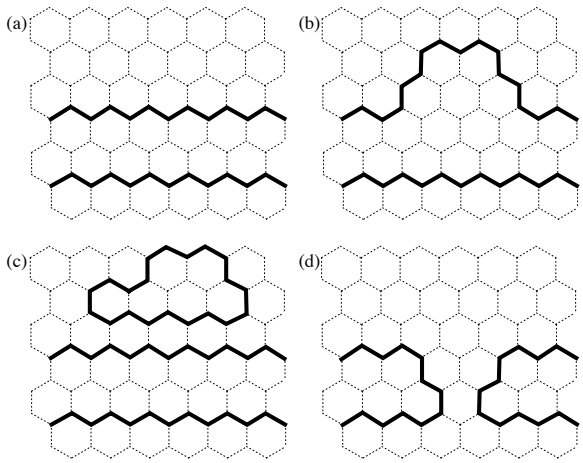


Figure 1.4: This diagram shows a specific small region of the lattice for four distinct spin configurations. The configurations are taken to be the same everywhere outside this region. For the toric code, all of these configurations occur in the ground state wave function with the same amplitude. This is because (b), (c), and (d) can all be made to look like (a) using loop deformation, loop collapsing and fusion respectively. In the DSem model, (a) and (b) occur with the same phase because they are related by deforming a loop. (a) and (c) occur with a relative minus sign because they differ by the presence of a single closed loop. (a) and (d) also occur with a relative minus sign because they are related by a single fusion (Fig. 1.3(d)).

only in a small region in the manner shown in Fig. 1.4(a)-(d) then they all appear in the ground state with the same amplitude. Loop deformation relates Fig. 1.4(a) and (b), loop collapsing relates Fig. 1.4(a) and (c) and loop fusion relates Fig. 1.4(a) and (d).

Now that we have concrete relations (Fig. 1.3(b)-(d)) between the coefficients of different spin configurations in the ground state we can deduce the ground state degeneracy for periodic boundary conditions in both directions (i.e. on the torus $\mathbb{T}^2$). Starting with any configuration of closed loops one can show that it appears in the ground state with the same amplitude as one of the four 'canonical' configurations labelled (a)-(d) in Fig. 1.5. These are distinguished by the winding number parities

$$P_x = \prod_{i \in c_x} \sigma_i^z \qquad P_y = \prod_{i \in c_y} \sigma_i^z \quad , \tag{1.3}$$

where c_x and c_y are cuts along the x and y directions respectively. Each distinct ground state is an equal superposition of all configurations related to a canonical ket by the equivalences in Fig. 1.3(b)-(d); some of the kets in each superposition are shown in Fig. 1.5.

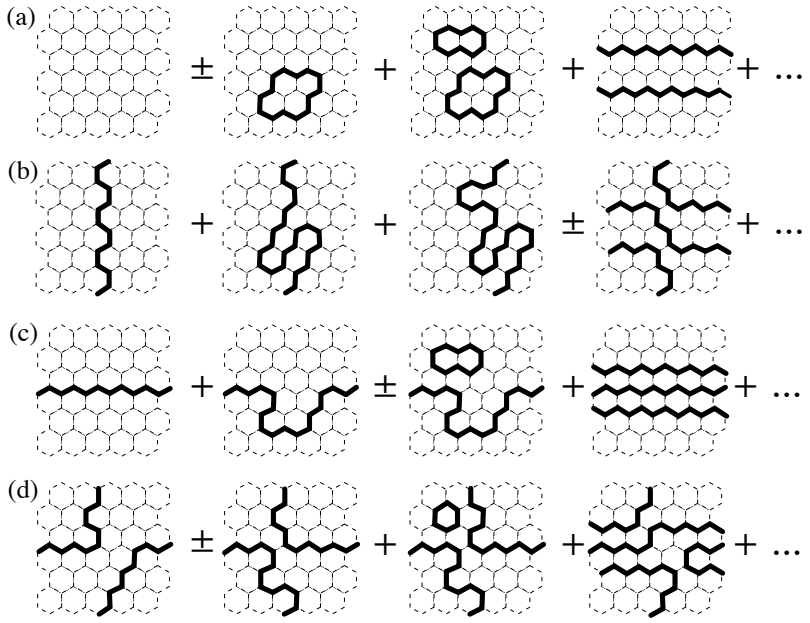


Figure 1.5: This figure shows the 4 independent ground state sectors in the toric code with periodic boundary conditions in both directions (i.e., on a torus). The 4 "canonical" kets can be taken to be the four spin configurations on the far left side labeled (a)-(d). Each of the 4 ground states is a superposition of all spin configurations which can be made to look like the canonical ket by using the equivalence rules shown in Fig. 1.3(b)-(d). For the toric code the relative coefficient is always +1. The ground state structure for the DSem model is similar except the kets marked with a ± appear with negative coefficients, a fact that can easily be checked using the rules in Fig. 1.3.

1.1.1.2 Excitations

The Hamiltonian Eq. (1.1) has two types of excitations: vertex defects where $B_v = -1$, and plaquette defects where $B_p = -1$. These defects are exact eigenstates because both B_p and B_v are conserved (that is, they commute with the Hamiltonian). Two further features of these excitations will be important in what follows. Firstly, an excitation necessarily involves a pair of vertex or plaquette defects. Secondly, both types of excitations are 'deconfined'[3], because the energy of a pair of vertex (or plaquette) defects is independent of their separation.

We can understand both of these features by considering how defects are created. To create a vertex defect at v, one must flip an edge spin in $s(v)$. This, however, creates a violation on the adjacent vertex v_2 sharing this edge. We can remove this violation by flipping a second edge spin in $s(v_2)$. However, this just moves the violation to a third vertex v_3, and so on. Hence we can never create a lone

[3]Vertex defects are deconfined if their world-lines have a perimeter law free energy cost.

vertex defect but we can create a pair of vertex defects by flipping the spins along a continuous path $\mathcal{C}$ of edges by acting with the operator $\hat{W}_V(\mathcal{C}) = \prod_{i\in\mathcal{C}} \sigma_i^x$, as shown in Fig. 1.6. We call this a vertex-type string operator. Crucially the string operator commutes with all plaquette operators along its length (because it only involves σ^x's), so only has an energy cost from the vertex defects at its endpoints. This tells us that vertex excitations are deconfined, and that closed strings without end-points have no energy cost. Indeed, taking $\mathcal{C} = \partial p$ gives precisely the plaquette operator B_p, which commutes with the Hamiltonian by construction. A closed vertex type string operator that wraps several plaquettes is just the product of B_p's for the enclosed plaquettes. However, interestingly, one can also construct non-contractible vertex type string operators which flip spins along paths $\mathcal{C}_x, \mathcal{C}_y$ which wind completely around the system in the x or y direction respectively. The resulting operators $\hat{W}_V(\mathcal{C}_x), \hat{W}_V(\mathcal{C}_y)$ flip the parities P_y or P_x respectively and so have the effect of toggling between the four different ground state sectors in Fig. 1.5.

One can similarly define plaquette-type string operators that create pairs of plaquette defects. These take the form $\hat{W}_P(\mathcal{C}') = \prod_{i\in\mathcal{C}'} \sigma_i^z$, where $\mathcal{C}'$ is a string on the dual lattice as shown in Fig. 1.6. Vertex defects have nontrivial relative statistics with plaquette defects: Moving a vertex defect all the way around a plaquette defect gives a Berry phase of -1, and vice versa. These statistics are a defining element of topological order, and will allow us to distinguish the toric code from the doubled semion model which we discuss in the next section.

1.1.1.3 Graphical representation of operators as strings

Before discussing our next 2D topological lattice model, it is useful to review the connection between the rules in Fig. 1.3 and the lattice model. Thus far, we have established that the rules in Fig. 1.3 (b)-(d) can be used to evaluate the relative amplitudes of different kets in a particular ground state. However, they can also be used to depict the action of the string operators defined in the previous section. An example is shown in Fig. 1.7: the plaquette operator B_p can be represented by a string running along the inside of the plaquette p. To determine the action of this operator on a particular ket, we "fuse" this string with the relevant edge labels of p using Fig. 1.3(d).

Vertex string operators $\prod_{i\in\mathcal{C}} \sigma_i^x$ are defined using a similar procedure: we depict the string operator graphically as a string running along the path $\mathcal{C}$. The action of the operator on a ket is given by fusing this string into the edges along $\mathcal{C}$ using Fig. 1.3(d) and (e). (For the toric code the rule (e) is superfluous; however in other models it

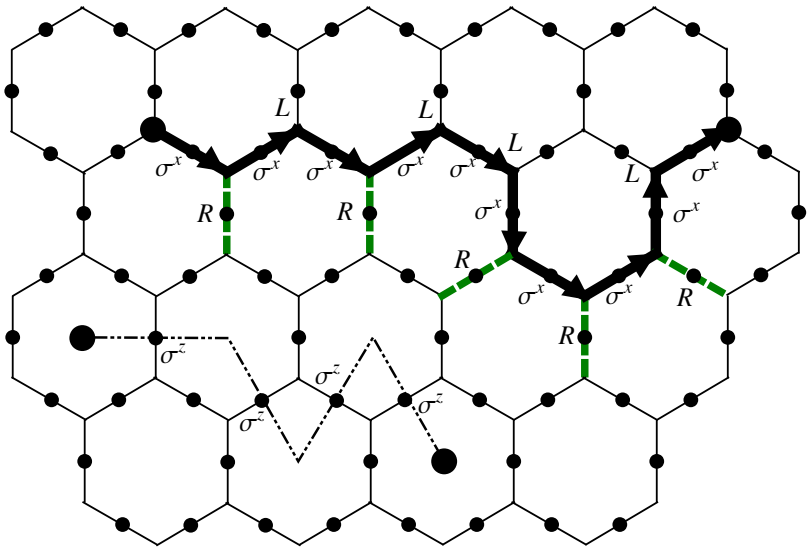


Figure 1.6: This figure shows the different types of string operators in the simple 2D lattice models. For the toric code, the vertex type string operator simply flips the spin on every edge of a path with σ^x. The plaquette type string operator is represented as a line living on the dual lattice, and every edge that crosses the line is acted on with σ^z. For the DSem model, the plaquette type string operator is precisely the same. The vertex type string operator, however, includes additional phases which depend on the spins touching the path. A phase $(\pm i)^{(1-\sigma^z)/2}$ is associated with the dashed (green) edges labelled R which lie just to the right of the path; the choice of $\pm$ determines the chirality of the string. Vertices labelled L are attached to an edge lying on the left of the path, and these vertices are associated with a phase $(-1)^{\frac{1}{4}(1-\sigma_i^z)(1+\sigma_j^z)}$ where i/j are the edges on the path just before/after the L-vertex.

will be necessary as we will assign a definite meaning to strings drawn crossing over, as opposed to under, the edges in its path (Fig. 1.8).)

Using these graphical representations of states and operators, it is possible to describe many more 2D topological lattice models than the ones we describe here [12]. A careful discussion of the conditions under which these graphical procedures give a consistent and unambiguous action for the operators in the theory can be found in [12, 13].

1.1.2 The doubled semion model

The toric code model shows that it is possible to write a simple and exactly solvable spin Hamiltonian exhibiting topological order. Many generalisations are known but here we describe one of the simplest, a second loop model known as the doubled semion or DSem model first discussed in [12] and [14]. The Hamiltonian takes the

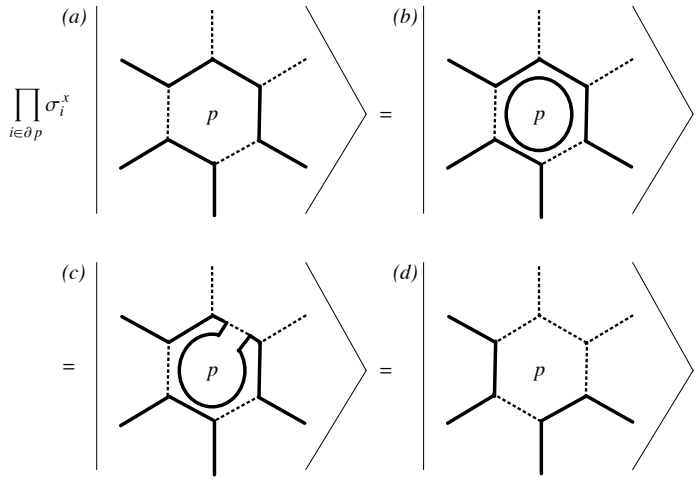


Figure 1.7: This diagram shows how we can use the fusion rules to graphically define a plaquette flipping term (a) using a string that lives off lattice shown in (b). The key step occurs in going from (b)-(c) where we use Fig. 1.3(d) to fuse the string into the edge. The end result (d) is that all edges on the plaquette are flipped, which is precisely the action of $\prod_{i\in\partial p}\sigma_i^x$.

form

$$H = -\sum_v \underbrace{\prod_{s(v)} \sigma_i^z}_{B_v} + \sum_p \underbrace{(\prod_{i\in\partial p} \sigma_i^x) \prod_{j\in s(p)} i^{(1-\sigma_j^z)/2}}_{B_p}, \tag{1.4}$$

where $s(p)$ is the set of six legs radiating from plaquette p, as shown in Fig. 1.2, and as above $s(v)$ and ∂p denote the three edges entering vertex v, and the six edges bordering plaquette p respectively. Comparing Eq. (1.4) with the toric code Hamiltonian in Eq. (1.1), we see that B_v is unchanged but the plaquette terms differ: in addition to flipping the edges of p, the new B_p operator includes a phase which depends on the spins in $s(p)$. Furthermore, the plaquette part of the DSem Hamiltonian appears with a total + sign rather than a − sign.

For any state $|\Psi_{loop}\rangle$ obeying $B_v|\Psi_{loop}\rangle = |\Psi_{loop}\rangle$ (a 'loop gas state'), it is easy to show that

$$[B_p, B_v]\,|\Psi_{loop}\rangle = [B_p, B_{p'}]\,|\Psi_{loop}\rangle = 0 \tag{1.5}$$

and furthermore that B_p has eigenvalues ± 1 on these loop gas states. Thus if we restrict our Hilbert space to the loop gas states, the Hamiltonian is a sum of commuting projectors and is thus exactly solvable. This fact will allow us to solve exactly for the ground states of the Hamiltonian, because we will find that these only involve closed loop configurations. Though it will not be necessary for our purposes, with a more

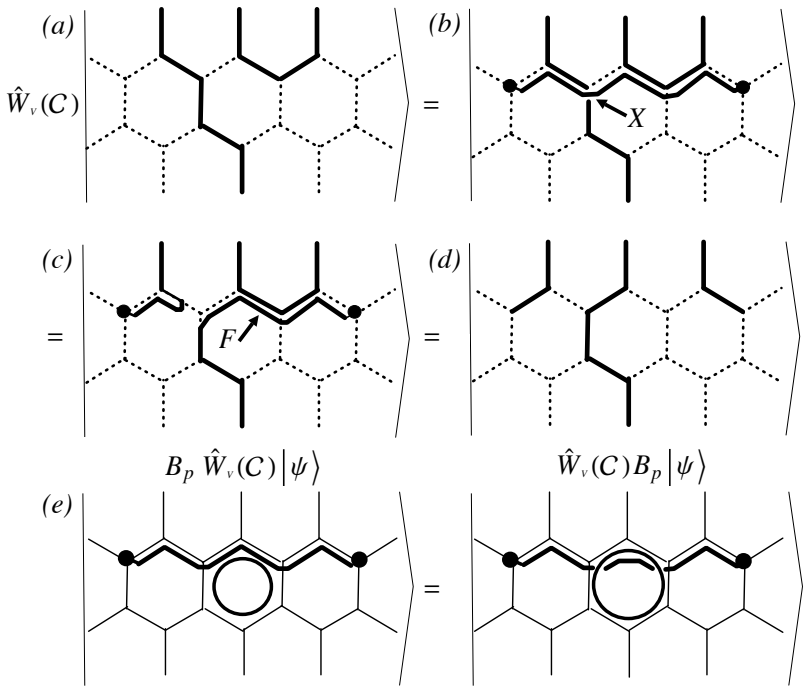


Figure 1.8: This diagram illustrates how we can use an off-lattice string to define a string operator $\hat{W}(C)$. Starting with some ket in (a) we define the string operator using the diagram in (b), where the black dots denote the end-points of the string operator. In order to evaluate this diagram we need to use the fusion rule Fig. 1.3(d) at the point labelled F and the braiding rule Fig. 1.3(e) at point X to resolve the string under-crossing the lattice edge. (e) Represents a graphical proof that the plaquette operator commutes with the string operator along its length; on the left hand side the string acts first, on the right hand side the plaquette operator acts first. We can move between these two diagrams by deforming the string locally, which is allowed as long as the string operator does not move through the centre of a plaquette.

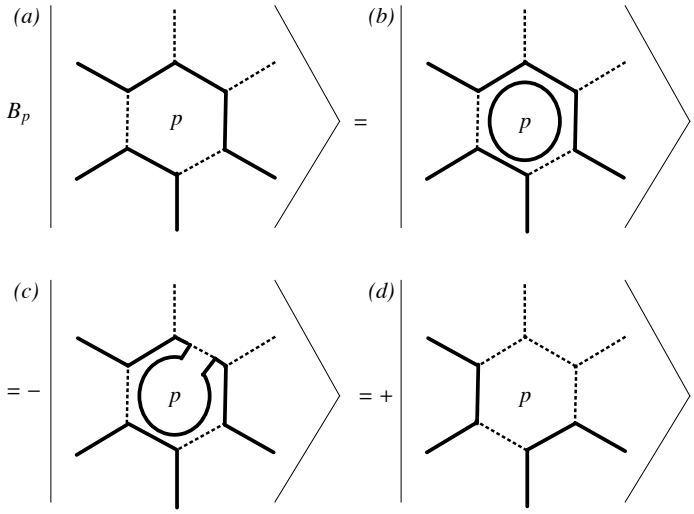


Figure 1.9: This figure shows the graphical definition of a B_p on a ket in the DSem model. (b) shows the definition in terms of a string operator. The step (b)-(c) requires the use of a fusion rule Fig. 1.3(d), so produces a minus sign. Similarly, step (c)-(d) requires a fusion, giving a net plus sign. The original ket and (d) are related by a single application of B_p, therefore they appear with opposite sign in the ground state because $B_p = -1$ on the ground state.

complex definition of B_p it is possible to write a Hamiltonian that is exactly solvable on the full Hilbert space (see App. A.3).

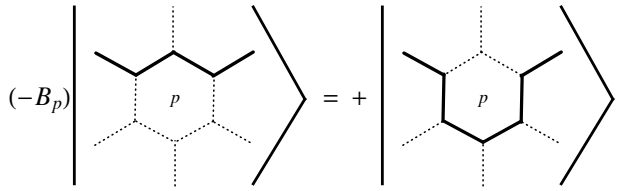
1.1.2.1 Ground States

A lower bound on the ground state energy is obtained when

$$B_v = 1 \text{ for all } v \qquad B_p = -1 \text{ for all } p\,. \tag{1.6}$$

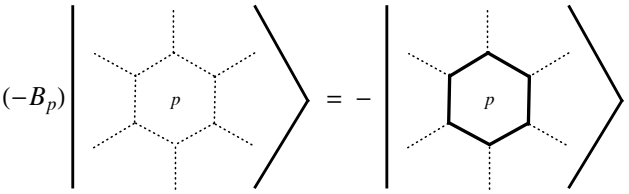
Any state which satisfies all of these conditions is automatically a ground state because it saturates a lower bound on the Hamiltonian. Once again such states exist. Since the vertex condition is the same, the ground states of the doubled semion model are also made of a superposition of spin configurations which involve only non-intersecting closed loops. However, as we will see below, the coefficients in the superposition are different from those of the toric code.

The condition $B_p = -1$ implies that the two spin configurations involved in the equation



, (1.7)

occur with the same coefficient in the ground state superposition. Therefore, similar to the toric code, configurations related by deforming a loop over a plaquette occur with precisely the same coefficient in the ground state (as indicated by Fig. 1.3(b)). However, the $B_p = -1$ condition implies that the two kets involved in



, (1.8)

occur with a relative minus sign in the ground state superposition. Therefore spin configurations related by the creation or elimination of a closed contractible loop have a relative minus sign in the ground state superposition (as indicated by the rule in Fig. 1.3(c)). In the same way one can show that configurations related by the fusion rule Fig. 1.3(d) occur with a relative minus sign. Thus the doubled semion graphical rules Fig. 1.3(b)-(d) give linear relations between the coefficients of spin configurations in the ground state as illustrated in Fig. 1.4.

In the ground state space, the amplitude of any loop configuration can be related, by using the DSem graphical rules Fig. 1.3(b)-(d), to the amplitude of one of the canonical kets labelled (a)-(d) in Fig. 1.5. As these new rules have minus signs, the ground states are similar to those in the toric code except some configurations appear with a -1 coefficient, as shown in the superposition in Fig. 1.5. Analogous to the toric code, the ground state space is thus split into 2^2 orthogonal sectors distinguished by parity operators P_x, P_y.

1.1.2.2 Excitations

The low lying excitations of the doubled semion Hamiltonian appear as pairs of vertex defects where $B_v = -1$, or pairs of plaquette defects where $B_p = +1$. As for the toric code, the operators that create pairs of defects are 'string operators' acting on all edges along some path C joining the pair. Here we will show how to construct string operators $\hat{W}_P, (\hat{W}_V)$ that create plaquette (vertex) defects at their endpoints

respectively, and commute with the Hamiltonian away from their endpoints. It follows that both vertex and plaquette excitations are deconfined: the energy cost of creating a pair of either of these is independent of their separation.

The plaquette type string operator is identical to that in the toric code, taking the form $\hat{W}_P(\mathcal{C}') = \prod_{i\in\mathcal{C}'} \sigma_i^z$, where $\mathcal{C}'$ is a string on the dual lattice (see Fig. 1.6). Such an operator manifestly commutes with every B_v, and only induces plaquette defects at its endpoints, where it anti-commutes with the $\prod \sigma^x$ part of the B_p operators. On the other hand, the vertex type string operator from the toric code model, $\prod_{i\in\mathcal{C}} \sigma_i^x$, fails to commute with the modified plaquette operators bordering on $\mathcal{C}$ because of the $i^{(1-\sigma_j^z)/2}$ factor in the new definition of B_p. To write down a vertex type string operator that produces vertex violations at its endpoints but commutes with plaquettes along its length, $\prod_{i\in\mathcal{C}} \sigma_i^x$ must be combined with phases depending on the spins on edges touching the path to form the following operator $\hat{W}_V^{\pm}(\mathcal{C})$

$$\prod_{i\in\mathcal{C}} \sigma_i^x \prod_{k\in L \text{ vertices}} (-1)^{\frac{1}{4}(1-\sigma_i^z)(1+\sigma_j^z)} \prod_{l\in R \text{ legs}} (\pm i)^{(1-\sigma_l^z)/2}\,. \tag{1.9}$$

To specify the phases such that $\hat{W}_V^{\pm}(\mathcal{C})$ commutes with B_p everywhere, we have had to choose an orientation for our string operator (Fig. 1.6), and separate the vertices into two types: L-vertices are attached to an edge on the left of $\mathcal{C}$, while R-vertices are attached to an edge on the right of $\mathcal{C}$ which we call an R-leg. Each L-vertex is also attached to two edges on $\mathcal{C}$, and these are denoted by i, j where i occurs before j on the directed path $\mathcal{C}$. The choice of $\pm$ determines whether the string has $\pm$ 'chirality'. The phases in the definitions of the string operators imply that two vertex string operators of the same chirality anti-commute if their paths cross. This indicates a sensitivity to the order in which particle pairs are created and destroyed, and can be used to show that vertex defects of the same chirality have semionic statistics [12]: exchanging a pair of these induces a phase of $\pm i$ in the wave function.

There is again a simple graphical mnemonic which reproduces the required spin flips and configuration dependent phases along the length of the string away from its endpoints. Pairs of 'positive chirality' vertex defects can be created by laying a string *over* the lattice along a prescribed path and using the rules Fig. 1.3(b)-(e) to fuse the string into the edges; an example of this procedure is shown in Fig. 1.10. The complex conjugate operator corresponds to laying the string *under* the edges it crosses in the lattice, and produces a pair of 'negative chirality' vertex defects.

As in the toric code, it is useful to consider string operators that do not create excitations (i.e. where the curve $\mathcal{C}$ has no endpoints). If $\mathcal{C}$ encircles a single plaquette

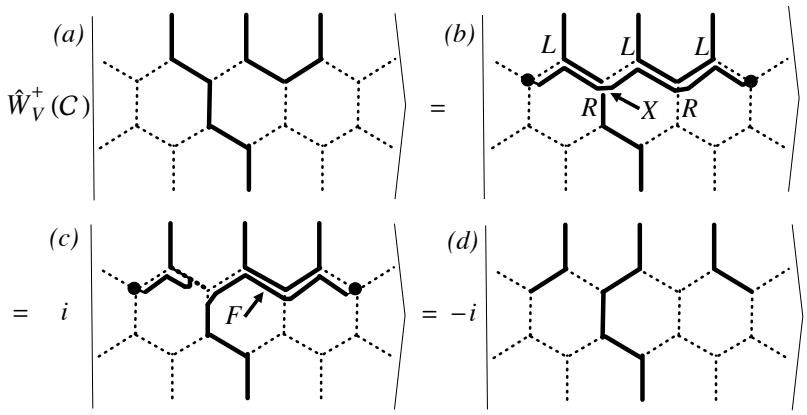


Figure 1.10: This diagram illustrates how we can use an off-lattice string to define a positive chirality string operator $\hat{W}^+(C)$ in the doubled semion model; positive chirality corresponds to taking $+i$ in the concrete Pauli matrix form of the operator in Eq. (1.9). Starting with some ket in (a) we define the string operator using the diagram in (b), where the black dots denote the end-points of the string operator. In order to evaluate this diagram we need to use the braiding rule Fig. 1.3(e) at the string over-crossing labelled X, yielding a factor of i. We then use the fusion rule Fig. 1.3(d) at point F to fuse the string into the edge, yielding an additional factor of -1.

p, $\hat{W}_V^{\pm}(\mathcal{C}) = B_p$, and hence $\hat{W}_V^{\pm}(\mathcal{C})$ commutes with H. If $\mathcal{C}$ traces the perimeter of a cluster of plaquettes, $\hat{W}_V^{\pm}(\mathcal{C}) = \prod_{p \in cluster} B_p$ and hence such string operators act trivially on the ground states. The operators of main interest are again those vertex type string operators which follow paths $\mathcal{C}_x, \mathcal{C}_y$ which wind completely around the system in the x and y direction respectively. The resulting operators $\hat{W}_V^{\pm}(\mathcal{C}_x)$, $\hat{W}_V^{\pm}(\mathcal{C}_y)$ flip the parities P_y, P_x respectively. These non-contractable string operators cannot be written as a product of B_p operators, but still commute with the Hamiltonian and have the effect of toggling between the four different ground state sectors in Fig. 1.5.

We end this section by noting a technical point. The above expression Eq. (1.9) gives the correct form of vertex type string operators away from their endpoints. Capturing the precise form of the string operator at its endpoints requires greater care. The details of this are not essential for our purposes, but are shown in App. A.3.

1.2 This thesis

This thesis is structured as follows. In Chapter 2 we introduce the Walker-Wang models and characterise their bulk spectra and topological order, as well as the anyonic excitations sometimes present at their surfaces. Then in Chapter 3, we argue

that certain Walker-Wang models arise as a low-energy effective description of axion electrodynamics. In the process, we construct an effective field theory for many Walker-Wang models. Axion field theories are thought to arise as effective descriptions of certain condensed matter systems with strong spin-orbit coupling, so we suggest that Walker-Wang models give a window into the possible phases of these systems. In Chapter 4, we provide a more detailed summary of the work contained in this thesis, and indicate directions for possible future research.

Chapter 2

Walker-Wang models

2.1 Introduction

Having discussed the two dimensional case in Chapter 1, we now ask what happens in three dimensional topological systems. Though statistics between point particles in $D = 3$ must be fermionic or bosonic, interesting statistical interactions can still exist between vortex defects, between point particles and vortex defects (as in discrete gauge theories), or between point-like defects with additional structure [15, 16]. Thus one class of 3D topological phases contains particles that have unconventional statistics, as they are not strictly point-like. A second category of 3D phases that share some of the characteristics of 2D topological phases are fractional topological insulators [17, 18, 19]. When time reversal symmetry is present, the surfaces of these systems have protected gapless excitations. If time reversal is broken, however, the surfaces exhibit a fractional Hall effect. These gapped surfaces are thus expected to support chiral anyonic excitations.

In the present chapter, we focus on a third class of 3D topological phases, which can be realized by a family of Hamiltonians introduced by Walker and Wang [20]. Specifically, we discuss phases realized by a subset of these models, which we will call confined Walker-Wang models. These are reminiscent of fractional topological insulators in that the 2D surfaces of these 3D systems have the same deconfined anyons as a fractional quantum Hall state. They differ, however, in that a fractional topological insulator has a topological ground-state degeneracy in periodic boundary conditions [19]. The confined Walker-Wang models, on the other hand, have non-degenerate ground states for the same boundary conditions. As we will see in Chapter 3, these confined Walker-Wang models more strongly resemble the confined phases of axion gauge theories.

The exactly solvable Walker-Wang Hamiltonians we study here are 3D cousins of the 2D string-net models introduced by Levin and Wen [12] (see Chapter 1.1), and operate on the same underlying principles. We do not expect that the Walker-Wang Hamiltonians can be implemented exactly in a real physical system; rather, they are interesting because they can be solved exactly, and capture the long-wavelength physics of certain topological states of matter. They thus provide a framework in which to study the physical properties of these topological states.

In the present chapter, our key findings are as follows. As mentioned above, and unlike both discrete gauge theories and true fractional topological insulators, the confined Walker-Wang models that we consider have a unique ground state on any *closed* 3D lattice (i.e., a lattice that has no boundary). Thus in the absence of boundaries, the models are not topologically ordered in the usual sense. The possible excitations in the bulk are line defects with an energy cost per unit length: in other words, the bulk admits no deconfined point particles. Unlike vortex lines in 3D systems, which must form closed loops, these line defects can end at points in the bulk. The name "confined" Walker-Wang model stems from the fact that these point particles are confined – that is they must sit at the end-points of line defects that have a fixed energy cost per unit length (analogous to flux-tubes in a confining gauge theory). If the lattice does have a boundary, however, the system has the more conventional hallmarks of topological order: with appropriate boundary conditions, the surfaces admit deconfined anyonic excitations, and the ground state is degenerate. Though much of our work focuses on the simplest (abelian) example of the family of confined Walker-Wang models, we will show that these properties also apply to models that have deconfined non-abelian anyons at their surfaces.

The surface states of the confined Walker-Wang models can have the topological properties (i.e., anyon content and ground-state degeneracy) of a bosonic quantum Hall state. Walker-Wang models with fermionic quantum Hall surface states also exist; in addition to the surface topological order, these have a deconfined fermion and $\mathbb{Z}_2$ topological order in the bulk, which we will also discuss in some detail.

Given the absence of bulk topological order in confined Walker-Wang models, and the fact that their surface states have the same anyon content as 2D Quantum Hall states of matter, one might legitimately ask whether there is anything "special" about confined Walker-Wang models. Do they represent a new phase of matter? Can their surface states (which have zero correlation length) be realised in purely two

dimensional systems?[1] We do not have a comprehensive answer to these questions, but we return to the issue in more detail in Chapter 4.

The bulk of this chapter will focus on the simplest topological models – those that can be described as loop gases. In Sec. 1.1 we reviewed the 2D loop gases: the toric code and the 2D doubled semion (DSem) model in the form introduced by Levin and Wen [12]. In the present chapter, starting with Sec. 2.2, we present the 3D generalisations of these loop gas models: the 3D toric code [21] (essentially the deconfined limit of 3D $\mathbb{Z}_2$ lattice gauge theory) and a 3D analogue of the semion model (3DSem), which is our paradigm for confined Walker-Wang models. After describing these Hamiltonians, we discuss their low-energy physics for periodic boundary conditions (i.e., if the system is on a three-torus, $\mathbb{T}^3$), showing that whereas the toric code has deconfined point particles and a degenerate ground state, the 3DSem model has a unique ground state and no deconfined point-like excitations. In Sec. 2.3 we study the low-energy physics of these models *with* boundaries. We find that for 3DSem, boundaries introduce new ground state sectors, and that deconfined anyonic excitations can exist on the boundary.

While a large part of this work focuses on the 3D toric code and the 3DSem models, these constitute only a small subset of the possible Walker-Wang models. In Sec. 2.4 we discuss how our results extend to the more general case. We show that 3DSem is one member of a large family of confined Walker-Wang models for which all point defects are confined in the bulk, and the ground state degeneracy is completely determined by the topology of the boundary of the system. Most generally, the surface excitations of confined Walker-Wang models can be non-abelian anyons. In Sec. 2.5, we study Walker-Wang models that describe fermionic systems, whose surface states have the topological order of fermionic quantum Hall systems and whose bulk has a deconfined fermionic point excitation. A number of technical aspects of the models are then addressed in the appendices.

Since the Hamiltonians we discuss were introduced by Walker and Wang [20], it is worth emphasising what is new in the present chapter. Our main contribution is to treat in detail the excitations of these Hamiltonians, particularly on their boundaries. This allows us to describe the full spectrum of "topological" features of the systems in question. We also discuss the possible boundary conditions of these models, and

[1] This question is important in characterising symmetry protected topological (SPT) phases, like topological insulators, whose surface states are often anomalous in 2D. For example, the time reversal invariant boundary of a non-interacting fermionic topological insulator has a single surface Dirac cone that cannot be realized in any 2D model with the same symmetries.

under what circumstances the topological order associated with the surface can be destroyed.

2.2 Simple 3D topological lattice models on closed manifolds

In this section we follow the prescription of Walker and Wang [20] to generalise the 2D toric code and DSem models to 3D. The resulting 3D lattice models are described by a two-state system $\sigma^z = \pm 1$ on each edge of the trivalent lattice shown in Fig. 2.1. The generalisation of the 2D toric code to 3D is well known [21, 22]. We nevertheless begin by reviewing the key signatures of topological order in this model (ground state degeneracy, possible defects and their statistics) for later contrast with the properties of the 3D cousin of the DSem model. In Sec. 2.2.1 we discuss the ground state degeneracy of the 3D toric code on the 3-torus, and describe the low-lying excitations which take the form of deconfined point defects and linearly confined vortex rings.

In Sec. 2.2.2 we present the 3D analogue of the 2D DSem model (the '3D semion' or '3DSem' model), which is our first example of a confined WW model. Again we characterise the model by studying its ground states and excitations. We find that the ground state is non-degenerate on the 3-torus, and in Sec. 2.2.2.3 we relate this to the fact that its point defects are confined in the bulk. On a manifold with boundary Sec. 2.3, for certain boundary conditions, the 3DSem model harbours deconfined chiral semions on its surface and can have a topological ground state degeneracy. We find that the 3D toric code and semion models capture much of the qualitative behaviour of more general Walker-Wang models which we study in Sec. 2.4.

2.2.1 The 3D toric code

Viewed as a Walker-Wang model, the 3D toric code [21, 22] Hilbert space consists of a two state system $\sigma^z = \pm 1$ on each edge of the lattice shown in Fig. 2.1. The Hamiltonian takes the form

$$H = -\sum_v \underbrace{\prod_{i \in s(v)} \sigma_i^z}_{B_v} - \sum_p \underbrace{\prod_{i \in \partial p} \sigma_i^x}_{B_p}, \tag{2.1}$$

where $s(v)$ is the set of three edges attached to vertex v and ∂p is the set of ten edges of a plaquette p (bold edges shown on the 3 types of plaquette in Fig. 2.5(a)-(c)). As in 2D, the B_v take the values ± 1 depending on whether there are an even/odd number

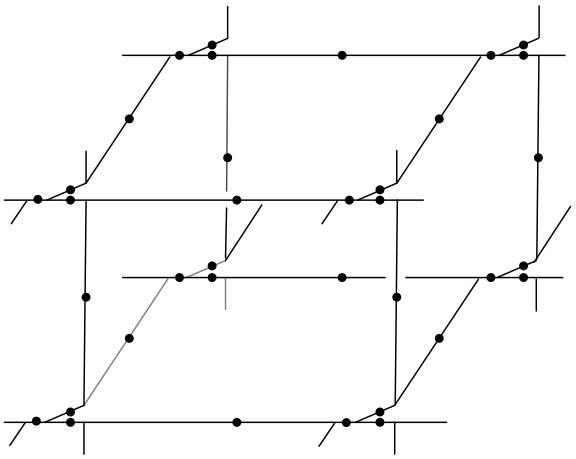


Figure 2.1: This figure shows the point splitting and fixed projection used to define the 3D lattice for the Walker-Wang models. The dot in the middle of each bond represents a spin variable.

of down spins on the edges coming into vertex v, and B_p flips the spins on each edge of p. The fact that B_p flips a pair of spins at vertex v implies that $[B_p, B_v] = 0$, and once again $[B_v, B_{v'}] = [B_p, B_{p'}] = 0$, so the model is exactly solvable.

2.2.1.1 Ground states of the toric code on $\mathbb{T}^3$

The ground state space is defined by the conditions $B_p = B_v = 1$ for all vertices and plaquettes. As in the 2D case in Sec. 1.1.2.1, the condition $B_v = 1$ forces the 3D ground state to be a superposition of closed loops. Recall that in 2D, the condition $B_p = +1$ implied that the rules in Fig. 1.3 (b)-(d) relate the amplitudes of different spin configurations. Exactly the same type of calculation shows the rules in Fig. 1.3 (b)-(d) relate the amplitudes of loop configurations in the ground state space of the 3D toric code.

In the 2D toric code on the 2-torus, the amplitude of any spin configuration in the ground state could be related to the amplitude of one of four canonical configurations (shown in Fig. 1.5) resulting in four degenerate ground states. Analogously, on the 3-torus one can show that any configuration of closed loops appears in the ground state with the same amplitude as one of the eight canonical configurations shown in Fig. 2.2. These 2^3 configurations can be labelled by three parities

$$P_{n_\perp} = \prod_{i \in n_\perp} \sigma_i^z \qquad n = x, y, z \tag{2.2}$$

which take values ± 1 depending on whether an even or odd number of loops wind around the n-cycle of the torus. Here $z_\perp$ is the set of all edges emanating from the

plane ($z = 0$) in the $+\hat{z}$-direction, and similarly for $x_\perp, y_\perp$. If we take an equal superposition of all configurations related to one of the eight canonical configurations by the equivalences in Fig. 1.3(b)-(d) (as shown in Fig. 2.3) then it is easy to verify that we get a ground state. This shows us that the ground state degeneracy is 2^3, and each distinct ground state is labelled by the three eigenvalues $P_{x_\perp}, P_{y_\perp}, P_{z_\perp} = \pm 1$. On more general closed manifolds the ground state degeneracy is 2^{b_1}, where b_1 is the number of independent non-contractible cycles on the manifold (also known as the first Betti number).

2.2.1.2 Excitations in the toric code

The Hamiltonian (2.1) has two types of excitations: pairs of vertex defects where $B_v = -1$, and lines of plaquette defects where $B_p = -1$. We can create a pair of vertex defects with an operator

$$\hat{W}_V(\mathcal{C}_{AB}) = \prod_{i \in \mathcal{C}_{AB}} \sigma_i^x \,, \tag{2.3}$$

where $\mathcal{C}_{AB}$ is a path connecting the positions of the defects A and B. Graphically we represent the string operator by laying a string along $\mathcal{C}_{AB}$, where it is understood that the operator acts on kets by fusing this string into the edges using the rules Fig. 1.3(b)-(e). The operator commutes with the Hamiltonian except at its endpoints, and so the defects are deconfined.

As in 2D, a closed vertex type string operator that wraps around the boundary of several plaquettes is just the product of B_p's for the enclosed plaquettes and so trivially commutes with the Hamiltonian. Non-contractible string operators (i.e., string operators that wrap around the periodic boundary conditions) are more interesting because they commute with the Hamiltonian but cannot be expressed as a product of B_p's. Operators of this form toggle between the different ground state sectors discussed in Sec. 2.2.1.1; for example, a non-contractible string operator wrapping the z-direction of the torus toggles between the ground states in Fig. 2.3(a) and (b).

Thus, vertex defects in 3D are much the same as they were in 2D, being thought of as the end-points of a string operator. Plaquette defects, on the other hand, behave quite differently in 2 and 3 dimensions. They no longer appear at the end-points of string operators, but rather at the boundary of surface operators. To create a plaquette defect, one acts on an edge with a σ^z. This, however, creates defects in all four plaquettes associated with the edge. More generally, if we pick a surface on

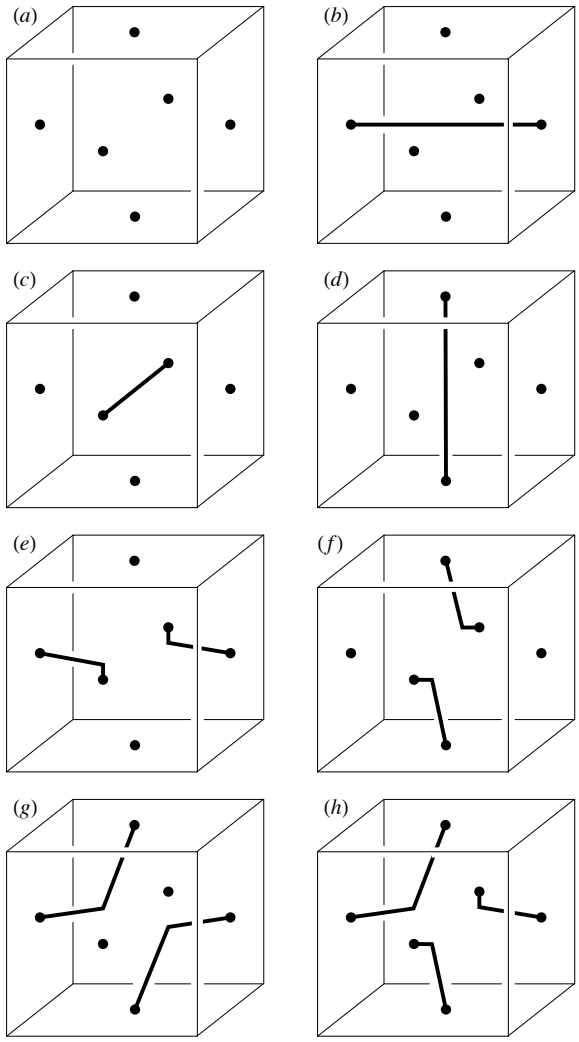


Figure 2.2: Shown are the eight canonical configurations with periodic boundary conditions in all three directions, where the thick black lines indicate edges with $\sigma^z = -1$. The underlying lattice is not drawn, for simplicity. Any basis ket without vertex violations can be related to one of these eight by using the graphical rules in Fig. 1.3. In the case of the toric code, the ground state splits into eight orthogonal sectors labelled by these eight kets; two of these states are shown in Fig. 2.3.

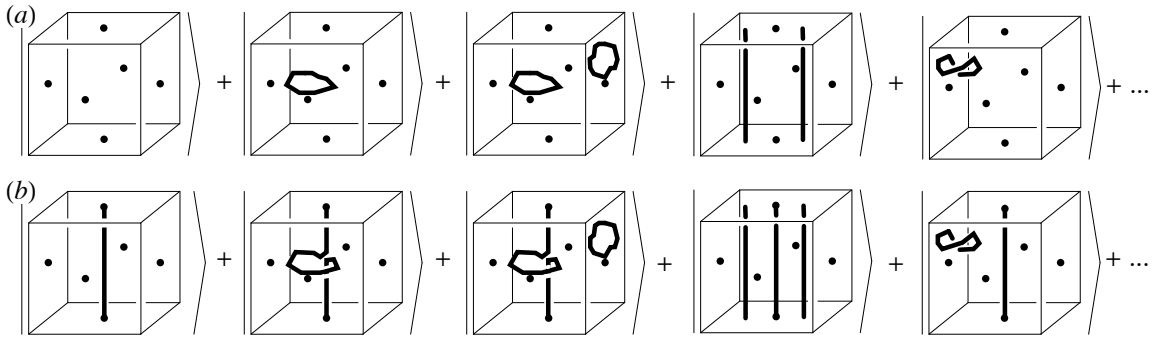


Figure 2.3: This figure shows two examples of ground states of the 3D toric code. (a) consists of an equal superposition of all kets related to Fig. 2.2(a) by Fig. 1.3(a)-(d), and has $P_{x_\perp} = P_{y_\perp} = P_{z_\perp} = 1$. (b) consists of an equal superposition of all kets related to Fig. 2.2(d) by the same graphical rules, and has $P_{x_\perp} = P_{y_\perp} = 1$ but $P_{z_\perp} = -1$. There are a further six ground states corresponding to the other kets in Fig. 2.2. The underlying lattice is not drawn, for simplicity.

the dual lattice and act with σ^z on each edge cutting the surface, then the resulting operator

$$\hat{W}_P(\mathcal{S}) = \prod_{i \in \mathcal{S}} \sigma_i^z \,, \tag{2.4}$$

creates plaquette defects along the boundary $\partial\mathcal{S}$ of the surface $\mathcal{S}$ (see Fig. 2.4(a)). This is because σ^z acts on an even number of edges of each plaquette cutting $\mathcal{S}$, except for those lying on the boundary $\partial\mathcal{S}$ which only have σ^z acting on one of their edges. Thus this type of surface operator has an energy cost which scales linearly with the length of the boundary $\partial\mathcal{S}$ of the surface.

One of the defining features of the topological order of the 3D toric code is the mutual statistics between the point-like vertex defects and the vortex lines. Moving a vertex defect all the way around a line defect gives a Berry phase of -1. This braiding process is defined as follows. First act on a ground state with the two operators to form $\hat{W}_V(\mathcal{C}_{AB})\hat{W}_P(\mathcal{S}) \mid GS\rangle$ as shown in Fig. 2.4(a). We now take the point defect B and thread it through $\partial\mathcal{S}$, and then annihilate A with B. This results in a string operator $\hat{W}_V(\mathcal{C}_{closed})$ enclosing the plaquette defects on $\partial\mathcal{S}$ as shown in Fig. 2.4(b). The string operator encircling the line defect can be written as a product of plaquette operators $\hat{W}_V(\mathcal{C}_{closed}) = \prod_{p \in \mathcal{R}} B_p$, where $\mathcal{R}$ is any surface bounded by $\mathcal{C}_{closed}$. However, one of the B_p operators in $\mathcal{R}$ will lie on the line defect, and therefore take value -1. Thus braiding the two types of defects leads to a sign of -1.

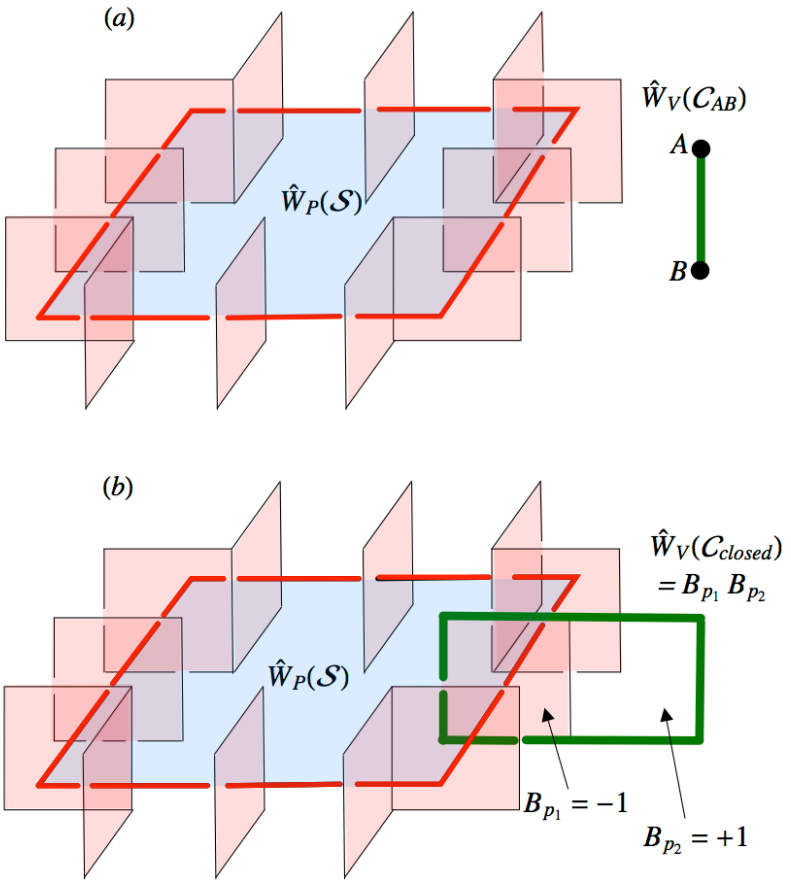


Figure 2.4: This diagram illustrates the braiding between a line defect created by $\hat{W}_P(\mathcal{S})$ and a pair of point defects created by $\hat{W}_V(\mathcal{C}_{AB})$ (shown in (a)) in the 3D toric code. We show the process on a cubic lattice for simplicity, but the same reasoning applies on the trivalent Walker-Wang lattice. The defect B is threaded through the surface $\mathcal{S}$ bounded by the line defect, and annihilated with A. The resulting closed loop (shown in (b)) can be written as a product of plaquette defects, yielding a result of -1 because one of the plaquettes lies on the line defect.

2.2.2 The 3D semion model

We now define the '3D semion model', our first example of a Walker-Wang model which had not previously been examined in the literature. To define the operators in this model, we first fix a projection of the trivalent lattice onto 2D, as shown in Fig. 2.1. (Note that we will always assume the lattice is defined on an orientable manifold.) The Hamiltonian takes the form

$$H = -\sum_v \underbrace{\prod_{s(v)} \sigma_i^z}_{B_v} + \sum_p \underbrace{(\prod_{i\in\partial p} \sigma_i^x)(\prod_{j\in s(p)} i^{n_j})\; i^{\sum_{j\,\mathrm{red}}\, n_\mathrm{j} - \sum_{j\,blue}\, n_\mathrm{j}}}_{B_p}\,, \tag{2.5}$$

where $n = \frac{1}{2}(1-\sigma^z)$ and, as for the 3D toric code, $s(v)$ is the set of three legs attached to vertex v, ∂p is the set of ten edges bounding plaquette p which includes the two privileged blue and two privileged red edges used in the definition of B_p above. $s(p)$ is the set of ten edges radiating from plaquette p (see Fig. 2.5(a)-(c)).

As in 2D, for states $|\Psi_{loop}\rangle$ obeying $B_v|\Psi_{loop}\rangle = |\Psi_{loop}\rangle$ (so-called 'loop gas states'), we can show that

$$[B_p, B_v]\,|\Psi_{loop}\rangle = [B_p, B_{p'}]\,|\Psi_{loop}\rangle = 0\,, \tag{2.6}$$

and furthermore that B_p has eigenvalues ± 1. Thus, if we restrict our Hilbert space to the loop gas states, the Hamiltonian is a sum of commuting operators. Once again, this fact will allow us to solve exactly for the ground state of the Hamiltonian, because we will find that the ground state is a loop gas state. We can also define B_p by using the graphical rules: Thread a string around the boundary of plaquette p as shown in Fig. 2.5(d)-(f), and fuse it into the edges using the graphical rules (Fig. 1.3(d) and (e)). The string will have a choice of under-crossing or over-crossing two edges in $s(p)$; these are the U and O edges marked in Fig. 2.5(d)-(e). In the Walker-Wang prescription the plaquette string will under-cross the U edge, and over-cross the O edge, a choice which ensures adjacent plaquettes commute. Note that in 3D we need to use the crossing rule Fig. 1.3(e) in order to define the plaquette operators graphically, while in 2D we only needed this rule to define the string operators. Unlike the toric code Hamiltonian (2.1), the complex phase in (2.5) ensure that the 3DSem Hamiltonian (and its ground states) are not invariant under complex conjugation.

2.2.2.1 Ground state of 3D semion model on $\mathbb{T}^3$

We first contrast the 3DSem model with the 3D toric code by comparing their ground states. The 3D toric code has a ground state degeneracy of 2^3 on the 3-torus, where

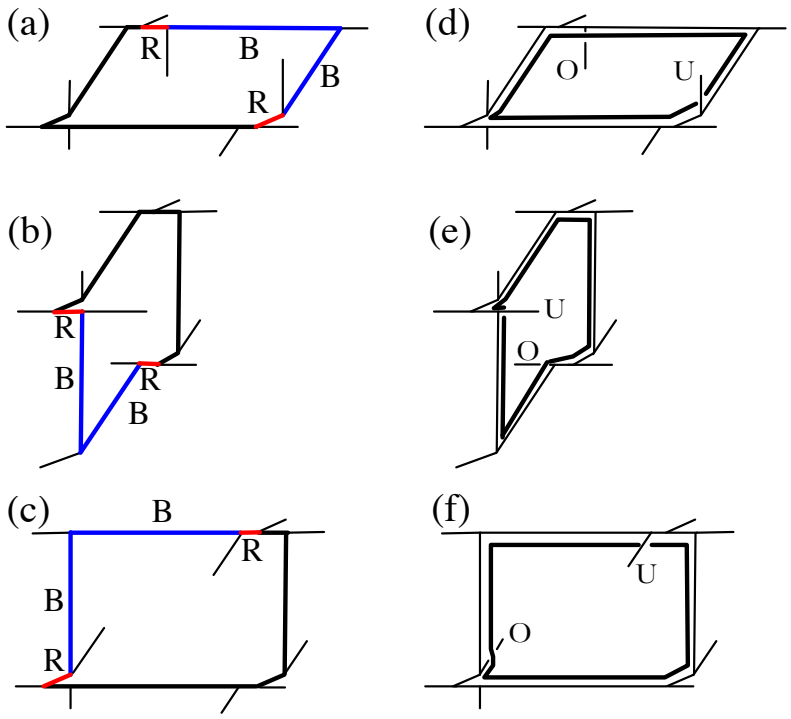


Figure 2.5: (a)-(c) show the three different types of plaquette occurring on the lattice. The edges have been made either black, bold black, bold blue (labelled B) or bold red (labelled R) to aid in the definition of the 3D semion plaquette operator in Eq. (1.4). The set ∂p contains the ten bold edges, while the set $s(p)$ contains the ten black edges. (d)-(f) show how to define B_p operators in terms of a string picture, where it is understood that the string is fused into the edges using Fig. 1.3(d) and (e); notice that the string under-crosses the edge labelled U, but over-crosses the edge labelled O.

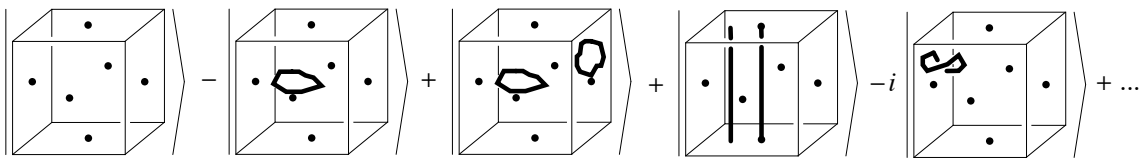


Figure 2.6: This figure shows the unique ground state of the 3D semion model on the 3-torus. It is a superposition of all configurations with all three parities $P_{x_\perp} = P_{y_\perp} = P_{z_\perp} = 1$. To calculate the coefficient of any ket use Fig. 1.3. For example, a ket with a single loop has coefficient -1 using Fig. 1.3(c). One can show that the ket with the twisted loop has coefficient $-i$ by using Fig. 1.3(e) then (c).

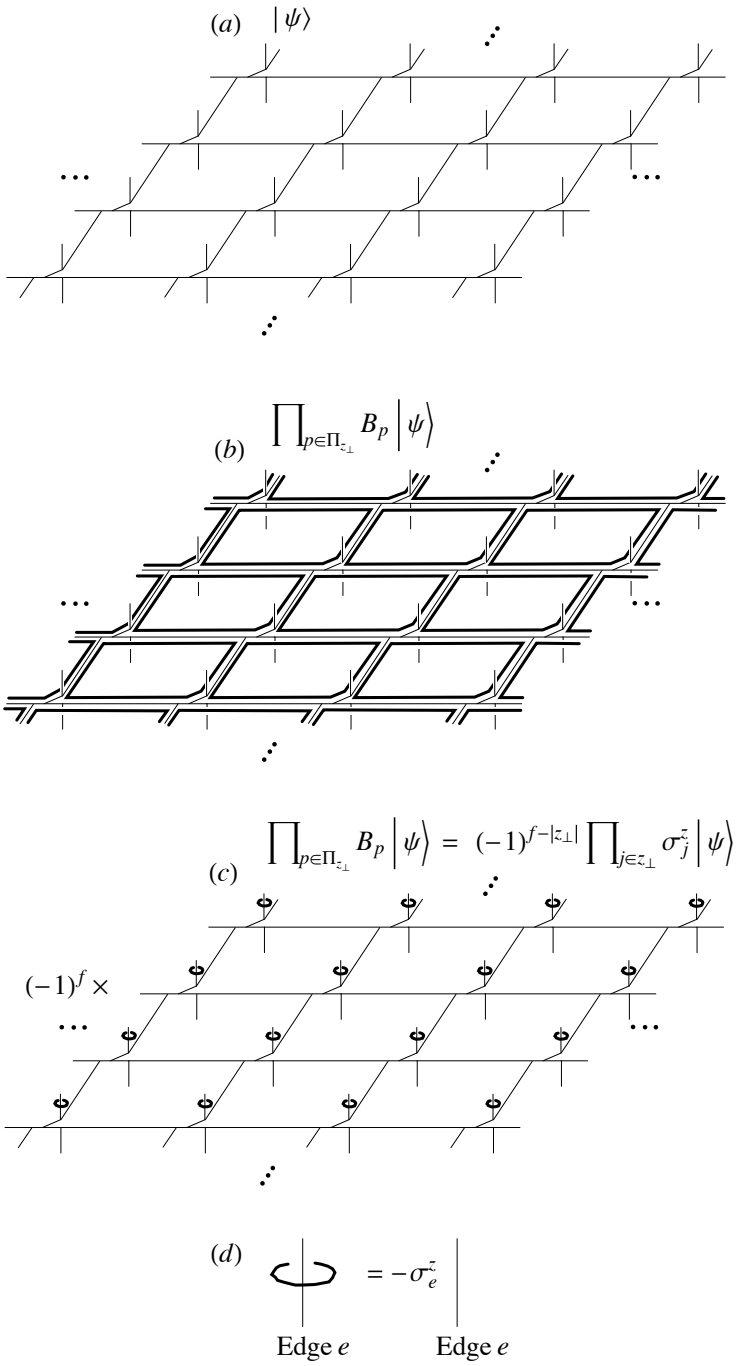
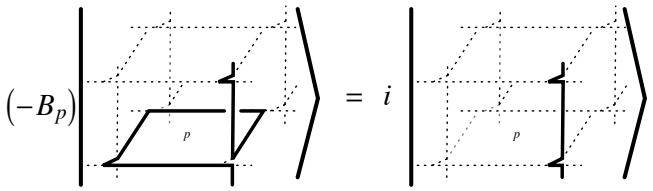


Figure 2.7: Here is the graphical procedure for evaluating the operator $\prod_{p\in\Pi_{z_\perp}} B_p$ on the 3-torus. $\Pi_{z_\perp}$ denotes the set of plaquettes in the plane perpendicular to the $\hat{z}$ direction, while $z_\perp$ represents a set of edges encircled by loops in (c); $|\Pi_{z_\perp}|$ and $|z_\perp|$ represents the sizes of these sets. To begin, we evaluate (b) by fusing each neighbouring string. This yields the picture in (c), where loops are left encircling edges coming up out of the plane, and there is a (-1) factor for each of the f fusions. The loops encircling the vertical legs have the same action as $-\sigma^z$, as shown in (d). This gives $\prod_{p\in\Pi_{z_\perp}} B_p = (-1)^{f-|z_\perp|} \prod_{j\in z_\perp} \sigma_j^z$. Careful counting shows $(-1)^{f-|z_\perp|} = (-1)^{|\Pi_{z_\perp}|}$, giving Eq. (2.9).

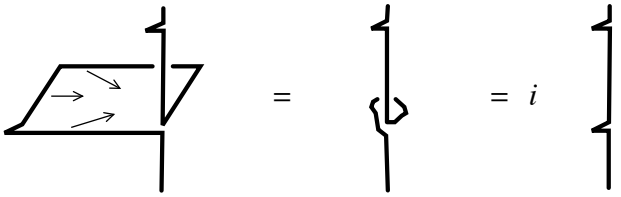
each ground state is labelled by three parity eigenvalues $P_{n_\perp} = \pm 1$ with $n = x, y, z$. We will find that 3DSem has precisely one ground state on the 3-torus, with all three parity values $P_{n_\perp} = +1$.

In analogy with the 2D DSem model, the 3D semion ground state is defined by the conditions $B_v = 1$ and $B_p = -1$ for all vertices and plaquettes. The vertex condition implies that the ground state is a loop gas. In the 2D DSem model, the condition $B_p = -1$ implied that the rules in Fig. 1.3 (b)-(d) related the coefficients of spin configurations. In the 3D semion model, something similar happens: the rules Fig. 1.3 (b)-(d), as well as (e) relate the amplitudes of different configurations in the ground state superposition. To see the rule Fig. 1.3(e) in action, note the equation



, (2.7)

along with the condition $B_p = -1$, implies that the ground state amplitudes of these two configurations are related[2] by a factor of $-i$. This is in accordance with the graphical rules, which tell us that



. (2.8)

In other words, a twist in a loop segment (like that on the left hand side of Eq. (2.7)) should be associated with a phase of $-i$ relative to a straight loop segment (such as the one on the right of Eq. (2.7)). With the aid of these graphical rules, we show that the 3D semion model has a non-degenerate ground state on the 3-torus. In the case of the toric code, there were precisely 2^3 ground states; each ground state was labelled by the three parity eigenvalues ($P_{n_\perp}$, where $n = x$, y or z), and was formed by making an equal amplitude superposition of all configurations related to a canonical ket (with the corresponding parity) by the graphical rules. In the case of the 3D semion model, we can again use local rules to relate any loop configuration to one of the eight canonical configurations in Fig. 2.2, but this only proves that there

[2]Specifically $B_p = -1$ implies the relation $a_L = -ia_R$ between the ground state amplitudes of the configurations on the left (L) and right (R) of Eq. (2.7).

is a ground state degeneracy of at most eight. In fact, there is only a single ground state, which has all $P_{n_\perp} = 1$; it is a superposition of all loop configurations related to Fig. 2.2(a), with relative phases given by the rules Fig. 1.3(b)-(e) as shown in Fig. 2.6.

What happens to the other configurations, which have some $P_{n_\perp} = -1$? None of these configurations occur in a ground state superposition because they are all excited: $P_{n_\perp} = -1$ implies the existence of plaquette defects in the plane perpendicular to the $\hat{n}$-direction. This follows immediately from the identity

$$P_{n_\perp} = \prod_{p \in \Pi_{n_\perp}} (-B_p) \ , \tag{2.9}$$

which we prove graphically in Fig. 2.7, where $\Pi_{n_\perp}$ is the set of plaquettes lying in a plane perpendicular to the $\hat{n}$ direction. We see that any negative parity $P_{n_\perp} = -1$ is incompatible with the ground state conditions that $B_p = -1$ for all p. In order to show that there is a ground state with all $\Pi_{n_\perp} = 1$ we still technically need to prove that the ket Fig. 2.2(a) has some overlap with the ground state. This can be shown by explicitly expanding the ground state projector $\mathcal{P}$, as we do in App. A.6.

Although we have worked specifically with the 3-torus, the above method appears to generalise to any (orientable) manifold without boundary. Hence, as promised, we have shown that the ground state of 3DSem is unique on any (orientable) manifold without boundary – unlike both the 3D toric code, and the 2D semion model.

2.2.2.2 Bulk excitations in the 3D semion model

An important characterisation of topological order is the identification of the low lying excitations and their statistics. In the 3D toric code, the low lying excitations are deconfined point defects, as well as lines of plaquette defects. The 3D semion model is very different because its point defects are confined: We will show that any attempt to separate a pair of point defects leads to the creation of a line of plaquette violations $B_p = 1$ connecting them.

First we note that, unlike in the 3D toric code, flipping spins along a path using $\prod_{i \in \mathcal{C}_{AB}} \sigma^x$ does not produce deconfined point excitations. This operator fails to commute with the B_p along its length due to the σ^z-dependent phase terms in Eq. (2.5). The same kind of issue arose in 2D in the DSem model (Sec. 1.1.2.2), where we found that the string operators producing deconfined point defects were not simply strings of σ^x operators; in addition to flipping the spins along a path, the DSem string operators included compensating phases (depending on the states of edges touching the path) which ensured they commuted with the plaquettes along their length. However,

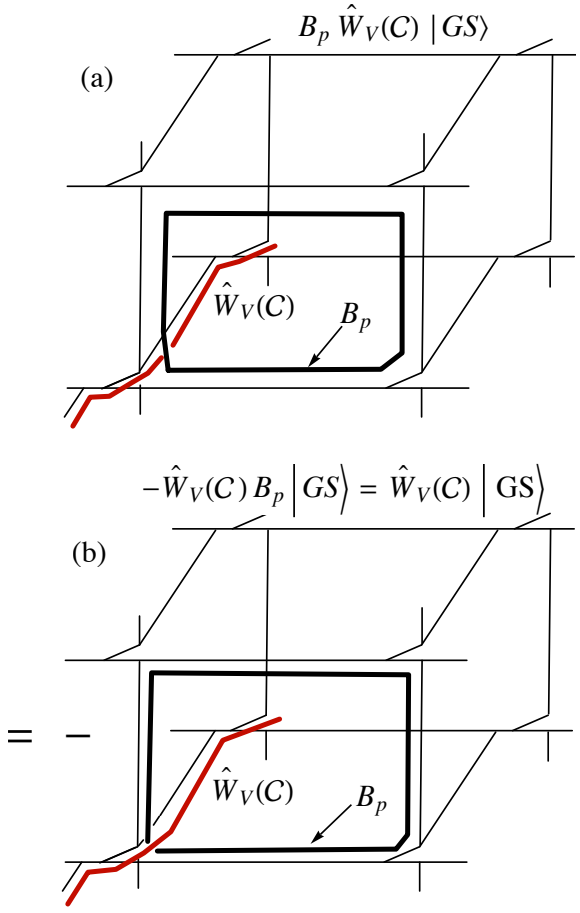


Figure 2.8: This diagram shows how a vertex type string operator $\hat{W}_V(\mathcal{C})$ in the 3D semion model violates any plaquette p it threads. Using the graphical rule in Fig. 1.3(e) shows that the state $B_p\hat{W}_V(\mathcal{C})\mid \mathrm{GS}\rangle$ in (a) is equal to the state $-\hat{W}_V(\mathcal{C})B_p\mid \mathrm{GS}\rangle = \hat{W}_V(\mathcal{C})\mid \mathrm{GS}\rangle$ in (b). Hence $B_p = +1$ on the state $\hat{W}_V(\mathcal{C})\mid \mathrm{GS}\rangle$, and so the string operator has excited the plaquette p out of its low energy state $B_p = -1$ to an excited state $B_p = +1$.

in 3D there is no such assignment of phases, a fact we will prove in Sec. 2.2.2.3. For now, we will demonstrate how a particularly important type of string operator fails to commute with plaquettes along its length.

In the 2D DSem model there was a neat graphical representation for the action of string operators (Sec. 1.1.2.2): lay a string along a path either over or under the lattice, and use the graphical rules Fig. 1.3(b)-(e) to fuse it into the edges. Now attempt to use this prescription in 3D as shown in Fig. 2.8(a): lay a string along a path $\mathcal{C}$ connecting two defects, taking note of which edges the path over and under-crosses, and fuse it into edges using the rules Fig. 1.3(b)-(e) to form an operator $\hat{W}_V(\mathcal{C})$. In addition to flipping spins along the path, the resulting operator includes

phases which ensure it commutes with many of the plaquettes touching $\mathcal{C}$. However, if the path $\mathcal{C}$ threads a plaquette p, as in Fig. 2.8(a), then $\hat{W}_V(\mathcal{C})$ flips the eigenvalue from the low energy state $B_p = -1$ to an excited state $B_p = +1$; we prove this statement in the caption to Fig. 2.8. Thus, attempting to create a pair of point defects with $\hat{W}_V(\mathcal{C})$ leads to a line of plaquette defects.

We might have expected from the outset that point particles are confined in the 3D semion model. In the 2D DSem model, point defects had relative semionic statistics: they were neither fermions nor bosons. The 3D semion model is built on the same semionic graphical rules, so we might have expected point defects in 3D to behave like semions. However, in 3D, *free* point-like particles are either fermions or bosons. The model complies with this requirement by confining the pairs of semionic point particles. Intriguingly, we will later find in Sec. 2.3 that deconfined semionic defects do exist in these 3D lattice models, with the caveat that they are pinned to a boundary.

2.2.2.3 Connection between confinement and non-degeneracy

We saw above that the toric code has degeneracy 2^3 on the 3-torus. This degeneracy is associated with the existence of deconfined point excitations in the following way. If the point defects are deconfined this means they are associated with the endpoints of vertex type string operators which commute with the Hamiltonian, except at their endpoints. Therefore closed string operators that wrap around the non-contractible cycles of the 3-torus have no energy cost. It is easy to see how these operators toggle between the different ground state sectors. For example, acting on the ground state in Fig. 2.3(a) with the operator $\prod_{j\in\mathcal{C}_z}\sigma_j^x$ yields the ground state Fig. 2.3(b), where $\mathcal{C}_z$ is any path that goes once around the z-cycle of the torus, and none of the other cycles. This should be contrasted with the 3D semion model, which has a single ground state on the 3-torus. In this unique ground state, all parities are trivial ($P_{n_\perp} = 1$, Fig. 2.6(a)). This observation proves our previous suggestion that point defects are confined in the bulk of the 3D semion model: if they were not confined, we would be able to form a closed string operator with no energy cost, and use it to thread a single string around a non-contractible cycle in the torus, forming another distinct ground state with non-trivial parity. This would contradict the fact that there is only one ground state.

Unlike the 3D toric code, then, the 3D semion model has no topological order in the conventional sense. Commensurate with this, its bulk entanglement entropy also vanishes, as we show in Appendix A.4. Having established that the 3D semion model is topologically "trivial" on manifolds without boundary, we now turn to study the

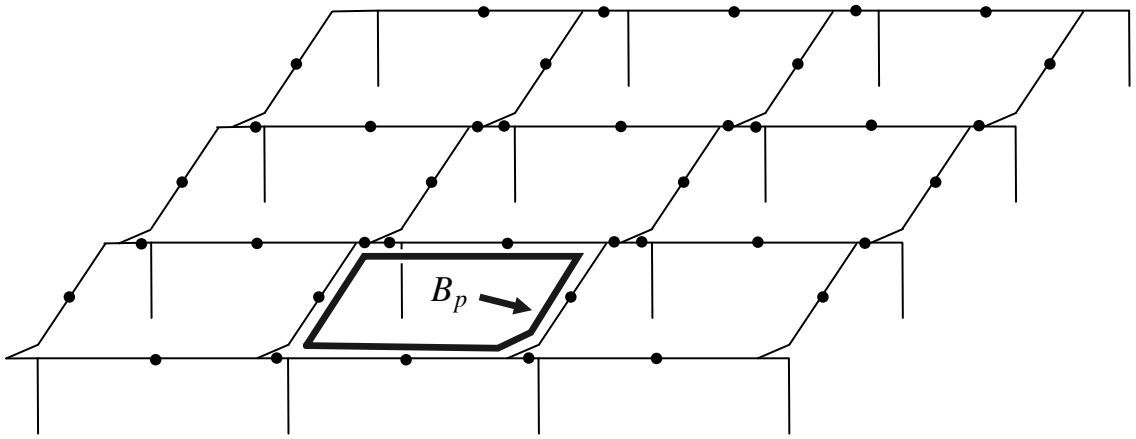


Figure 2.9: This figure shows an example of the surface of a lattice that has been 'smoothly' cut-off. The boundary Hamiltonians of both toric code and 3D semion models will include vertex and plaquette projectors for every (trivalent) vertex and plaquette in the surface.

model on a manifold with boundary, where we will find that its physics is markedly different.

2.3 3D topological lattice models on manifolds with boundary

In the previous section we investigated the 3D semion model on manifolds without boundary; all excitations were confined and we connected this with the uniqueness of the ground state. In this section we investigate the 3D semion model on manifolds with boundary, finding that the presence of the boundary leads to important qualitative changes in the topological order: There exist deconfined chiral anyonic excitations on the surface of the manifold, and these are associated with the existence of multiple ground states. In contrast, the presence of the surface will have little qualitative effect on the topological order in the 3D toric code; in particular, there are no new excitations. This section is organised as follows. In Sec. 2.3.1 we define boundary conditions for the toric code on the solid doughnut, and then describe its ground states and excitations. Then in Sec. 2.3.2 we define the analogous boundary conditions for the 3D semion model, and find that the surface has the same anyon content as a $U(1)_2$ Chern-Simons theory.[3] In particular, there are two ground states which we tie to the presence of deconfined semionic surface excitations. We will then

[3]Here $U(1)_k$ denotes U(1) Chern-Simons theory at level k i.e., $\frac{ik}{4\pi}\int AdA$.

argue in Sec. 2.3.2.2 that adding a chiral 2D anyon layer to this boundary can destroy the topological order associated with the surface.

2.3.1 The toric code on the solid doughnut

In this section we examine the toric code on the solid doughnut manifold $D^2 \times S^1$, where D^2 is a 2D disk and S^1 is a circle. Here we will consider the so-called 'smooth' 3D boundary condition, which is analogous to a well known 2D boundary condition[23, 24]. This smooth boundary is shown for a small (one plaquette thick) version of the solid doughnut in Fig. 2.10(a), and more generally in Fig. 2.9. We discuss an alternative 'rough' boundary condition in App. A.5.

The toric code Hamiltonian is again defined by Eq. (2.1), where v runs over all trivalent vertices, and p runs over all plaquettes, including those plaquettes and vertices lying on the surface of the manifold. The ground state is again defined by $B_v = 1$ and $B_p = 1$. This again implies that the ground state is a loop gas state, and that we can relate different configurations using the graphical rules Fig. 1.3(a)-(d) as before. In the case of the solid doughnut, there are two 'canonical' configurations to which all other loop gas states can be deformed, each distinguished by the winding parity $P_{z_\perp}$. There are 2 ground states labelled by $P_{z_\perp} = \pm 1$, and each is an equal sum superposition of all loop configurations related by graphical rules to the corresponding canonical configuration. These arguments are clearly independent of the number of sites in the lattice, and only depend on the topology of the underlying manifold. The ground state degeneracy is 2^{b_1} on more general manifolds with these boundary conditions, where b_1 is the number of independent non-contractible cycles.

2.3.1.1 Excitations

The excitations of the toric code on the solid doughnut are much the same as they were for the 3-torus. There are deconfined point particles in the bulk and on the surface, created by vertex type string operators $\hat{W}_V(\mathcal{C}) = \prod_{j \in \mathcal{C}} \sigma_j^x$. As before, we are particularly interested in string operators which are closed and non-contractible like $\hat{W}_V(\mathcal{C}_z)$, where $\mathcal{C}_z$ is any path that wraps once around the (non-contractible) z-cycle of the solid doughnut. This operator commutes with the Hamiltonian, but flips $P_{z_\perp}$, so toggles between the two possible ground states.

As on the 3-torus, we can also use operators of the form $\hat{W}_P(\mathcal{S}) = \prod_{i \in \mathcal{S}} \sigma_i^z$ to create lines of plaquette defects along the boundary $\partial\mathcal{S}$ of a surface on the dual lattice $\mathcal{S}$. An interesting feature of our chosen boundary conditions is that $\hat{W}_P(\mathcal{S})$

does not have an energy cost for parts of $\partial\mathcal{S}$ which lie on the surface. We can use this to create open lines of plaquette defects in the bulk, provided they end on plaquette defects on the surface of the manifold. To create a line of plaquette defects connecting surface plaquettes p_1, p_2 along a line $\mathcal{C}'$ in the bulk, find a surface $\mathcal{S}$ which has $\mathcal{C}'$ as part of its boundary. Make the rest of the boundary of $\mathcal{S}$ lie on the surface of the manifold. The resulting operator $\hat{W}_P(\mathcal{S})$ produces the line $\mathcal{C}'$ of plaquette defects ending at p_1, p_2, but no other defects.

In summary, the presence of the surface does not change the nature of defects in the 3D toric code; they still consist of deconfined vertex defects, and linearly confined vortex lines (although these lines can now be open provided they end on the boundary). The excitations are either deconfined vertex defects, or lines of plaquette defects. This is very different to the behaviour of the 3DSem model on the solid doughnut, which we study next.

2.3.2 The 3D semion model on the solid doughnut

Evidently, the presence of a 'smooth' surface has little effect on the toric code; the ground state degeneracy still only depends on the number of independent non-contractible cycles, and we can toggle between all sectors of the ground state by using vertex string operators that lie in the bulk or on the surface. We now contrast this with the 3D semion model, using the same 'smooth' cut-off of the lattice and an analogous boundary Hamiltonian. On the solid doughnut, the 3D semion model has Hamiltonian

$$H = -\sum_{v} B_v + \sum_{p \text{ in bulk}} B_p + \sum_{p \text{ on surface}} B_p^{\text{surf}}, \tag{2.10}$$

where v runs over all trivalent vertices, including those on the surface. For those plaquettes p with both ∂p and $s(p)$ in the bulk, the definition of plaquette operator B_p is as it was in Eq. (2.5). A plaquette p lying near or entirely in the surface will have some edges missing from $s(p)$; the corresponding operator B_p^{surf} is defined simply by omitting these edges from the original definition of B_p in Eq. (2.5). It is easy to show that the new plaquette operators still satisfy $(B_p^{\text{surf}})^2 = 1$, and therefore have eigenvalues ± 1. These boundary conditions are again chosen to gap the surface to vertex and plaquette defects.

Having defined the operators of the Hamiltonian, we note that the ground state is defined by $B_p = -1$ and $B_v = 1$. These conditions again imply that the ground state is a loop gas state, and we can use the graphical rules of Fig. 1.3(a)-(e) to relate the

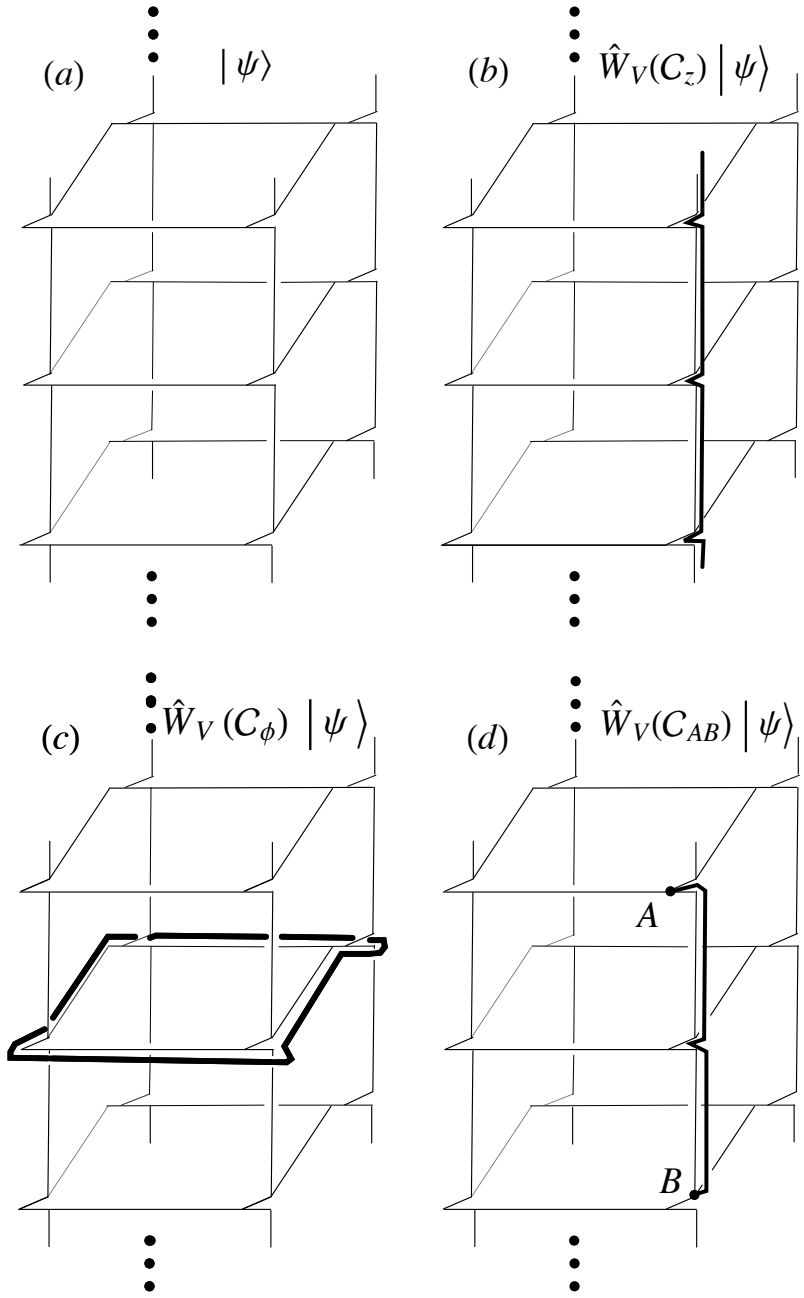


Figure 2.10: (a) Shows a lattice representing a solid doughnut $D^2 \times S^1$ where periodic boundary conditions are enforced in the z-direction. Following that, (b)-(d) show how to define various string operators by laying a string over the lattice and fusing it into the edges using graphical rules. (b) Shows the action of a closed non-contractible string operator $\hat{W}(\mathcal{C}_z)$ that toggles between the two ground states, which are distinguished by whether an odd or even number of strings wind around the z-cycle. (c) Defines the operator $\hat{W}(\mathcal{C}_\phi)$, which also commutes with the Hamiltonian but anti-commutes with $\hat{W}(\mathcal{C}_z)$. (d) Shows how to define deconfined surface excitations at A and B using an open string operator $\hat{W}(\mathcal{C}_{AB})$.

coefficients of different configurations. In the present case there are two 'canonical' states (labelled by $P_{z_\perp} = \pm 1$) to which all other loop configurations can be related using the graphical rules. This suggests that the ground state degeneracy is at most two. In fact it is precisely two, and one can readily prove this using the methods of App. A.6.

2.3.2.1 Surface excitations in the 3D semion model on a manifold with boundary

So far we have shown (see also App. A.6) that the toric code and 3DSem have degeneracy 2 on the solid doughnut. However, they exhibit very different kinds of topological order, a point we clarify by comparing their excitations. In the 3D toric code, point defects are deconfined on the surface and in the bulk. Being deconfined 3D particles, they must be bosonic or fermionic; it is easy to show that they are bosonic. In this section, we show that 3DSem has deconfined vertex defects on the surface of the manifold. The statistics of these surface excitations, and the related ground state degeneracy, are captured by a continuum Chern-Simons topological quantum field theory of form

$$\mathcal{L} = \frac{ik}{4\pi}\epsilon_{\mu\nu\rho}a_\mu\partial_\nu a_\rho + ij_\mu a_\mu \,, \tag{2.11}$$

where we set $k = 2$ (see [25]), and the defects sourced by j_μ are chiral semions. This field theory also describes the anyon content of a $\nu = 1/2$ bosonic Laughlin state. However, we cannot have semions in 3D, only bosons or fermions! The Walker-Wang model complies with this requirement because the vertex defects are confined in the bulk (Sec. 2.2.2.2), and thus effectively pinned to the surface. Thus they are effectively 2D particles, and therefore are allowed to have anyonic statistics.

In the 2D DSem model we found that there were two chiralities of deconfined point defects; positive chirality and negative chirality corresponded to the choice of $+i$ or $-i$ in Eq. (1.9). The string operators creating the point defects had a neat graphical mnemonic demonstrated in Fig. 1.8: To act with a string operator, lay a string along the prescribed path and fuse it into the edges using the graphical rules Fig. 1.3. Positive chirality strings lie above the lattice, while negative ones lie below.

However, on the boundary of 3-manifolds there is only one species of deconfined vertex defect. To create a pair of these vertex defects at A and B, lay a string just outside the surface as shown in Fig. 2.10(d) along a path $\mathcal{C}_{AB}$ connecting A to B, and fuse it into the edges using the graphical rules. (Note that laying the string outside the surface, as opposed to inside, corresponds to a particular choice of phases $\pm i$ when this string crosses a spin-down edge). Such a string operator

($\hat{W}(\mathcal{C}_{AB})$) has phase choices which ensure it commutes with the plaquettes along its length; graphically, this corresponds to the fact that the string does not thread any plaquettes. In contrast, strings lying just beneath the surface necessarily produce confined point excitations because they excite the plaquettes along their length in the same way that bulk string operators do (see Fig. 2.8). This preference for one chirality over the other reflects the fact that the Hamiltonian is not invariant under complex conjugation (because of the i phases appearing in Eq. (2.5)). The chiral phase choice (needed in defining the surface string operators) is such that two vertex string operators on the surface will anti-commute if their paths cross (see Sec. 1.1.2.2). This indicates a sensitivity to the order in which particle pairs are created and destroyed on the surface, and can be used to show that the deconfined surface vertex defects have semionic statistics [12].

These chiral surface vertex defects are deconfined because the surface strings used to create a pair of defects commute with the plaquettes along their length. Therefore if we form a non-contractible surface string $\hat{W}_V(\mathcal{C}_z)$ which winds once around the z-cycle of the torus as shown in Fig. 2.10(b), it will commute with the Hamiltonian and flip the sign of the parity operator $P_{z_\perp}$. This operator toggles between the two ground states mentioned in the previous section.

For the 3D semion model on the 3-torus, we found there was a single ground state and that any state with (for example) $P_{z_\perp} = -1$ is excited. This latter fact followed from Eq. (2.9), which showed that $P_{z_\perp} = -1$ implies the existence of plaquette defects in the $z_\perp$ plane. What is the analogue of Eq. (2.9) on the solid doughnut, and how does it allow a ground state with $P_{z_\perp} = -1$? Using the same methods used to derive Eq. (2.9), we can show that

$$P_{z_\perp} = -\hat{W}(\mathcal{C}_\phi) \prod_{p \in z_\perp \text{ plane}} (-B_p) \ , \tag{2.12}$$

where $\hat{W}(\mathcal{C}_\phi)$ is another string operator on the surface which commutes with the Hamiltonian, defined in Fig. 2.10(c). We see immediately that $P_{z_\perp} = -1$ is not incompatible with the ground state condition $B_p = -1$, provided $\hat{W}(\mathcal{C}_\phi) = 1$. Note that, when there are no plaquette defects, $P_{z_\perp} = -\hat{W}(\mathcal{C}_\phi)$, and so $\hat{W}_V(\mathcal{C}_\phi)$ anti-commutes with $\hat{W}_V(\mathcal{C}_z)$.

2.3.2.2 Other boundary conditions

We have seen that in the presence of a smooth boundary, the 3DSem model is topologically ordered, with a topological ground state degeneracy and deconfined chiral

anyons on the boundary. An exactly solvable zero correlation length (fixed point) [12] model capable of describing chiral topological order is striking: as discussed in the introduction and Chapter 4, there is good reason to believe that such a description is only possible at the boundary of a 3D system.

However, it is certainly possible to generate chiral anyon theories in 2D lattice models that are not fixed point Hamiltonians. Given this, we might ask how robust the surface topological order is to our choice of boundary conditions? One might imagine that the surface topological order can be altered or even destroyed by adding some 2D model to the boundary, i.e., by choosing an appropriate perturbation to the surface of the 3D system.

To destroy the surface topological order, let us begin with a smooth boundary, and add a Laughlin $\nu = 1/2$ quantum Hall system of opposite chirality to the surface. Let the charge of the fundamental boson in the $\nu = 1/2$ layer be q_B. We take the quantum Hall system to have a finite density of charge $q_B/2$ semionic quasi-particles, which are not strongly pinned in space. Next, we perturb the surface Hamiltonian by adding a very strong attraction between the vertex defects on the surface of the 3D model and the quasi-particles of the quantum Hall system in such a way that each quasiparticle will bind exactly one surface vertex defect. The key to altering the surface topological order is that these composite particles have bosonic statistics, because the semionic braiding phases of the vertex defects precisely cancels the phases from the quantum Hall quasiparticle braiding.

We now introduce a kinetic term to the Hamiltonian so as to allow the vertex defects to hop from site to site. We therefore expect that a Bose condensate of these excitations will form at the surface. Interestingly, if we attempt to form a new pair of semions on the surface of the 3DSem model, they braid non-trivially with the condensate and are therefore confined [26]. This confinement ensures that the ground-state degeneracy is lifted, leaving only the even parity ground state ($P_{z_\perp} = 1$).

In summary, unlike in the 3D toric code, the 3DSem model behaves very differently on systems with and without boundaries. In closed systems it appears topologically trivial (unique ground state, confined excitations). With an exactly solvable "fixed point" boundary, however, we find deconfined chiral semions living at the boundary, and a corresponding ground-state degeneracy when the boundary is topologically non-trivial. This topological order, which arises purely at the boundary, can nonetheless be destroyed by adding a sufficiently strong perturbation to the surface.

2.4 General Walker-Wang models

So far we have studied two of the simplest Walker-Wang models, built from the graphical rules in Fig. 1.3. There are many more examples of Walker-Wang models, each based on a different set of self-consistent graphical rules, taking the general form shown in Fig. 2.12; we refer to such a collection of rules as a premodular category (or just 'category' for short). In this section we introduce the general Walker-Wang models in Sec. 2.4.1 and find that, of the many possible models, there is a family which behaves in a similar manner to 3DSem. We call these 'confined Walker-Wang models' because, like 3DSem, all of their bulk excitations are confined. In Sec. 2.4.2 we show that a Walker-Wang model is 'confined' if and only if it is based on a modular tensor category (MTC) (which we define in Sec. 2.4.2).

We then go on to demonstrate that confined Walker-Wang models share many other properties with 3DSem. First we show that the confined models have a unique ground state on the 3-torus in Sec. 2.4.3.1. We then show in Sec. 2.4.3.2 that confined models can have multiple ground states on manifolds with boundary like the solid doughnut, and these degenerate ground states are associated with deconfined anyonic vertex excitations which are pinned to the boundary. These results support the suggestion of Walker and Wang [20] that the lattice models based on certain MTC's (specifically those MTC's coming from a Chern-Simons theory) have surfaces hosting the same anyons as $(2+1)$D Chern-Simons theories.

2.4.1 The general Walker-Wang Hamiltonian, and excitations

The Hilbert spaces of the 3D toric code and 3D semion models consisted of a 2 state system $\sigma^z = \pm 1$ on each edge of the lattice shown in Fig. 2.1, and we represented spin configurations graphically by colouring in only the $\sigma^z = -1$ edges. The ground states were determined by using the graphical rules: Fig. 1.3(a) told us that the ground state involved configurations with an even number of coloured edges coming into a vertex (so the ground state was a 'loop gas'), while the graphical rules Fig. 1.3(b)-(e) provided relationships between the amplitudes of different loop gas configurations.

More general Walker-Wang models are based, in an analogous way, on more complicated sets of graphical rules. For example, probably the next simplest Walker-Wang model is based on the Fibonacci category. The graphical rules for this model are given in Fig. 2.11(a)-(e). The Walker-Wang model based on this category (3DFib)

still consist of a 2 state system $\sigma^z = \pm 1$ on every edge, and again we graphically represent different spin configurations by only colouring in edges with $\sigma^z = -1$. The Hamiltonian (which we define below) is set up so as to ensure the following: The ground state is a superposition of configurations obeying the modified vertex constraints Fig. 2.11(a), and the graphical rules Fig. 2.11(b)-(e) give new linear relations between the amplitudes of different kets in the ground state superposition. As for the semion rules, the Fibonacci rules Fig. 2.11(a) permit vertices with none or two of their incoming edges coloured, and forbid vertices with a single coloured edge. However, unlike the semion rules, the Fibonacci rules also permit vertices with all three incoming edges coloured. This means that the ground state does not quite look like a loop gas – we say that the ground state is a 'string-net' [12] obeying Fig. 2.11(a).

Further generalisations of Walker Wang models can include Hilbert spaces where each edge is in one of k possible states, as compared to the above cases where each edge is in only one of two possible states. More generally, a Walker Wang model can be defined by any 'premodular category' [20]. A 'premodular category' is a set of possible edge labels along with a set of graphical rules (shown in Fig. 2.12) that satisfy certain consistency conditions [27, 28] which we will not enumerate here. For a category with k possible labels, the Hilbert space of the corresponding WW model consists of giving a label $i \in \{0, \ldots, k-1\}$ to each edge in the system.[4]

The general Hamiltonian, which we introduce in the next section, is constructed to ensure two things. Firstly, it ensures that the ground state is a string-net with $k-1$ different 'coloured' strings with labels $\{1, \ldots, k-1\}$ obeying a more general set of vertex constraints represented by Fig. 2.12(a). Secondly, it ensures that the rules Fig. 2.12(b)-(e) give linear relations between the amplitudes of different string-net configurations in the ground state superposition.

2.4.1.1 Hamiltonians

Having explained that all Walker-Wang Hamiltonians are contrived so as to ensure the ground state is described by a set of graphical rules, we now define the Hamiltonians. The details in this section are not essential to understanding the qualitative behavior of confined Walker-Wang models, which we resume studying in Sec. 2.4.3. The casual reader may therefore wish to skip directly to Sec. 2.4.3.

The general Walker-Wang Hamiltonian takes the form

[4] In fuller generality the vertices can also carry a quantum label when the underlying category has 'fusion multiplicities', and the strings can be oriented [28]. We do not consider these subtleties here.

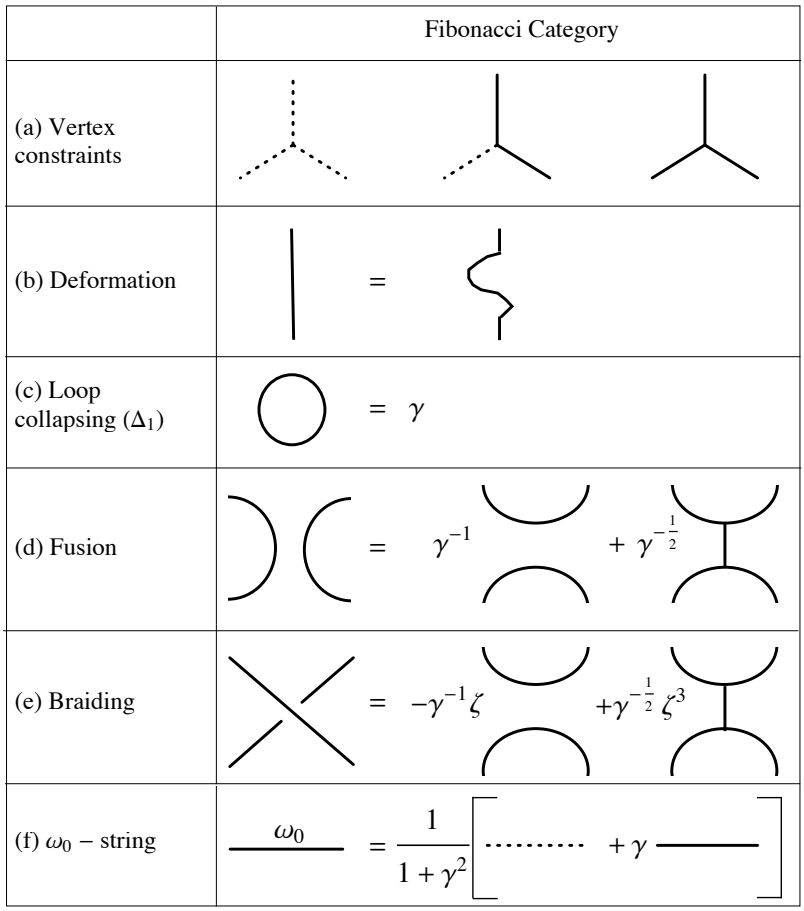


Figure 2.11: The figure above shows the graphical rules for the Fibonacci category, where $\gamma = (1+\sqrt{5})/2$ and $\zeta = e^{i\pi/5}$. (a) represents the fact that the ground state of a Walker-Wang model based on this category is a superposition of configurations involving vertices with either zero, two or three edges coloured in. The rules (b)-(e) give graphical relations between the amplitudes of different spin configurations in the ground state, as well as provide a graphical calculus for defining string operators. Note that there is a rule conjugate to (e) obtained by turning the over-crossing into an under-crossing on the left hand side, and sending $\zeta \to \zeta^* = \zeta^{-1}$ on the right hand side. The string type ω_0 in (f) is used in the definitions of plaquette projection operators.

$$H_{WW} = -\sum_v \mathcal{P}_v - \sum_p \mathcal{P}_p \,, \tag{2.13}$$

where $\mathcal{P}_v, \mathcal{P}_p$ are a commuting set of projectors. The ground state(s) can be found exactly, and has the defining property that $\mathcal{P}_v = \mathcal{P}_p = 1$ for all vertices and plaquettes. The operator $\mathcal{P}_v$ projects onto configurations where only certain combinations of edge colours come into a vertex (see Fig. 2.12(a)), and so the condition $\mathcal{P}_v = 1$ for all v ensures that the ground state is a string-net involving only these types of configurations. The plaquette operators will be defined below, but we reiterate that they are constructed to ensure that Fig. 2.12(b)-(e) relate the amplitudes of different string-net configurations in the ground state.

All that remains is to define the plaquette projectors generally. For explicit expressions for the $\mathcal{P}_p$, we refer readers to [20]; in what follows, we will define the $\mathcal{P}_p$ using a graphical calculus. We saw in the 3D toric code and 3DSem models that there exists a graphical mnemonic for acting with string-operators. Exactly the same mnemonic works here. $\hat{W}_V^i(\mathcal{C})$ denotes an operator formed by laying down a string of type $i \in \{0, 1, \ldots, k-1\}$ along a path $\mathcal{C}$ and fusing it into the edges using Fig. 2.12(b)-(e). While there are only $k-1$ coloured strings in the category, it is notationally convenient to introduce an 'empty' string labelled $i = 0$ with the convention that it braids and fuses trivially with everything, and has $\Delta_{i=0} = 1$ (see Fig. 2.12(c)). This implies that empty string operators always act trivially on the Hilbert space i.e., $\hat{W}_V^{i=0}(\partial p) = \mathbb{I}$.

We now apply this formalism to define the plaquette operators. First we define plaquette operators $\hat{W}_V^i(\partial p)$ for each string type i: Using the fixed projection of the lattice onto 2D, thread a string carrying label i around ∂p using the under and over-crossing prescription shown in Fig. 2.5(d)-(f) and fuse it into the edges of p using the graphical rules (Fig. 2.12(b)-(e)); this prescription ensures that adjacent plaquette operators commute, as shown in Fig. 2.13. Now, the plaquette projector is defined by

$$\mathcal{P}_p = \frac{1}{\mathcal{D}^2} \sum_{i=0}^{k-1} \Delta_i \hat{W}_V^i(\partial p) \tag{2.14}$$

where Δ_i is called the quantum dimension of i (see Fig. 2.12(c)), and $\mathcal{D}^2 = \sum_{i=0}^{k-1} \Delta_i^2$. This operator will sometimes be referred to as $\hat{W}_V^{\omega_0}(\partial p)$, where ω_0 is the superposition of string types

$$\omega_0 = \sum_{i=0}^{k-1} \Delta_i \hat{i} / \mathcal{D}^2 \quad , \tag{2.15}$$

and $\hat{i}$ indicates a string of type i. While the form of this ω_0 operator may seem complicated, it is constructed to have one crucial property, namely the 'handle-slide' property [27] shown and explained in Fig. 2.14. It is precisely this property which ensures that Fig. 2.12(b)-(e) relate the amplitudes of different configurations in the ground state.

2.4.1.2 3DSem in the more general language

Let us now try to understand 3DSem in this new language. The 3DSem category has two string types. There is the 'empty' string carrying label $i = 0$, which for simplicity we did not mention in Fig. 1.3 because it braids and fuses trivially with everything. Then there is the single coloured string type which has label $i = 1$ and has semionic self-braiding Fig. 1.3(e).

The allowed vertices in 3DSem had only an even number of down spins attached to each vertex, which corresponded with $B_v = +1$, where we defined B_v in Eq. (2.5). Therefore we should define $\mathcal{P}_v = (1+B_v)/2$ so that the condition $\mathcal{P}_v = 1$ is equivalent to $B_v = 1$, a condition which ensured that the ground state was a loop gas (see Sec. 2.2.2).

According to Eq. (2.14) the definition of $\mathcal{P}_p$ in DSem is $\mathcal{P}_p = (1 - \hat{W}_V^1(\partial p))/2$, because $\Delta_0 = 1, \Delta_1 = -1$. But we noted in Sec. 2.2.2 that B_p has a graphical definition which is precisely the definition of the string operator $\hat{W}_V^1(\partial p)$. Hence $\mathcal{P}_p = (1-B_p)/2$. Plugging these relations, as well as $\mathcal{P}_v = (1+B_v)/2$, into Eq. (2.13) gives back Eq. (2.5) up to an unimportant re-scaling of the Hamiltonian (and an overall shift of the Hamiltonian by a constant).

2.4.2 Modular tensor categories and excitations

In Sec. 2.2.2.2 we found that the bulk vertex excitations of the 3DSem model were confined, and this was related to the statement that string operators have an energy cost for every plaquette they thread. For these reasons, we called 3DSem a 'confined Walker-Wang model'. We now turn our attention to Walker-Wang models based on modular tensor categories (MTC's). We will show that these are precisely the Walker-Wang models which are confined, in the sense that their string operators have an energy cost for every plaquette they thread.

MTC's are defined as categories with a unitary 'S-matrix' [28]. They have the special property that a loop of the string type used to define $\mathcal{P}_p$ (i.e. $\omega_0 = \sum_i \Delta_i \hat{i}/\mathcal{D}^2$ in Fig. 2.12(f)) kills all flux going through it i.e, using the fusion and braiding rules in

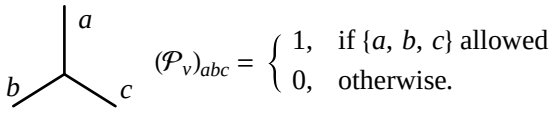
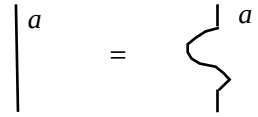
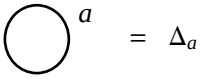
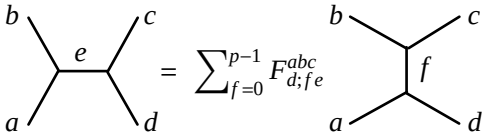
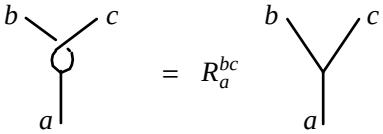
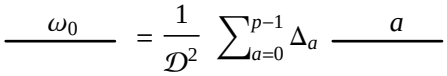
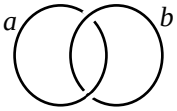
	Premodular category
(a) Vertex constraints	
(b) Deformation	
(c) Loop collapsing	
(d) Fusion	
(e) Braiding	
(f) ω_0 − string	
(g) S-matrix	

Figure 2.12: (a) Represents the vertices allowed by the category; the ground state of a Walker-Wang model will involve only these types of vertices. The diagrams in (b)-(e) serve two purposes. Firstly, they tell us the relative amplitudes of 'string-net' configurations in the ground state e.g. row (c) tells us that configurations related by removing a closed loop carrying label a occur with a relative factor of Δ_a in the ground state. Second, these diagrams provide a neat graphical mnemonic for the definitions of string operators. Note that there is a rule conjugate to (e) obtained by turning the over-crossing into an under-crossing on the left hand side, and sending $R \to R^*$ on the right hand side.

Fig. 2.12 to evaluate Fig. 2.14(b) yields an answer of zero if the flux $i \neq 0$. Examples of MTC's include the semion, Fibonacci, and Ising categories as well as $\mathrm{SU}(2)_n$ for all n [28]. An important non-example is the toric code; we see in Fig. 2.14(c) that a string operator $(1 + \hat{W}_p^1)/2$ does not kill flux going through it.

We can define a string operator $\hat{W}_V^i(\mathcal{C})$ by threading an i string along $\mathcal{C}$, and fusing it into the edges along the path. This produces vertex defects at the end-points of $\mathcal{C}$. For the 3D toric code, such string operators only produced vertex defects at their endpoints. But for 3DSem, the operator also produced plaquette violations along $\mathcal{C}$, which represented the fact that bulk vertex excitations are confined in 3DSem. We will now show that MTC based models behave like 3DSem: Acting on the ground state of any MTC based model with string operator $\hat{W}_V^i(\mathcal{C})$ will excite plaquettes p threaded by the string in addition to creating vertex defects at the ends of $\mathcal{C}$. Put another way, point defects are confined because they are tied to a line of plaquette defects.

The previous paragraph establishes that vertex string operators that act in accordance with the graphical rules produce confined excitations. In App. A.2, we show that this holds for any string operator in a MTC Walker-Wang model, completing the proof that all excitations are confined in the bulk of these models.

Algebraically, confinement means that $\mathcal{P}_p \hat{W}_V^i(\mathcal{C}) \mid \mathrm{GS}\rangle = 0$ for $i \neq 0$, where p is any plaquette threaded by $\mathcal{C}$. We prove this relation graphically in Fig. 2.15(a)-(d). The crucial feature of MTC's is that loops of ω_0 string kill the flux going through them (see Fig. 2.14), and this key property is used to evaluate Fig. 2.15(d). This behavior should be contrasted with that seen for the toric code, which is not based on a modular tensor category. For the toric code we can follow the same reasoning as for a MTC in Fig. 2.15(a)-(d). The difference comes in evaluating diagram (d); in the toric code the ω_0 string does not kill the i flux, it gives back the same answer Fig. 2.15(a) because of the identity shown in Fig. 2.14(c). Algebraically this can be expressed as $\mathcal{P}_p \hat{W}^i \mid \mathrm{GS}\rangle = \hat{W}^i \mid \mathrm{GS}\rangle$, and this implies that the toric code string operator does not produce any plaquette violations along its length, a point we have already discussed in a simpler setting in Sec. 2.2.2.2.

Having seen that all MTC based models are confined, we ask the reverse question: If a category is bulk confined, is it necessarily modular? The answer is yes. If a category is *not* modular, then it can be shown [28] that there must exist a non-vacuum particle which braids trivially with all other particles. If we write down a string operator carrying the label of such a particle, we will find that it commutes with every plaquette projector, and therefore gives rise to deconfined bulk point excitations.

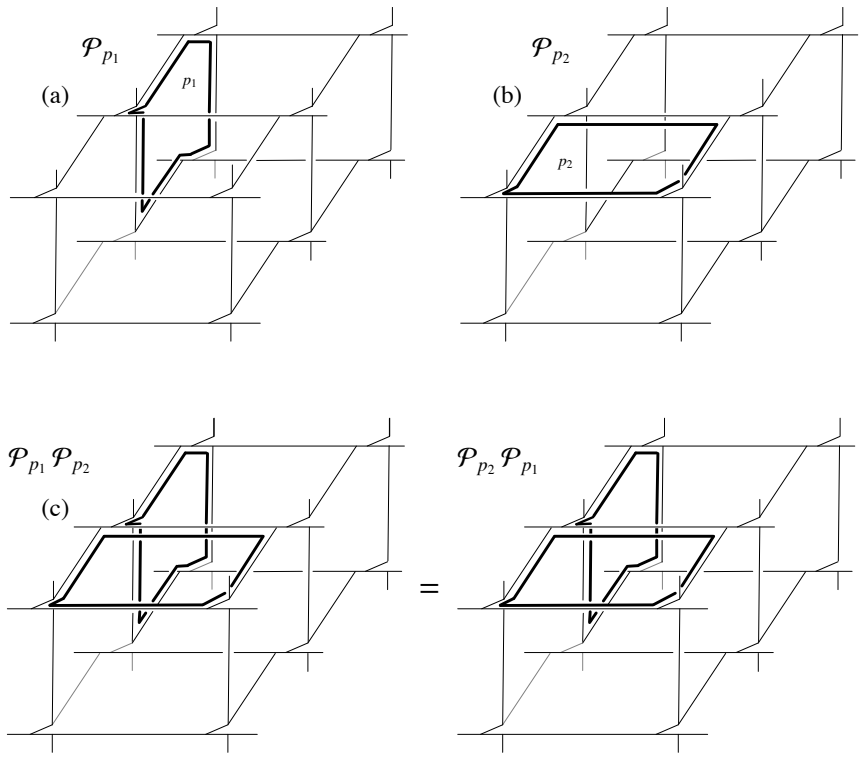


Figure 2.13: This figure shows the graphical definition of plaquette operators in general Walker Wang models. Having fixed a projection of the lattice to 2D, we define a plaquette projector by threading a ω_0 string just inside the perimeter of the plaquette. Two examples are shown in (a) and (b). Then in (c) we show that these adjacent operators commute with each other because the diagrams representing $\mathcal{P}_{p_1}\mathcal{P}_{p_2}$ and $\mathcal{P}_{p_2}\mathcal{P}_{p_1}$ are identical.

Therefore 'not-MTC' implies 'not bulk confined', or equivalently all bulk confined models must be based on MTC's. With the reasoning in the previous paragraph, this implies that a model is bulk confined if and only if it is based on a MTC.

2.4.3 Confined Walker-Wang models on various manifolds

We have shown that string operators in confined Walker-Wang models violate every plaquette they thread. This suggests that confined Walker-Wang models on manifolds without boundary have a unique ground state, an assertion we verify in Sec. 2.4.3.1 (this result is known to the mathematical community [20, 29]). We then go on to show in Sec. 2.4.3.2 that, like 3DSem, confined Walker-Wang models on manifolds with boundary have deconfined anyonic excitations pinned to the boundaries, and that these deconfined excitations are associated with a ground state degeneracy.

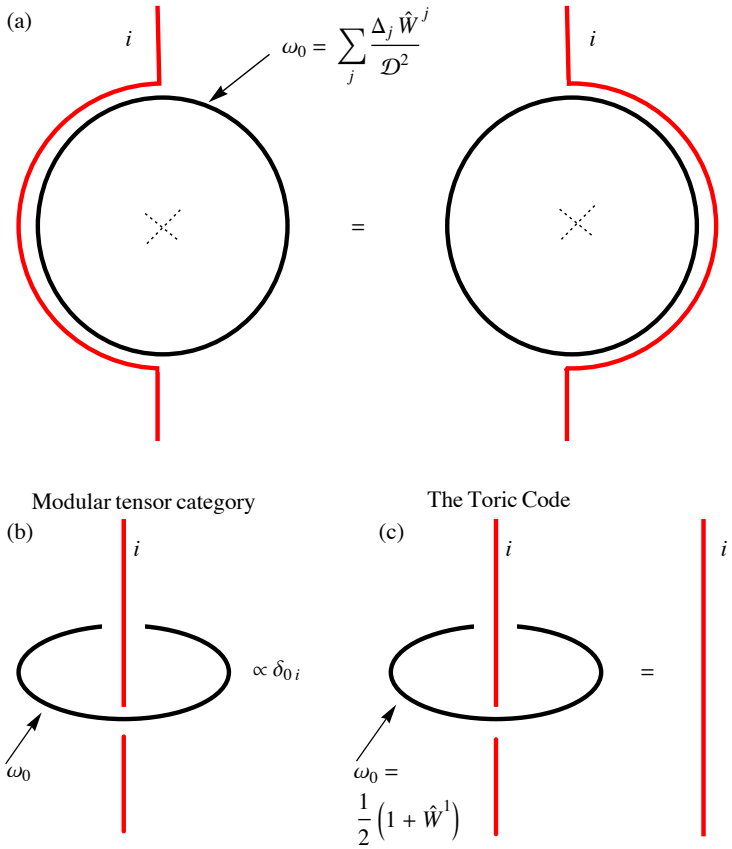
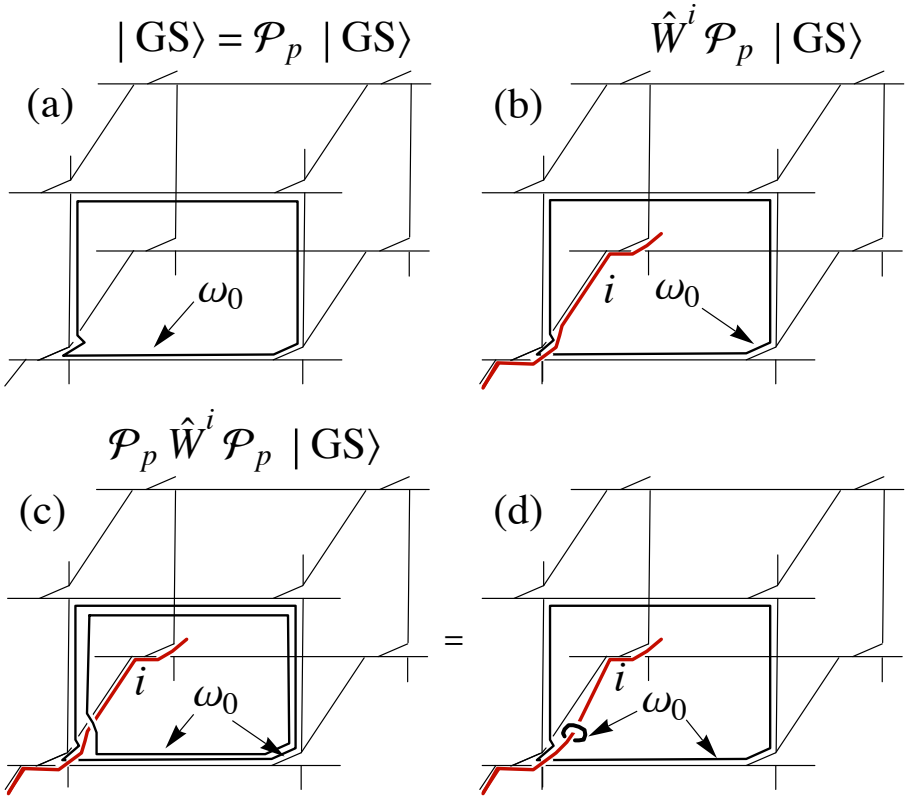


Figure 2.14: (a) demonstrates the handle-slide property of the ω_0 loop which appears in the definition of the plaquette projector. A special property of ω_0 allows us to deform other string operators (or indeed edge strings) i over ω_0 regardless of whether other strings thread ω_0. The X in the middle of the ω_0 loop indicates that other strings may be passing through the middle of the loop. (b) In a modular category, ω_0 loops kill any nonzero flux passing through them. However, in a non-modular category, such as in the toric code (c), this is not the case.

2.4.3.1 The 3-torus

One consequence of bulk confinement is that there are no non-contractible string operators in the bulk that commute with the Hamiltonian of an MTC based model. This naively suggests that the ground state is non-degenerate on manifolds without boundary because there are no operators which commute with the Hamiltonian and toggle between different ground states. We have already written out an argument specific to the 3D semion model, proving that it has non-degenerate ground states on the 3-torus. In App. A.1 we present a general proof that the ground state is non-degenerate on $\mathbb{T}^3$ for *any* modular tensor category. For MTC Walker-Wang models it appears as though the interesting physics occurs on the surface, and not in the bulk.



Toric code: $\mathcal{P}_p\,\hat{W}^i\,\mathcal{P}_p\ |\,\mathrm{GS}\rangle = \hat{W}^i\,\mathcal{P}_p\ |\,\mathrm{GS}\rangle$

MTC: $\mathcal{P}_p\,\hat{W}^i\,\mathcal{P}_p\ |\,\mathrm{GS}\rangle = \delta_{0\,i}\,\hat{W}^i\,\mathcal{P}_p\ |\,\mathrm{GS}\rangle$

Figure 2.15: This diagram shows that acting on the ground state of a lattice model with a string operator carrying label $i \neq 0$ and threading plaquette p will excite the plaquette to $\mathcal{P}_p = 0$ if the underlying category is modular, but will not excite the plaquette if the underlying category is $\mathbb{Z}_2$ (the toric code case). (a) Represents the ground state, which we have acted on with $\mathcal{P}_p$ which equals 1 on the ground state. In (b) we act with a string operator. We then act with plaquette projector $\mathcal{P}_p$ to ascertain the new eigenvalue of $\mathcal{P}_p$ and this forms (c). Using the handle-slide property of the plaquette projectors strings, we handle-slide the inner projector over the outer projector. The result is (d) in which a ω_0-string is left encircling the i-string giving δ_{0i} for a MTC, which is zero because we chose $i \neq 0$.

This motivates the study of a simple manifold with boundary.

2.4.3.2 The solid doughnut $D^2 \times S^1$

We now put a MTC based model on a solid doughnut choosing the 'smooth' boundary conditions shown in Fig. 2.16. These are completely analogous to the smooth boundary conditions described for the 3D toric code and 3DSem model in Sec. 2.3, and are similarly constructed to gap the surface to vertex and plaquette excitations.

As in the case of 3DSem on the doughnut, we can create pairs of deconfined anyons on the surface of the manifold by using graphically defined operators of the form $\hat{W}_V^i(C_{AB})$, where $\mathcal{C}_{AB}$ is a path lying just above the surface of the manifold connecting points A to B and $i \in \{1, \ldots, k-1\}$ is any label in the category. The anyons are deconfined because the path of the string does not thread any plaquettes (see Fig. 2.16(d)).

For such an MTC with $k-1$ non-trivial string types, the ground state degeneracy for the corresponding Walker-Wang model on the solid doughnut is k – exactly that of the chiral anyon theory living on its surface. To see this, note that any ket without vertex violations can be related, using graphical rules Fig. 2.12, to a combination of the k canonical kets shown in Fig. 2.16(b). The ground states labelled by these canonical kets are mutually orthogonal; we can verify this by showing that they have distinct eigenvalues under flux measurement, which involves acting with a closed string operator of the form $\hat{W}_V^{\omega_i}(C_\phi)$ defined in Fig. 2.16(d). Hence there are precisely k distinct ground states, and we can toggle between them using closed string operators of the form $\hat{W}_V^i(C_z)$ (see Fig. 2.16(c)). This is consistent with the degeneracy of 2 found for 3DSem in Sec. 2.3. As a further example, an MTC based on $\mathrm{SU}(2)_n$ has a degeneracy of $n+1$. We note again that the ground state degeneracy is tied to the existence of surface anyon excitations.

2.5 Connection to models with surface quantum Hall anyons

We have seen that the 3DSem model surface has the same anyon content as a $\mathrm{U}(1)_2$ Chern Simons theory, which in turn describes the anyon content of a bosonic Laughlin state at $\nu = 1/2$. In this section we present lattice models whose surfaces resemble more general quantum Hall states. In Sec. 2.5.1 we revisit the 3DSem model. Then in Sec. 2.5.2 we attempt to find a lattice model with the anyon content of a fermionic $\nu = 1/3$ fractional Hall effect. We succeed in part: we find a lattice model with the

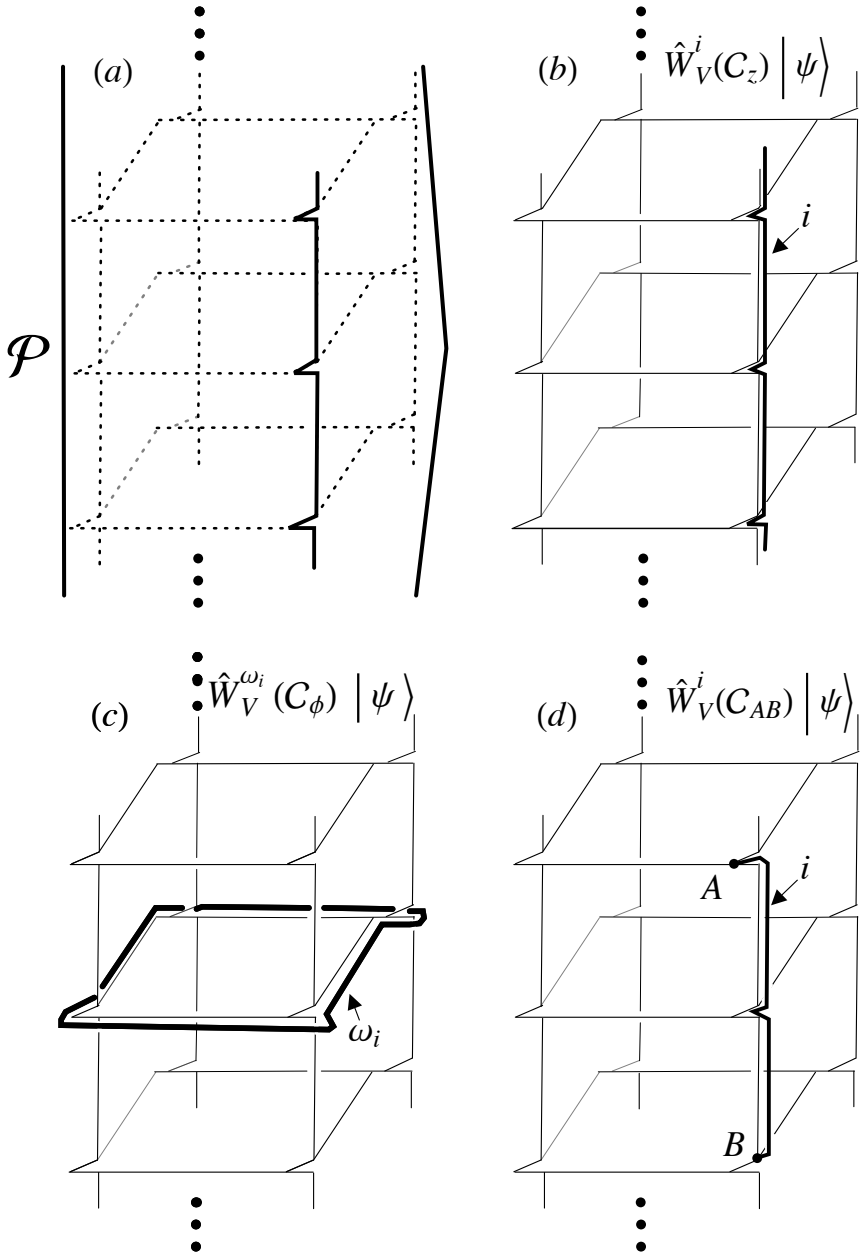


Figure 2.16: (a) Shows the k independent ground states $|\ GS_i\rangle$ where $i \in \{0, 1, 2, \ldots, k-1\}$ and $\mathcal{P}$ is the ground state projector. The dotted lines are edges in state 0 while the bold black edges are in states corresponding to the i-label. (b) Defines a string operator $W_V^i(\mathcal{C}_z)$ winding around the non-contractible z-cycle of the solid doughnut. This operator toggles between ground states e.g., $W_V^i(\mathcal{C}_z)\ |\ GS_0\rangle =|\ GS_i\rangle$. (c) Defines yet another operator $W_V^{\omega_i}(\mathcal{C}_\phi)$ which can be used to distinguish between the different ground states. This operator involves a string type ω_i with a special superposition of labels $\omega_i = \frac{\Delta_i}{\mathcal{D}} \sum_h S_{hi}^* \hat{h}$ where S is the S-matrix of the underlying category. In a MTC, this operator has the property $W_V^{\omega_i}(\mathcal{C}_\phi)\ |\ GS_j\rangle = \delta_{ij}\ |\ GS_j\rangle$. (d) Defines an open string operator, creating defects at A and B but otherwise commuting with the Hamiltonian along its length.

expected deconfined anyons pinned to its surface, but we also find that there exists a deconfined vertex defect in the bulk with fermionic statistics. In Sec. 2.5.2.4 we give a dictionary for going between more general fermionic fractional Hall effects, and a Walker-Wang model with the corresponding anyons on its surface. Once again we find that lattice models with fermionic fractional Hall anyons on their surfaces have a deconfined fermionic vertex excitation in the bulk.

2.5.1 Bosonic $\nu = 1/2$ surface Hall state

The 3DSem model is based on a category called $\mathbb{Z}_2^{(1/2)}$, which has two labels corresponding to the possible anyons in a $U(1)_2$ Chern-Simons theory. For this reason, $\mathbb{Z}_2^{(1/2)}$ is sometimes called $U(1)_2$ [28]. We saw in Sec. 2.3.2.1 that the 3D semion model has surface excitations with semionic statistics – which are described by a $U(1)_2$ Chern-Simons theory [25]. Hence the Walker-Wang model based on category $U(1)_2$ has the same anyons as a $U(1)_2$ Chern-Simons theory, which also has the same anyons as a $\nu = 1/2$ bosonic Laughlin state.

We begin by making more precise the analogy between the surface of the lattice model and a Laughlin state of bosons of charge q_B in a magnetic field. The charge $q_B/2$ excitations have the same semionic statistics as surface vertex defects (corresponding to vertices at the ends of the string operators $\hat{W}(\mathcal{C}_{AB})$ discussed in Sec. 2.3.2.1). The bosonic charge q_B excitations, however, do not exist in the lattice model: excitations that carry charge but no interesting statistics are, in the string-net framework, indistinguishable from the identity. This represents an important difference between the Walker-Wang lattice models of this section and actual quantum Hall fluids: The lattice models have $\mathbb{Z}_n$ rather than U(1) charge conservation. In the present example fusing together two of the $q_B/2$ excitations in the bosonic $\nu = 1/2$ state gives a charge q_B excitation, which is physically measurable but topologically trivial, while in 3DSem fusing the corresponding vertex defects gives the identity – so the lattice model has only $\mathbb{Z}_2$ charge conservation.

2.5.2 Fermionic $\nu = 1/3$ surface Hall state

The 3D semion model has the same anyons as a $\nu = 1/2$ bosonic fractional Hall effect on the boundary of a confining bulk. Can we construct a Walker-Wang model with surface topological order resembling a $\nu = 1/3$ fermionic Hall effect? We will find that there does exist such a model but, unlike 3DSem, it has a deconfined vertex

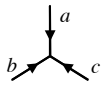
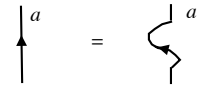
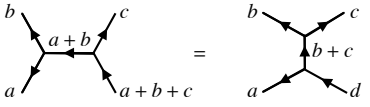
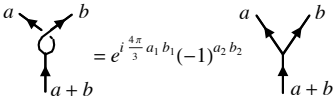
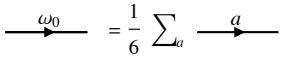
	$\mathbb{Z}_3^{(2)} \times \mathbb{Z}_2^{(1)}$
(a) Labels	$(0,0), (1,1), (2,0), (0,1), (1,0), (2,1)$
(b) Vertex constraints	 $a_1 + b_1 + c_1 = 0 \bmod 3$ $a_2 + b_2 + c_2 = 0 \bmod 2$
(c) Deformation	
(d) Loop collapsing	 $= \Delta_a = 1$
(e) Fusion	
(f) Braiding	 $= e^{i\frac{4\pi}{3}a_1 b_1}(-1)^{a_2 b_2}$
(g) ω_0 − string	
(h) S-matrix	 $= \frac{1}{\sqrt{6}} \begin{pmatrix} 1 & 1 & 1 & 1 & 1 & 1 \\ 1 & \eta & \eta^2 & 1 & \eta & \eta^2 \\ 1 & \eta^2 & \eta & 1 & \eta^2 & \eta \\ 1 & 1 & 1 & 1 & 1 & 1 \\ 1 & \eta & \eta^2 & 1 & \eta & \eta^2 \\ 1 & \eta^2 & \eta & 1 & \eta^2 & \eta \end{pmatrix}$

Figure 2.17: (a) Shows the six possible edge labels of the category. All of the string labels should be viewed as coming from $\mathbb{Z}_3^{(2)} \times \mathbb{Z}_2^{(1)}$. (b) to (f) show the category rules, which we have explained in Sec. 2.4. Note that labels can be added component by component e.g. $a + b = (a_1 + b_1 \mod 3, a_2 + b_2 \mod 2)$. (g) Shows the ω_0-string in the category (which, as always, has the handle-slide property), while (h) shows the S-matrix of the theory (where $\eta = e^{i2\pi/3}$). The columns and rows of the S-matrix are ordered according to the list in (a).

Charge	Exchange Phase	Category Label
0	1	$(0,0)$
$e/3$	$e^{i\pi/3}$	$(1,1)$
$2e/3$	$e^{i4\pi/3}$	$(2,0)$
e	$e^{i\pi}=-1$	$(0,1)$
$4e/3$	$e^{i4\pi/3}$	$(1,0)$
$5e/3$	$e^{i\pi/3}$	$(2,1)$

Table 2.1: This table shows the edge labels in the category $\mathbb{Z}_3^{(2)}\times\mathbb{Z}_2^{(1)}$ used to construct the state with surface resembling a $\nu=1/3$ fermionic Hall effect. Each of the labels in the category correspond with a quasi-particle in the Laughlin $\nu=1/3$ state. The exchange phase is the phase accumulated by exchanging two particles of the same type.

excitation (with fermionic self-braiding) in the bulk which is associated with an additional ground state degeneracy. Therefore, the lattice model does not quite have the topological order of a surface $\nu=1/3$ Laughlin state on a confining bulk.

We choose a category with labels which correspond with the quasi-particle content of the $\nu=1/3$ quantum Hall effect (summarised in Table 2.1). The category is known as $\mathbb{Z}_3^{(2)}\times\mathbb{Z}_2^{(1)}$, and is sometimes labelled by the Chern-Simons theory with corresponding anyon content $\mathrm{U}(1)_3$ [28].

The category in question has labels represented by a doublet $i=(i_1,i_2)$ where i_1 is an integer modulo 3 and i_2 is an integer modulo 2. The Hilbert space thus consists of a 6-state system on each edge of a lattice.[5] The label $(i_1=1,i_2=1)$ represents a Laughlin quasi-particle of charge $e/3$, while $(i_1=0,i_2=1)$ represents a charge e quasi-particle (which, unlike the boson of the $\nu=1/2$ Laughlin state, we must keep track of explicitly because of its fermionic statistics). Excitations such as $(i_1=1,i_2=0)$ can be viewed as the combination of Laughlin charge $e/3$ and charge e quasi-particles. The correspondence between the doublets and the various Laughlin quasi-particles is summarised in Table 2.1.

2.5.2.1 Excitations of the $\mathbb{Z}_3^{(2)}\times\mathbb{Z}_2^{(1)}$ model

In this section we list the excitations present in the Walker-Wang model based on $\mathbb{Z}_3^{(2)}\times\mathbb{Z}_2^{(1)}$. First we discuss the vertex defects, which carry a $\mathbb{Z}_6^{(1)}=\mathbb{Z}_3^{(2)}\times\mathbb{Z}_2^{(1)}$ charge (see Sec. 2.5.1). Unlike the confined Walker-Wang models such as 3DSem, the Walker-Wang model based on $\mathbb{Z}_3^{(2)}\times\mathbb{Z}_2^{(1)}$ has deconfined point-like excitations

[5]Note the strings in this category come with an orientation.

in the bulk and on its surface. The deconfined bulk excitations are fermionic vertex defects that occur at the end-points of strings labelled $(0,1)$. The other four possible vertex defects, which on the surface correspond to Laughlin quasi-particles, or Laughlin quasi-particles bound to electrons, are deconfined only on the surface. This is consistent with the fact that point particles in 3D must be bosons or fermions.

It is enlightening to see how this arises in practice. From the S-matrix (Fig. 2.17(h)) we see that strings carrying label $f = (0,1)$ (f for fermion) braid trivially with all other particles (represented by the fact that the column S_{if} is identical to S_{i0}). This in turn implies that string operators of the form $\hat{W}_V^f(\mathcal{C})$ commute with all the plaquettes along their length because they commute with all the string operators used to define the plaquette operator. On the other hand, all other string types braid non-trivially, so there is only one deconfined vertex defect. Thus the other four types of excitation listed in Table 2.1 are confined in the bulk, but as in the case of MTC based models, they are deconfined on the surface of the manifold.

In the bulk, the four kinds of confined vertex defect are associated with lines of plaquette defects (like those in Sec. 2.2.2.2) which we can think of as 'chiral vortex' lines. However there is another type of confined vortex line which has the same relative statistic with the deconfined $(0,1)$ vertex defects as we found in Sec. 2.2.1.2 between vortex lines and vertex defects in the 3D toric code. We can define this vortex line using a surface operator (see Eq. (2.4)) of the form

$$\hat{W}_P(\mathcal{S}) = \prod_{j \in \mathcal{S}} \widetilde{\sigma}_j^z \,, \tag{2.16}$$

where $\widetilde{\sigma}_j^z$ acts on edge j in the following way: if edge j is in state $i = (i_1, i_2)$ then $\widetilde{\sigma}_j^z = (-1)^{i_2}$. Here $\mathcal{S}$ is a surface on the dual lattice, and the product is over edges cutting the surface transversally. The operator $\hat{W}_P(\mathcal{S})$ creates a line of plaquette violations on its boundary in the manner shown for the 3D toric code in Fig. 2.4. Having understood the spectrum of this Walker-Wang model, we now investigate its properties on some simple manifolds.

2.5.2.2 The $\mathbb{Z}_3^{(2)} \times \mathbb{Z}_2^{(1)}$ model on the 3-torus

The Walker-Wang model based on the $\mathbb{Z}_3^{(2)} \times \mathbb{Z}_2^{(1)}$ category has 2^3 degenerate ground states on the 3-torus, just like the 3D toric code. We will not go through the argument for this result thoroughly, as it strongly resembles those presented for the toric code in Sec. 2.2.1.1, but we emphasise that the ground state degeneracy is associated with

the presence of deconfined excitations. The string operator creating a pair of fermions at either end of a curve $\mathcal{C}$ is:

$$W_V^f(\mathcal{C}) = \prod_{j\in\mathcal{C}} \widetilde{\sigma}_j^x \prod_{\text{crossed edges}} \widetilde{\sigma}_i^z \tag{2.17}$$

where the second product is over edges which are over- or under-crossed by $\mathcal{C}$. Here $\widetilde{\sigma}_j^x$ flips the i_2 label between 0 and 1 on an edge j in state (i_1, i_2), while $\widetilde{\sigma}_j^z = (-1)^{i_2}$. Since W_V^f commutes with the Hamiltonian, as before, one can toggle between the different ground states on the 3-torus using the $\mathbb{Z}_2$ operators $W_V^f(\mathcal{C})$, where $\mathcal{C}$ is a closed path winding around one of the non-contractible cycles of the torus. Furthermore, one can distinguish between the 2^3 different ground states using the new parity operators:

$$\widetilde{P}_{n_\perp} = \prod_{i\in n_\perp} \widetilde{\sigma}_i^z \qquad n = x, y, z \tag{2.18}$$

which take values ± 1 depending on whether an even or odd number of f loops wind around the n-cycle of the torus. Here $n_\perp$ is a set of edges parallel to the $\hat{n}$-direction, whose centers all lie on a plane perpendicular to the $\hat{n}$-direction. This generalises the construction in Eq. (2.2). Having understood the Walker-Wang model on a manifold without boundary, we now investigate its properties on a manifold with boundary.

2.5.2.3 The $\mathbb{Z}_3^{(2)} \times \mathbb{Z}_2^{(1)}$ model on the solid doughnut

In the case of the solid doughnut, the ground state degeneracy is $2 \times 3 = 6$. Heuristically, this result arises for the following reasons. The deconfined fermion can have a parity ± 1 around the single non-contractible direction in the solid doughnut (this gives the factor of 2). To see where the factor of 3 comes from, let us fix the fermion parity. This is like considering a Walker-Wang model based on the category $\mathbb{Z}_3^{(2)}$. As this category is modular [28], and has 3 types of string, we can use the reasoning in Sec. 2.4.3.2 to show that it has a degeneracy of 3 on the solid doughnut associated with the surface deconfined anyons. Therefore, together with the two values of fermion parity, the ground state degeneracy is 6.

Unlike 3DSem, then, the topological order we have found on the solid doughnut does not correspond exactly to that of a quantum Hall state on the boundary of a confining bulk. The discrepancy is due to the fact that we have had to explicitly keep track of the charge e quasi-particle in our category, due to its fermionic statistics – which effectively doubled the number of ground states. The appearance of this deconfined fermionic vertex excitation is not unexpected: if this state does have the

topological order of some system of fermions, then the fermions should be able to exist in the bulk where they would be deconfined in general.

2.5.2.4 More general surface quantum hall states

Having seen how two specific examples give rise to surfaces with topological order resembling fractional Hall states, we briefly summarise how these results generalise. The Walker-Wang model based on category $\mathbb{Z}_k^{(1/2)}$ (also called $\mathrm{U}(1)_k$) for even k (listed in [28]) gives a fully confined bulk, and a surface with the anyons of a $\nu = 1/k$ bosonic Laughlin state.

On the other hand, to obtain surface topological order resembling the fermionic Laughlin states at $\nu = 1/m$ (m odd) we can construct a Walker-Wang model based on category $\mathbb{Z}_m^{(2)} \times \mathbb{Z}_2^{(1)}$, which is sometimes denoted $\mathrm{U}(1)_m$ [28]. As in the case of $\nu = 1/3$, all of these models have their excitations confined in the bulk except for a single deconfined fermionic vertex defect.

It is natural to ask whether this correspondence generalises to more exotic Hall states. Using the 12-particle category in [28] called 'Moore-Read' [30] we can produce a Walker-Wang model with surface Moore-Read anyon content, and a deconfined fermionic vertex in the bulk (labelled $\psi_{(2,4)}$ in the reference). On the solid doughnut, this model has a degeneracy of 12.

2.6 Conclusion

In this chapter, we focussed on two distinct families of topological phases in 3D, exemplified by the 3D toric code and 3DSem models respectively. The first family (which has been studied in a variety of contexts [31, 32]) has a ground-state degeneracy that depends on the topology of the underlying manifold: for example, the ground state is 2^3-fold degenerate on $\mathbb{T}^3$. The excitations of these models can be grouped into point-like defects (which are deconfined everywhere) and vortex loops, and these two types of defects have universal mutual statistics. These features (topological ground state degeneracy, and mutual statistics between point defects and vortex lines) are the most natural extension of the notion of topological order to 3 dimensions.

The second family, however, suggests a different notion of 3D topological order: they have a unique ground state on any closed (orientable) 3-manifold, and all excitations in the bulk are confined. Nonetheless on a manifold with boundary these models can have degenerate ground states, whose number depends on the topology

of the boundary. More than this, their surfaces admit deconfined anyonic excitations. For 3DSem these have (abelian) semionic statistics, but other models exist for which these surface excitations are non-abelian anyons. Hence these are 3D models whose topological characteristics are largely restricted to their boundaries. It is well-established that in some systems, such as topological insulators [33], the low-energy physics at the surface cannot be realised in a purely 2D system. The interesting surface physics of the confined Walker-Wang models appears to play a similar role; they appear to realise chiral topological order with zero correlation length, which cannot be realised in purely 2D. The story is rather subtle, however, and we refer the reader to Chapter 4 for a fuller discussion.

In summary, we have shown that the Walker-Wang Hamiltonians present an interesting playground in which to examine possible 3D topological states of matter, in a context where concrete calculations can be carried out. This raises the interesting possibility that some 3D systems have a topological order confined to their surfaces, while others (such as the fermionic models discussed here in Sec. 2.5) are both topologically ordered in the bulk and at their surfaces. Finally, we might ask what kinds of real physical systems could be expected to share the long-wavelength characteristics of the Walker-Wang models. One possibility, which we explore in the next chapter, is that Walker-Wang models may provide a useful effective description for certain interacting systems with strong spin-orbit coupling [34].

Chapter 3

Walker-Wang models and axion electrodynamics

We now aim to write down field theories realising some of the Walker-Wang models investigated in the previous section. To this end we argue qualitatively, and in some cases more concretely, that the abelian Walker-Wang models of Sec. 2.5 arise in a certain limit of compact axion electrodynamics – specifically, a "dyon condensed" or "obliquely confined" limit, for which composites of bosons and monopoles are condensed. In the process, we make contact with much of the recent work on symmetry protected phases (see [35, 36, 37], and references therein), which we now briefly summarise.

The symmetry protected topological (SPT) phases considered in these references are "trivial" in the bulk (meaning that they have only short-ranged entanglement, and in particular no topological order), but appear to have surfaces that necessarily either (1) break all symmetries; (2) are gapless; or (3) are topologically ordered [37]. In the latter two cases, the surface state realises the residual symmetry in a manner that is "impossible" (i.e., anomalous) in a purely 2D system.

An important part of the effort to understand these new phases has been the identification of model Hamiltonians that can realise them. Though several approaches are possible [36, 38, 39], one approach (which appeared after the work detailed in Chapter 2) is to use Walker-Wang models to obtain symmetry-protected phases [40, 41, 42]. The Walker-Wang models considered in these references are somewhat different from the abelian $\mathbb{Z}_N$ models considered in Chapter 2 because they have additional symmetries, which are realised anomalously on their surfaces.

Not all Walker-Wang Hamiltonians are SPT. For example, the abelian Walker-Wang Hamiltonians in Sec. 2.5 based on the $\mathrm{U}(1)_q$ categories. Said categories describe the anyon content of $\nu = 1/q$ bosonic or fermionic Laughlin states depending on

whether q is even or odd respectively. On the surface, we saw that the corresponding WW ground states have the anyon content of the relevant Laughlin state. In the bulk, the bosonic/fermionic cases have trivial/$\mathbb{Z}_2^{(1)}$ topological order respectively.[1] Neither of these families of models are SPT: the fermionic models are topologically ordered in the bulk, and the gapped surface states of both the bosonic and fermionic models do not appear to realise any global symmetry anomalously.

Here we argue that, rather than being SPT, the abelian quantum Hall models of Sec. 2.5 realise a particular limit of a compact Maxwell theory with bosonic matter sources (of charge p) and a topological θ term

$$\mathcal{L} = \frac{1}{4g^2} F_{\mu\nu} F^{\mu\nu} + \frac{\theta}{32\pi^2} \epsilon_{\mu\nu\rho\lambda} F^{\mu\nu} F^{\rho\lambda} \,. \tag{3.1}$$

Such field theories are of interest in condensed matter, for instance in certain interacting systems with strong spin-orbit coupling [34]. We will argue that the Walker-Wang models describe a phase of this field theory in the limit $g^2 \to \infty$ with $\theta = 2\pi k, k \in \mathbb{Z}$. When k is even and $p = k$, the axion theory bulk is neither SPT nor long-range entangled, but the surfaces have the same anyons as a $\nu = 1/k$ bosonic Laughlin state, just like the $\mathrm{U}(1)_k = \mathbb{Z}_k^{(1/2)}$ Walker-Wang model. When k is odd and $p = 2k$, the axion theory surfaces also have the same anyons as a $\nu = 1/k$ bosonic Laughlin state and $\mathbb{Z}_2^{(1)}$ bulk topological order just like the $\mathrm{U}(1)_k = \mathbb{Z}_k^{(2)} \times \mathbb{Z}_2^{(1)}$ WW model.

Though previous works have offered conjectures about the appropriate (topological) field theory for the Walker-Wang models [1, 20, 43, 44], the present chapter provides a rigorous correspondence between certain Walker-Wang models and "$bF + bb$" topological field theories, and very explicitly identifies them with a particular region of the phase diagram of Eq. (3.1).

Perhaps the most interesting outcome of this correspondence is that it allows us to connect a specific Walker-Wang model based on Fig. 3.4 (which has $\mathbb{Z}_2^{(1)}$ topological order) and the bosonic topological insulator [37, 45] (or BTI). The BTI is a symmetry-protected phase of interacting bosons in which the surface cannot be rendered trivial without breaking a global $\mathrm{U}(1) \rtimes \mathbb{Z}_2^T$ symmetry. The connection is most easily understood using the approach of Metlitski et al. [46], who proposed that Eq. (3.1) with $\theta = 2\pi$ describes the result of gauging the U(1) symmetry of the SPT insulator, and integrating out the fundamental bosons.

[1] Here $\mathbb{Z}_2^{(1)}$ indicates a topological order with one deconfined emergent fermionic charge in the bulk. The paradigm for this topological order is precisely the Walker-Wang model based on the category $\mathbb{Z}_2^{(1)}$ shown in Fig. 3.4.

The Walker-Wang model, it will transpire, describes a limit in which this U(1) gauge symmetry is made compact, and g^2 is made large in the presence of a background of charge $p = 2$ bosonic matter. The bulk $\mathbb{Z}_2^{(1)}$ topological order of the Walker-Wang model is a direct consequence of the fact [46] that in the bosonic topological insulator the magnetic monopole (which one expects to proliferate in the strong-coupling limit, leading to confinement) is a fermion.

This connection between lattice models and the confining phases of the field theory (3.1) also gives us insight into the nature of the models constructed from bosonic Laughlin states, which we identify with confined phases at $\theta = 4\pi n, n \in \mathbb{Z}$. The bulk phase of matter that they realise is, up to a relabelling of its excitations, just the ordinary confined phase of Maxwell theory, which is a prototypically "trivial" phase. The field theory also suggests a path through the phase diagram that could comprise an adiabatic deformation from the Walker-Wang Hamiltonian to the trivial phase.

The remainder of this chapter is set out as follows. We begin in Sec. 3.1 by discussing qualitatively the gapped phases of field theories of the form (3.1). We then identify a limit in which these can be described by a purely topological '$bF + bb$' action; our arguments here are partly heuristic as they do not address certain technical challenges associated with implementing the axion term on the lattice. In Sec. 3.1.4 we briefly summarise the properties of the quantum Hall Walker-Wang models. In Sec. 3.2 we discuss a lattice version of the $bF + bb$ theory, and quantise it to obtain a Walker-Wang Hamiltonian. In Sec. 3.3 we focus on the specific example of the bosonic topological insulator and the corresponding Walker-Wang model, discussing common features between the ground states of the lattice model and the non-linear sigma model that describes the BTI [47]. In Sec. 3.4 we discuss the boundaries of the confined phases. We conclude in Sec. 3.5 with some comments about the generalizability of our results, as well as their implications for the phase diagram of the Walker-Wang lattice models.

3.1 Dyon condensed phases of U(1) electrodynamics with a theta term

In this section, we discuss U(1) gauge theory with a topological θ term $\frac{\theta}{2\pi} = k \in \mathbb{Z}$, and introduce the dyon condensed limit, in which it is well-described by Abelian Walker-Wang Hamiltonians. (This limit has also recently been considered in [48], although in a rather different context.) For k even, these phases are completely

confining in the bulk; for k odd, they will all have $\mathbb{Z}_2^{(1)}$ bulk topological order i.e., $\mathbb{Z}_2$ topological order, but with an emergent deconfined fermion.

The starting point for our analysis is compact U(1) gauge theory coupled to charged bosonic matter, in the presence of an axion term [49, 50]. Later in Sec. 3.2.1 we will discuss a related theory on the lattice. In this section, however, we argue qualitatively using the continuum action

$$S = \int d^4x \left(\frac{1}{4g^2} \Gamma_{\mu\nu}^2 + i \frac{\theta}{8\pi^2} \Gamma \wedge \Gamma - ipA_\mu n^\mu \right) + \mathcal{L}_m \,, \tag{3.2}$$

where $\Gamma_{\mu\nu} = F_{\mu\nu} - 2\pi s_{\mu\nu}$, and $F_{\mu\nu} = \partial_\mu A_\nu - \partial_\nu A_\mu$ is the non-singular part of the field strength, while $s_{\mu\nu}$ accounts for the 2π flux Dirac strings of monopoles that may also be present since the gauge field is compact. We have also defined $\Gamma \wedge \Gamma = \frac{1}{4}\epsilon^{\mu\nu\rho\lambda}\Gamma_{\mu\nu}\Gamma_{\rho\lambda}$. We use a Euclidean space-time metric, such that $Z = e^{-S}$. n^μ is a current of charge p dynamical bosonic matter, while $\mathcal{L}_m$ is an action for this current which we take to be

$$\mathcal{L}_m = K_H n^2 \,. \tag{3.3}$$

This imparts particle world-lines with an energy per unit length of K_H; for the majority of our analysis we work in the limit where $K_H = 0$.

Since the gauge theory is compact, in addition to currents of bosons carrying integral charges, there are currents of monopoles of flux $2\pi\mathbb{Z}$. Throughout this work we will denote a bound state of a charge n boson, and flux $2\pi m$ monopole by (n, m). What difference does the theta term make? When $\theta \neq 0$, a magnetic monopole $(0, m)$ couples to the gauge field as though it has electric charge $q_I = \frac{\theta}{2\pi} m$; we say the monopole has an *induced* electric charge q_I. More generally, the object (n, m) couples to the gauge theory as though it has total electric charge $q_E = n + \frac{\theta}{2\pi} m$. Correspondingly, in the Hamiltonian formulation of the theory, the theta term modifies the Gauss constraint to $\partial_i \hat{E}_i = \rho_b + \frac{\theta}{2\pi}\rho_m$, so that it depends on the monopole number density ρ_m in addition to the boson number density ρ_b. Here we define the electric flux as

$$\hat{E}_i \equiv \hat{\mathcal{E}}_i - \frac{\theta}{4\pi^2} \hat{B}_i \,, \tag{3.4}$$

where $\hat{B}_i \equiv \epsilon_{ijk}\hat{F}_{jk}/2$, and $-\hat{\mathcal{E}}_i \equiv -i\frac{\delta}{\delta \hat{A}_i}$ is the momentum canonically conjugate to $\hat{A}_i$.

In the majority of this chapter, we will assume $k = \theta/2\pi$ is integer valued. Let us compare the theories at $\theta = 2\pi k$ and $\theta = 0$. The allowed particles in both theories are (n, m) where $n, m \in \mathbb{Z}$. One naively expects the physics at $\theta = 2\pi k$ and $\theta = 0$ to be the same: for each particle (n, m) at $\theta = 2\pi k$ there is precisely one particle at

$\theta = 0$, namely $(n + km, n)$, with the same electric charge and magnetic flux. Thus, one expects the physics at $\theta = 2\pi k, 0$ to be the same under the one-to-one relabelling $(n, m) \to (n + km, n)$ [51, 52, 53].

However, [46] (see also [54]) points out that the physics at $\theta = 2\pi k$ and $\theta = 0$ is not quite the same if k is odd. For example, $(-1, 1)$ and $(0, 1)$ have the same electric and magnetic charges at $\theta = 2\pi$ and $\theta = 0$ respectively – they are both electrically neutral and carry unit monopole charge at their respective values of θ. However, the bound state $(-1, 1)$ is a fermion [54], while $(0, 1)$ is a boson. Therefore the $\theta = 2\pi, \theta = 0$ theories are physically distinguishable; in the former $(-1, 1)$ is electrically neutral and fermionic, while in the latter $(0, 1)$ is electrically neutral but bosonic (see Table 3.1). This fact was used ingeniously in [46] to argue that Eq. (3.2) with $\theta = 2\pi$ and small g^2 (weak coupling) describes the electromagnetic response of a bosonic topological insulator.

name	label	q_E	q_M
fundamental monopole	$(0, 1)$	$\frac{\theta}{2\pi}$	1
neutral monopole	$(-\frac{\theta}{2\pi}, 1)$	0	1
fundamental charge	$(1, 0)$	1	0

Table 3.1: Our notation for the point particles in the model Eq. (3.2). The first column shows the label that we will use in the text, which denotes the number of bosonic charges and fundamental monopoles in a given object. This quantity is independent of θ. The second and third columns show the electric and magnetic charges of each object (the former being θ-dependent).

3.1.1 Gapped phases and condensation

The question of which, if any, of these particles condense for a given $(g, \theta, \mathcal{L}_M)$ was addressed by Cardy and Rabinovici [49]; we briefly review their arguments here. The interactions between these point particles can be understood by integrating out A_μ in Eq. (3.2) to obtain

$$\begin{aligned} S &= \int d^4r d^4r' \left[\frac{2\pi^2}{g^2} m_\mu(r) G(r - r') m_\mu(r') \right. \\ &\quad \frac{1}{2} p^2 g^2 j_\mu(r) G(r - r') j_\mu(r') \\ &\quad \left. + 2\pi i p \partial^\nu s_{\mu\nu}(r) n^\mu(r') G(r - r') + \mathcal{L}_m \right] , \end{aligned} \tag{3.5}$$

[49], where we define the total charge current

$$j_\mu(r) = n_\mu(r) + \frac{\theta}{2\pi p} m_\mu(r) , \tag{3.6}$$

and $\delta_{\mu\nu}G(r-r')$ is the photon propagator in the Feynman gauge. The first two terms in Eq. (3.5) represent the Coulomb repulsion between magnetically and electrically charged objects, respectively. The total electric current j^μ contains both the original charge current n^μ and a term $\frac{\theta}{2\pi p}m^\mu$ proportional to the monopole current, indicating that the monopole now carries an induced electric charge of $\theta/(2\pi)$. The third term in Eq. (3.5) is a statistical Berry phase interaction between the matter and monopole currents, which is independent of θ.

Consider a single large current loop. Its Coulomb self-energy is the dominant contribution to its energy per unit length. However, the loop also has an approximately fixed entropy per unit length s_l. As described in [49], the competition between self-energy and entropy leads to an approximate criterion for the condensation of (n, m) current loops

$$\left(\frac{m^2}{\gamma} + (n + \frac{k}{p}m)^2\gamma\right) p < C\,, \tag{3.7}$$

where $\gamma = pg^2/(2\pi)$, $k = \frac{\theta}{2\pi}$, and $C = s_l/\pi G(0)$. We now note a few things about the phase diagram predicted by Eq. (3.7). First, for small g^2 (i.e., small γ), monopoles are heavily penalised and the charge p bosons are condensed forming a $\mathbb{Z}_p$ Higgs phase. At large g^2, on the other hand, the self-energy of any electrically charged object (i.e., objects sourcing E_i field lines in Eq. (3.4)) is large, and only neutral objects for which

$$pn = -km \tag{3.8}$$

can condense. Moreover, if in this limit such a neutral object is condensed, then (i) objects sourcing electric charge are linearly confined and (ii) other electrically neutral objects are deconfined [49]. For $\theta = 2\pi k$, and $p = k$, the fundamental object satisfying Eq. (3.8) is the 'neutral monopole' $(-k, 1)$ – a bound state of a boson with charge $-k$, and a single monopole with equal and opposite induced charge $+k$.[2] Because these electrically neutral objects are bound-states of bosonic charges and fundamental monopoles, we refer to the gapped phases in which they have condensed as dyon condensates. This neutral monopole exists only if our theory contains *dynamical* matter fields of charge (dividing) k. However, in Eq. (3.2) we have explicitly included the factor of p to set the size of the smallest dynamical charge in the theory – thus the neutral monopole can only form if p divides k.[3]

[2]Note, in contrast to [49], in our notation $(1, 0)$ is an object of charge 1, not an object of charge p.

[3]Although p sets the minimum charge of dynamical bosons, in the coming sections we will consider the effect of adding non-fluctuating matter fields (of charge $q \in \mathbb{Z}, 0 < q < p$) as "test charges".

In this work we choose p so as to make contact with the Walker-Wang models. If k is even, we choose $p = k$ which is the largest possible value of p allowing the neutral monopole. The neutral monopole is a boson, and can condense at large g^2; this leads to a phase in which there are no deconfined point particles in the bulk. If k is odd, the neutral monopole is a fermion, and must pair in order to condense. In this case we choose $p = 2k$, which is the largest possible value of p allowing for the formation of *pairs* of neutral monopoles (i.e, $(-2k, 2)$)). The large g^2 phase has $\mathbb{Z}_2^{(1)}$ topological order, much like a superconductor [55].

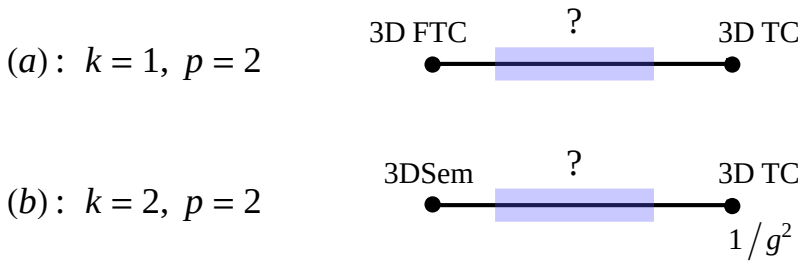


Figure 3.1: Heuristic phase structure as a function of $1/g^2$ for the action in Eq. (3.2). (a): For $\theta = 2\pi, p = 2$, there is $\mathbb{Z}_2^{(1)}$, or fermionic toric code (FTC), topological order for $1/g^2 = 0$ and the usual $\mathbb{Z}_2$ toric code (TC) topological order for $1/g^2 \to \infty$. (b): For $\theta = 4\pi, p = 2$ the theory is confined and has no topological order for $1/g^2 = 0$; we will later identify this limit with the 3DSem model. Again there is TC topological order for $1/g^2 \to \infty$. We do not know the form of the phase diagram for intermediate values of $1/g^2$ (the shaded regions).

It is instructive to consider the phase behaviour as a function of g^2. For $k = 1, p = 2$ (i.e. $\theta = 2\pi$, with a dynamical matter field of charge 2), the (approximate) phase structure is shown in Fig. 3.1 (a). The dyon condensed phase at large g^2 and the Higgs phase at small g^2 are both topologically ordered; however, they have different topological order and are therefore distinct. We will describe the reasons for this in more detail in Sec. 3.1.2. Essentially, however, this is because the Higgs phase admits a deconfined charge 1 bosonic excitation, while the dyon condensed phase (we will find) has a deconfined *fermion*. It is well known that the $p = 2$ Higgs phase is described by the 3D toric code (or $\mathbb{Z}_2$ gauge theory with bosonic charges [31]); we will show in the coming sections that the dyon condensed phase at $\theta = 2\pi$ is described by $\mathbb{Z}_2$ gauge theory with fermionic charges – i.e., by the $\mathbb{Z}_2^{(1)}$ Walker-Wang model, which is just a fermionic variant of the 3D toric code.

For $\theta = 4\pi$, $p = 2$, an approximate phase diagram is shown in Fig. 3.1(b). The Higgs phase here is identical to that for $\theta = 2\pi, p = 2$: the dynamical charge 2 leads

to a gapped phase with the $\mathbb{Z}_2$ topological order of the 3D (bosonic) toric code. For $\theta = 4\pi$ the dyon condensed phase, however, is akin to the usual confined phase at $\theta = 0$, with no topological order or deconfined excitations – we will argue that this limit is captured by the 3DSem model from Sec. 2.2.

For $k > 2$ the Higgs phases are more complicated, with $\mathbb{Z}_k$ ($\mathbb{Z}_{2k}$) topological order for k even (odd). On the other hand, the large g^2 dyon condensed phases follow the same simple pattern: if k is odd, the dyon condensed limit has $\mathbb{Z}_2^{(1)}$ topological order, while if k is even there is no bulk topological order.

3.1.2 Physics in the dyon condensed phases

In this subsection, we discuss in more detail the excitations of the dyon condensed phases with $p = k$ for k even, and $p = 2k$ for k odd. We will see that the spectrum of excitations in these models is described by the $\mathbb{Z}_k^{(1/2)}$ and $\mathbb{Z}_k^{(2)} \times \mathbb{Z}_2^{(1)}$ Walker-Wang models respectively from Sec. 2.5. Then in the remainder of this chapter, we derive some of these Walker-Wang Hamiltonians starting from a lattice gauge theory related to Eq. (3.2), thus making a more concrete connection between certain Walker-Wang models and the gapped phases of axion gauge theories.

Before starting, let us make a technical point which will simplify the following discussion. We stated before that, in the large g^2 dyon condensed regime, excitations of non-vanishing charge q are confined – the energy required to separate two charges $\pm q$ is linear in their separation i.e., their Wilson loops obey an area law.

In fact, this is not quite correct, because we must take account of the background charge p dynamical matter. If p divides q, then the test charges are perfectly screened by the background charge p bosons on large enough length scales[4], and no longer confined. If p does not divide q, the test charges will still be confined, although the charge p matter will serve to reduce the energetically costly electric charge q by multiples of p, so that the screened value of q lies in the set $\{-p/2, 1-p/2, \ldots, -1+p/2\}$ (p is always even in this section). By the same token, the background charge p matter can screen any linearly confined lines of electric flux E_i by multiples of p. Thus, the net electric charge (or flux) after screening only depends on the original value of q (or E_i) modulo p. For this reason, we consider q and E_i to be defined modulo p in the following section.

[4]In the limit considered here, the line tension K_H for the charge p matter is vanishing, and so screening occurs at all length scales

3.1.2.1 k even, $p = k$

We begin by studying the dyon condensed phase for k even, with $p = k$. As discussed above (see Table 3.1), we label a composite of a charge n boson, and flux $2\pi m$ monopole by (n, m). In this notation, for $\theta = 2\pi k$ the composite object $(-k, 1)$ (the 'neutral monopole') has no net electric charge, but carries 2π monopole flux.

As k is an even integer, the neutral monopole $(-k, 1)$ is a boson and can thus condense. The bulk is essentially the usual confined phase of a compact U(1) gauge theory insofar as all test particles carrying nonzero electric charge (which cannot be screened by the dynamical matter) are confined [49, 56]. Thus the allowed test charges $(n, 0)$ with $n \in \{-k/2, \ldots, -1 + k/2\}$ and nonzero are all confined because they cannot be screened perfectly by the background $p = k$ dynamical matter (or similarly, the charge k dynamical monopole). They are associated with open line defects of electric flux $E_i \in \{-k/2, \ldots, -1 + k/2\}$, with $k - 1$ of these non-trivial. It is possible to fuse the ends of these electric flux lines to form closed versions of the same line defects.

This bulk spectrum – with $k - 1$ non-trivial types of open and closed line defects – qualitatively reproduces the bulk spectrum of the confined Abelian Walker Wang models in Sec. 2.5 (specifically those based on $\mathrm{U}(1)_k = \mathbb{Z}_k^{(1/2)}$, with k even). For example, in Sec. 2.2.2, we saw that the spectrum of the 3DSem model ($k = 2$) has a single kind of line defect, which can be open or closed, and which we identify here with the $E_i = -1$ line defect in the gauge theory.

3.1.2.2 k odd, $p = 2k$

For k odd, $(-k, 1)$ is a fermion, and the object that condenses as $g^2 \to \infty$ is the boson $(-2k, 2)$, which has no electric charge, and flux 4π. As a consequence, the bulk spectrum admits a deconfined fermion, analogous to the BdG quasi-particle in a superconductor, and has $\mathbb{Z}_2$ topological order. Indeed, in Sec. 3.2, we will show that for $k = 1$ the lattice model associated with this phase is precisely the $\mathbb{Z}_2^{(1)}$ Walker-Wang model (or "fermionic toric code") which has $\mathbb{Z}_2$ topological order and an emergent deconfined fermion. However, there is an important conceptual difference between the two: in the superconductor, the fundamental charge-carrying object is a fermion. In the models we discuss the charge carriers are *bosonic*; fermions are emergent, arising because the neutral monopole is a composite object when $\theta = 2\pi$.

To make this comparison more precise, let us consider the superconductor in more detail. At long wavelengths there are point-like fermionic excitations (the BdG

quasiparticles) of charge 1 (modulo 2), and vortex lines which carry magnetic flux in integer multiples of π due to the Meissner effect. The BdG quasiparticle acquires a Berry phase of π when it encircles a vortex line carrying an odd-integer multiple of π flux. For a compact theory on the lattice, and in the long wavelength limit, the spectrum consists of one deconfined fermion and a single species of line defect (π flux vortices) [55].

In the limit $g^2 \to \infty$ for $k = 1, p = 2$ in Eq. (3.2), the dyonic condensate is composed of objects carrying twice the fundamental magnetic charge. The result is that the electric field lines are confined to electric tubes carrying integer multiples of $E_i = 1/2$ flux. This is the electromagnetic dual of flux quantisation in a superconductor, and stems from the requirement that the Berry phase of the condensed particle (which has magnetic charge 2) with the electric flux tube must be trivial.

As electric flux is energetically costly for large g^2, we know that the ground state will have $E_i = 0$. Due to the dual Meissner effect (and charge p screening) we expect line-like defects to carry electric flux $E_i \in \frac{1}{2}\{-2, -1, 0, 1\}$. However, the monopole $(0, 1)$ also carries electric charge 1, and must be dynamical as it is a fundamental excitation of the gauge field. So we expect the charge 1 monopoles to screen the energetically costly electric flux lines, so that E_i is reduced in size to $E_i = 0, -1/2$. Therefore, there is effectively only one line defect in this limit: the $E_i = -1/2$ (modulo one) electric flux tube.

What are the possible point-like excitations in the model? As $p = 2$, we need only consider the fate of a pure test charge $(1, 0)$. A pair of $\pm(1, 0)$ (charge 1) bosons will be screened by dynamical monopoles. The resulting composite neutral objects $\pm(1, -1)$ are fermions [54]. These deconfined fermions acquire a Berry phase of π if they encircle a flux tube carrying half-integral electric flux. Hence the dyon condensed phase for $k = 1$ contains only the deconfined $(-1, 1)$ fermion and the $1/2$ electric flux loop. Thus the spectrum is entirely analogous to that of the superconductor, except here the fermion is emergent, and the line defects carry electric rather than purely π magnetic flux.

This result extends to general odd k. Since the monopole carries charge k, the minimal electrically neutral excitation $(-k, 1)$ is a bound state of a monopole with an odd number of bosonic charges. This object is a fermion and cannot condense; instead at large g^2 a condensate of $(-2k, 2)$ will form. The resulting spectrum contains a deconfined fermion $(-k, 1)$ as before, and the dual Meissner effect (and charge p screening) leads to line defects $E_i \in \frac{1}{2}\{-2k, -2k + 1, \ldots, 2k - 1\}$. The dynamical monopole $(0, 1)$ has electric charge k, and so can screen the costly electric flux lines so

that E_i is reduced in size to one of $2k$ possible values $E_i \in \frac{1}{2}\{-k, -k+1, \ldots, k-1\}$, $2k-1$ of which are non-trivial.[5]

There are also, as before, test electric charges $(-k, 0), (-k+1, 0), \ldots, (k-1, 0)$. The $(-k, 0)$ pure charge can be screened perfectly by the charge k monopole, and so becomes the neutral fermion $(-k, 1)$. The remaining $2k-2$ non-trivial test charges cannot be perfectly screened by the monopole, and so live at the ends of open linearly confined electric flux lines. The remaining non-trivial charges are $(\pm 1, 0), ...(\pm(k-1), 0)$. For charge $q > (k-1)/2$, these will be further screened by the $(0, 1)$ monopole to create a composite object of charge $q-k$ bound to a neutral fermion. This gives exactly the low-energy spectrum of the $\mathbb{Z}_k^{(2)} \times \mathbb{Z}_2^{(1)}$ Walker-Wang model in Sec. 2.5.

As an example, let us study the case $k = 3, p = 6$ which corresponds to the Walker-Wang model in Sec. 2.5.2. The non-dynamical charges are $(1, 0), (2, 0), (3, 0) \equiv (-3, 0), (4, 0) \equiv (-2, 0)$ and $(5, 0) \equiv (-1, 0)$. (Here the equivalence indicates the effect of the background charge $p = 6$ matter explained at the beginning of this section). However, screening by the $(0, 1)$ monopole (which has charge 3) will convert these into

$$(\pm 1, 0) \to (\pm 1, 0)\ , \quad (\pm 2, 0) \to (\pm 2, \mp 1)\ , \quad (-3, 0) \to (-3, 1)\,. \tag{3.9}$$

These combine according to the anticipated $\mathbb{Z}_k \times \mathbb{Z}_2$ group structure. The remaining four confined defects have electric charge ± 1, meaning that the energy cost of the electric flux line that connects them is the same in all cases. Table 3.2 gives a few other examples.[6]

k	neutral fermion	Pure charges	Charge-fermion composites
3	$(-3, 1) \equiv (3, -1)$	$(-1, 0), (1, 0)$	$(-2, 1), (2, -1)$
5	$(-5, 1) \equiv (5, -1)$	$(\pm 1, 0), (\pm 2, 0)$	$\pm(-3, 1), \pm(-4, 1)$
7	$(-7, 1) \equiv (7, -1)$	$(\pm 1, 0), (\pm 2, 0), (\pm 3, 0)$	$\pm(-4, 1), \pm(-5, 1), \pm(-6, 1)$

Table 3.2: Spectrum of the dyon condensed phase of axion electrodynamics for $p = 2k$ with $k = 3, 5, 7$. This spectrum contains a deconfined fermion for every k, as well as pure charges which are confined in the bulk, but deconfined on the surface. The total electric charge of any composite object (n, m) in the table is $q_E = n + km$.

[5]Note the half integer electric flux loops are necessarily closed because there are no half-integer charges.

[6]Note that for $k > 3$ not all confined point particles source the same amount of electric flux after screening; hence (unlike in the Walker-Wang model) in the gauge theory some test charges will be more tightly confined than others. This has no interesting qualitative effect on the physics.

3.1.3 An effective topological action for the dyon condensed phases

Having discussed the qualitative physics of the dyon condensed phases, we now derive an effective field theory for Eq. (3.2) in the limit $g^2 \to \infty, \mathcal{L}_m = 0$, with the choice $p = k$ for k even, and $p = 2k$ for k odd. Our derivation is somewhat heuristic: a careful derivation would provide a precise lattice regularisation of the field theory Eq. (3.2).[7] Consider the partition function associated with the effective action (3.2)

$$Z = \int_0^{2\pi} dA \sum_{\{s_{\mu\nu}, n_\mu\}} \exp\Big[- \int \frac{1}{4g^2} \Gamma_{\mu\nu}^2 + \frac{ik}{4\pi} \Gamma \wedge \Gamma - ipA_\mu n^\mu \Big] \tag{3.10}$$

where we use the notation defined below Eq. (3.2). Since at every point we must sum over all possible Dirac strings (i.e. all integer $s_{\mu\nu}$), the partition function is invariant under $F_{\mu\nu} \to F_{\mu\nu} + 2\pi s_{\mu\nu}$. This periodicity in F allows us to re-write the partition function as a (discrete) Fourier series

$$Z = \int_0^{2\pi} dA \sum_{b_{\mu\nu}, n_\mu \in \mathbb{Z}} e^{i \int (b \wedge F + p A_\mu n^\mu)} e^{-\widetilde{S}[b]} \tag{3.11}$$

where

$$\begin{aligned} e^{-\widetilde{S}[b]} =& \int_{-\infty}^{\infty} dQ e^{- \int \left(ib \wedge Q + \frac{1}{4g^2} Q_{\mu\nu}^2 + \frac{ik}{4\pi} Q \wedge Q \right)} \\ =& \exp\left[- \int \left(- \frac{i\pi}{kC} b \wedge b + \frac{2\pi^2}{k^2 g^2 C} b_{\mu\nu}^2 \right) \right] \end{aligned}$$

and $C = 1 + (\frac{2\pi}{g^2 k})^2$. (Such discrete actions are most naturally defined by taking our gauge theory to live on a 4D lattice, as is done for example in [49]. Here for notational simplicity we omit the lattice for the time being, but will re-introduce it later). Eq. (3.10) is therefore equivalent to a theory with the Lagrangian density

$$\mathcal{L} = - \frac{i\pi}{kC} b \wedge b + \frac{2\pi^2}{k^2 g^2 C} b_{\mu\nu}^2 - ib \wedge F - ipA_\mu n^\mu \,, \tag{3.12}$$

where $b_{\mu\nu} \in \mathbb{Z}$ and $F_{\mu\nu} = \partial_\mu A_\nu - \partial_\nu A_\mu$ with $A \in [0, 2\pi)$. In the limit $g^2 \to \infty$ the second term in Eq. (3.12) vanishes. Since we are including dynamical matter, the final step is to integrate out the matter fields. In our model this is straightforward: summing over n_μ quantises F (and consequently A) in units of $2\pi/p$.[8]

[7] Some care must be taken when defining the $F \wedge F$ on the lattice. This subtlety will not qualitatively effect the results of this section, but the correct choice must be made in order to obtain the correct periodicity in b which we require to make contact with the WW models.

[8] For later reference, we note here that in the Hamiltonian formulation of this theory, $\frac{1}{2}\epsilon_{ijk}\hat{b}_{ik}$ will be canonically conjugate to $\hat{A}_i$, and so (as far as the derivation above is valid) it can be identified with $-\hat{\mathcal{E}}_i$ in Eq. (3.4).

So, we see that deep in the dyon condensed phase, in the presence of dynamical matter of charge p, Eq. (3.2) is captured by the topological field theory

$$S_{\text{top}} = -i \int \left[\frac{\pi}{k} b \wedge b + b \wedge F \right] \tag{3.13}$$

where $A \in \frac{2\pi}{p}\{0, 1, \ldots, p-1\}$. The discreteness of various terms in this action implies (at least naively) a periodicity under $b \to b + l$, where $l = \text{lcm}(p, k)$. (On the lattice this periodicity is somewhat subtle; see Appendices B.1, B.2). Thus b is effectively a $\mathbb{Z}_l$ variable, and can be assumed to live in $\{0, 1, \ldots, l-1\}$. To investigate the properties of the action in this limit, it is useful to introduce line and point defects. To this end, we consider an action of the form

$$S_{\text{top}} - i \int \left[J^\mu A_\mu + \frac{\Sigma^{\mu\nu}}{2} b_{\mu\nu} \right] + S_{\text{Source}} \,, \tag{3.14}$$

where $\Sigma_{\mu\nu}$ is a source of line defects, and J^μ a source of point defects. The S_{Source} term assigns an energy to the two kinds of defects. Due to the periodicities of the fields b and A, we will assume $\Sigma^{\mu\nu}, J^\mu$ take values in $\frac{2\pi}{l}\{0, 1, \ldots, l-1\}$ and $\{0, 1, \ldots, p-1\}$ respectively. For simplicity, we will consider static line and point defects, in which case only Σ_{0i}, J_0 are non-vanishing. A natural choice of action for these defects is

$$S_{\text{Source}} = \epsilon_p \int \mathcal{F}(e^{i\Sigma_{0i}}) + \epsilon_V \int \mathcal{G}(e^{i2\pi J_0/p}) \,, \tag{3.15}$$

where ϵ_P is a line tension, and ϵ_V is a particle mass. Here $\mathcal{F}, \mathcal{G}$ are non-negative functions that vanish only if $\Sigma_{0i} = 0, J_0 = 0$ modulo $2\pi, p$ respectively.

3.1.4 Walker-Wang models

In the remainder of this chapter, we will discuss the connection between the field theory Eq. (3.14) and the Walker-Wang topological lattice models based on $\text{U}(1)_k$ categories. In this section, we briefly review some key features of these specific Walker-Wang models; see Sec. 2.5 for a more detailed discussion.

To begin, consider the Walker-Wang model based on the category corresponding to the bosonic Laughlin states. For example, at $\nu = 1/2$ the category is called $\text{U}(1)_2 = \mathbb{Z}_2^{(1/2)}$ and contains one non-trivial particle type, which we associate with the charge $1/2$ quasi-particle. The Walker-Wang model is just the 3DSem model (Sec. 2.2.2), which has trivial confined bulk and surfaces hosting the same anyons as a $\nu = 1/2$ state. More generally, if our category describes an allowed quantum Hall state of bosons (i.e., if the S matrix of the corresponding rational CFT is modular), the corresponding Walker-Wang model has the following properties:

1. There are no deconfined excitations in the 3D bulk.

2. If the 3D lattice has a boundary, then (at least for some boundary conditions) all anyons in the category can appear as deconfined excitations on the boundary.

For example, Walker-Wang models based on the $\nu = 1/2n$ bosonic Laughlin state with n an integer (category $\mathrm{U}(1)_{2n} = \mathbb{Z}_{2n}^{(1/2)}$) has confined bulk, and can have a surface with the anyon content of said Laughlin-state.

If, on the other hand, we choose a fermionic quantum Hall state, such as the $\nu = 1/3$ Laughlin state, then the combination of three $1/3$ quasiparticles gives a fermion that braids trivially with all other anyons. Unlike the boson of the $\nu = 1/2$ Laughlin state, however, a fermion cannot be "trivial" topologically, and must be included in the category [28]. For this reason, the category corresponding the $\nu = 1/3$ is denoted $\mathrm{U}(1)_3 = \mathbb{Z}_3^{(2)} \times \mathbb{Z}_2^{(1)}$ as described in Sec. 2.5.2. The fermionic particle label can be thought of as living in the $\mathbb{Z}_2^{(1)}$ part of the category. More generally, if our category describes an allowed Laughlin quantum Hall state of fermions, the corresponding Walker-Wang model has the properties:

1. There is a single deconfined fermion in the 3D bulk.

2. If the 3D lattice has a boundary, then (at least for some boundary conditions) the anyons in the underlying category (including the fermion) can appear as deconfined excitations on the boundary.

For example, Walker-Wang models based on the $\nu = 1/(2n+1)$ fermionic Laughlin state with n an integer (category $\mathrm{U}(1)_{2n+1} = \mathbb{Z}_{2n+1}^{(2)} \times \mathbb{Z}_2^{(1)}$) has confined bulk, and can have a surface with the anyon content of said Laughlin-state.

These facts suggest the following: for k even, the Walker-Wang model constructed from $\mathrm{U}(1)_k = \mathbb{Z}_k^{(1/2)}$ describes the dyon condensed phase of Eq. (3.2) with $\theta = 2\pi k, p = k$; for k odd, the Walker-Wang model constructed from a fermionic Laughlin state category $\mathrm{U}(1)_k = \mathbb{Z}_k^{(2)} \times \mathbb{Z}_2^{(1)}$ with k odd describes the $\theta = 2\pi k, p = 2k$ dyon condensate. We make this connection more apparent in the next section, and discuss its implications in Sec. 3.5.

3.2 Discrete bF+bb theories and Walker-Wang models

Thus far, we have derived a topological action for the dyon condensed phases of Eq. (3.2). We now show that S_{top} is also the appropriate field theory for the Walker-

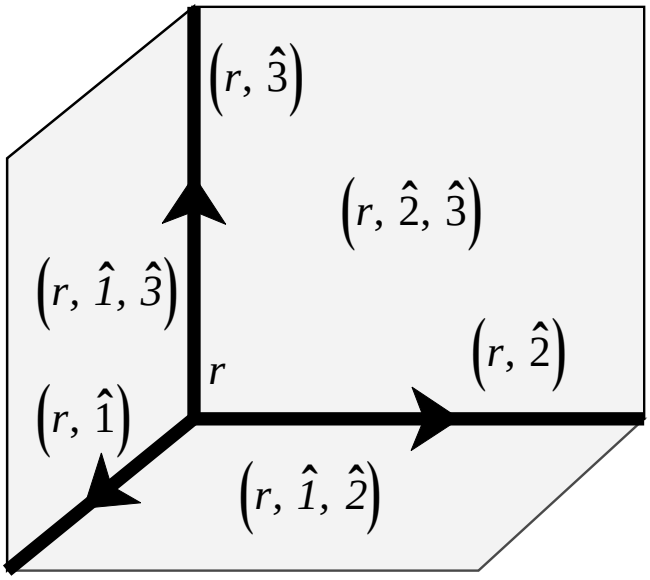


Figure 3.2: This figure illustrates the lattice notation used in this work, where $r = (r^0, r^1, r^2, r^3)$ is a vertex of the 4D lattice, while $(r, \hat{\mu})$ denotes an edge, and $(r, \hat{\mu}, \hat{\nu})$ a plaquette.

Wang models discussed in Sec. 3.1.4, affirming previous conjectures [1, 20, 43, 44]. In this section we show that the $k = 1, p = 2$ $bF + bb$ theory is equivalent to a $\mathbb{Z}_2^{(1)}$ Walker-Wang model. In App. B.1 we explain more generally that for odd k, the $p = 2k$ $bF + bb$ theory is equivalent to a $\mathrm{U}(1)_k = \mathbb{Z}_k^{(2)} \times \mathbb{Z}_2^{(1)}$ Walker-Wang model.[9]

Our approach is as follows. To make a direct connection between S_{top} and the lattice Hamiltonians described in Sec. 2.5, we must put our field theory on a lattice; in Sec. 3.2.1 we describe our conventions for doing this. We then quantise this field theory in Sec. 3.2.2 to derive the Walker-Wang model.

3.2.1 Topological gauge theory on the lattice

We will put our 4D (space + Euclidean time) field theory on the 4D hyper-cubic lattice L. It is convenient to label the vertices by their co-ordinate $r = (r^0, r^1, r^2, r^3)$, and to let $(r, \hat{\mu})$ denote the edge connecting r to $r + \hat{\mu}$. Let $(r, \hat{\mu}, \hat{\nu})$ (with $\mu \neq \nu$) denote the plaquette bounded by $(r, \hat{\mu})$ and $(r, \hat{\nu})$ (see Fig. 3.2).

On each edge $(r, \hat{\mu})$ of L, there is an associated gauge field $A_\mu(r)$. The lattice

[9] As discussed in App. B.2, we are unable to derive the WW model for even $p = k$ due to subtleties involved in defining the field theory on the lattice.

derivative ∂_α is defined by

$$\partial_\alpha T_{\mu\nu\ldots}(r) = T_{\mu\nu\ldots}(r+\hat{\alpha}) - T_{\mu\nu\ldots}(r) \quad \hat{\alpha} = \hat{0}, \hat{1}, \hat{2}, \hat{3} \tag{3.16}$$

where T is an arbitrary vector or tensor field. The value of the electromagnetic field strength on plaquette $(r, \hat{\mu}, \hat{\nu})$ is then given by $F_{\mu\nu}(r) \equiv \partial_\mu A_\nu(r) - \partial_\nu A_\mu(r)$, or more compactly $F \equiv dA$.

In our topological field theory there is another tensor $b_{\mu\nu} = -b_{\nu\mu}$. This field is most naturally viewed as living on the plaquettes of the dual lattice $L^\star$. The vertices of the dual lattice are formed by translating vertices of L by vector $\frac{1}{2}\hat{n}$, where

$$\hat{n} = \hat{0} + \hat{1} + \hat{2} + \hat{3}\ . \tag{3.17}$$

Given a vertex $r^\star$ on the dual lattice, $b_{\mu\nu}(r^\star)$ is the value of b on the $(r^\star, \hat{\mu}, \hat{\nu})$ dual lattice plaquette. A plaquette $(r, \hat{\rho}, \hat{\sigma})$ on the original lattice intersects precisely one plaquette on the dual lattice lying in the $\mu\nu$ plane, where $\epsilon_{\mu\nu\rho\sigma} \neq 0$. We call this dual plaquette $(r^\star(\mu,\nu), \hat{\mu}, \hat{\nu})$ where $r^\star(\mu,\nu) = r + \frac{1}{2}\hat{n} - \hat{\mu} - \hat{\nu}$ is a vertex in L^*. This association between plaquettes and dual plaquettes is used to construct bF type terms, which in this notation take the form

$$\sum_r \frac{1}{4}\epsilon_{\mu\nu\rho\sigma} b_{\mu\nu}(r^\star(\mu,\nu)) F_{\rho\sigma}(r)\,. \tag{3.18}$$

In the field theory (3.14), we also have expressions of the form $b \wedge b \equiv \epsilon_{\mu\nu\rho\sigma} b_{\mu\nu} b_{\rho\sigma}$. These involve terms like $\epsilon_{ijk} b_{ij} b_{0k}$ where b_{0k} lies on time-like plaquettes, while b_{ij} lies on space-like plaquettes. So, which time-like plaquettes should be paired with which space-like plaquettes? It is natural to pair fields on plaquettes that share a vertex, but this still leaves four choices. Here we will use the convention

$$b \wedge b \leftrightarrow \sum_{\mu,\nu,\rho,\sigma} \epsilon_{\mu\nu\rho\sigma} \frac{1}{4} b_{\mu\nu}(r^\star)\, b_{\rho\sigma}(r^\star - \hat{\rho} - \hat{\sigma})\,. \tag{3.19}$$

This prescription coincides with the usual definition of $\epsilon_{\mu\nu\rho\sigma} b_{\mu\nu} b_{\rho\sigma}$ in the naive continuum limit, and defines a symmetric quadratic form for the b's. From this point onwards, we will make a simplifying abuse of notation, and instead denote $b_{\mu\nu}(r^\star(\mu,\nu))$ by $b_{\mu\nu}(r)$ after which, for the record, the $b \wedge F$ and $b \wedge b$ terms become

$$\begin{aligned} b \wedge F &\to \frac{1}{4}\epsilon_{\mu\nu\rho\sigma} b_{\mu\nu}(r) F_{\rho\sigma}(r) \\ b \wedge b &\to \epsilon_{0ijk} b_{ij}(r) \left[\frac{b_{0k}(r + \hat{0} + \hat{k}) + b_{0k}(r - \hat{n} + \hat{0} + \hat{k})}{2} \right]\ . \end{aligned} \tag{3.20}$$

3.2.2 Hamiltonian for $bF + bb$ theory for $k = 1, p = 2$

In this subsection we identify the Hamiltonian describing the dyon condensed bosonic topological insulator starting from the $bF+bb$ field theory (Eq. (3.14)) with $p = 2, k = 1$. A more general derivation for $k \in \mathbb{Z}, p = 2k$ runs along similar lines, and is given in App. B.1. Our method is to write down the partition function, express it as a Trotter decomposition, and from this deduce the effective Hamiltonian.

With $p = 2, k = 1$, the $bF + bb$ Lagrangian density of Eq. (3.14) is

$$\begin{aligned}\mathcal{L} = &-ib \wedge F - i\pi b \wedge b - iJ^0 A_0 - i\Sigma^{0i} b_{0i} \\ &+ \epsilon_V \mathcal{G}(e^{i\pi J^0}) + \epsilon_P \mathcal{F}(e^{i\Sigma^{0i}}) \,, \end{aligned} \tag{3.21}$$

where $F = dA$, $A \in \{0, \pi\}$, and $b_{0i}, \frac{1}{2}\epsilon_{ijk} b_{jk} \in \{0, 1\}$. Both J^0 and Σ^{0i}/π are integers modulo 2, representing static charge and line-defect sources. As they do not explicitly depend on A, b, we will drop $\mathcal{F}, \mathcal{G}$ for now and re-introduce them at a later stage. The first step is to 'integrate out (i.e., sum over) A_0, which imposes the 'Gauss' law constraint' $\epsilon_{ijk}\partial_i b_{jk} = J_0 \mod 2$. Having eliminated the non-dynamical field A_0 at the expense of imposing a constraint, the partition function can now be expressed as

$$\sum_{\{b\}}{}' \sum_{\{\tilde{A}\}} \exp\left[i \sum_r (b \wedge d\tilde{A} + \pi b \wedge b + \Sigma^{0i} b_{0i}) \right] , \tag{3.22}$$

where $\sum'$ is a sum over the constrained b fields, and where $\tilde{A}_\mu$ contains just the space-like components of A_μ.

At this point, it is convenient to introduce a change of variable names. Define Ising fields $\sigma^z, \sigma^x = \pm 1$ living on the space-like edges of the hyper-cubic lattice. (These fields are classical, but the reason for their names will become clear shortly!) Set

$$b_{ij}(r) = \epsilon_{ijk}(1 - \sigma^z_{r,k})/2 \ , \quad A_i(r) = \pi(1 - \sigma^x_{r,i})/2 \tag{3.23}$$

for the space-like components of b and A. In terms of the new variables, the Lagrangian density is

$$\sum_{j=1}^{3} \frac{i\pi}{4}(1-\sigma^z_{r,j})\partial_0(1-\sigma^x_{r,j}) - \sum_{k=1}^{3} i\Sigma^{0k}(r)b_{0k}(r)$$
$$-\sum_{k=1}^{3} \frac{i\pi}{4} b_{0k}(r)\left[(1-\sigma^z_{r-\hat{0}-\hat{k},k})+(1-\sigma^z_{r+\hat{n}-\hat{0}-\hat{k},k})\right]$$
$$-\sum_{i,j,k:\epsilon_{ijk}=1} \frac{i\pi}{4} b_{0k}(r)\left(1-\prod_{e\in\partial(r,\hat{i},\hat{j})}\sigma^x_e\right), \tag{3.24}$$

where $\partial(r,\hat{i},\hat{j})$ denotes the edges in the boundary of plaquette $(r,\hat{i},\hat{j})$. The Gauss constraint can be rewritten $\mathcal{Q}_r \equiv \prod_{e\in s(r)}\sigma^z_e = (-1)^{J_0(r)}$, where $s(r)$ is the set of six space-like edges attached to vertex r. The second step is to sum out the (unconstrained) time-like components of b (i.e., b_{0k}). An integration by parts then gives a partition function

$$\sum_{\{\sigma^z\}}{}' \sum_{\{\sigma^x\}} \prod_{(r,\hat{i},\hat{j})}\left[1+e^{i\pi\Sigma^{0k}(r)}\prod_{e\in\partial(r,\hat{i},\hat{j})}\sigma^x_e \times \sigma^z_{r+\hat{i}+\hat{j},k}\sigma^z_{r-\hat{k}-\hat{0},k}\right]$$
$$\times \exp\left[\sum_{r,i}\frac{i\pi}{4}\left(\sigma^z_{r,i}-\sigma^z_{r-\hat{0},i}\right)(1-\sigma^x_{r,i})\right]. \tag{3.25}$$

Here the first product is over the space-like plaquettes present in the $ij = 12, 23, 31$ planes at every time slice; within this product, the direction $\hat{k} = \hat{1}, \hat{2}, \hat{3}$ is uniquely specified by requiring $\epsilon_{ijk} = 1$. The first line of Eq. (3.25) gives rise to a second constraint

$$\mathcal{B}_{(r,\hat{i},\hat{j})} \equiv \prod_{e\in\partial(r,\hat{i},\hat{j})}\sigma^x_e \times \sigma^z_{r+\hat{i}+\hat{j},k}\sigma^z_{r-\hat{k}-\hat{0},k} = e^{-i\pi\Sigma^{0k}(r)}. \tag{3.26}$$

Using this constraint and the Gauss condition, and re-introducing the ϵ_V, ϵ_P terms from Eq. (3.21) allows us to remove all explicit dependence on Σ_{0i}, J_0

$$\sum_{\{\sigma^z\}}{}' \sum_{\{\sigma^x\}} \exp\left[\epsilon_v \sum_r \mathcal{G}\left(\mathcal{Q}_r\right) + \epsilon_p \sum_{(r,\hat{i},\hat{j})} \mathcal{F}\left(\mathcal{B}_{(r,\hat{i},\hat{j})}\right)\right]$$
$$\times \exp\left[\sum_{r,i}\frac{i\pi}{4}\left(\sigma^z_{r,i}-\sigma^z_{r-\hat{0},i}\right)(1-\sigma^x_{r,i})\right], \tag{3.27}$$

where (without loss of generality[10]) we will take $\mathcal{F}(\kappa) = \mathcal{G}(\kappa) = 2\delta_{\kappa,1} - 1$.

[10] If $\kappa = \pm 1$, then $\mathcal{F}(\kappa), \mathcal{G}(\kappa)$ can be written generally as $\alpha + \beta\delta_{\kappa,1}$

We now express Eq. (3.27) as $\mathrm{Tr}\, e^{-\hat{H}_{\rm eff}\tau}$ where $\hat{H}_{\rm eff}$ is a 3D quantum Hamiltonian. The full details of this procedure are in App. B.1, but here are the key steps. Note that a spin-1/2 system has obvious bases $\hat{\sigma}^\alpha \mid \sigma^\alpha\rangle = \sigma^\alpha \mid \sigma^\alpha\rangle$ for $\alpha = z, x$. It is easy to verify that

$$\langle \sigma'^z \mid \sigma^x\rangle \langle \sigma^x \mid \sigma^z\rangle = \exp\left[\frac{i\pi}{4}\left(\sigma'^z - \sigma^z\right)\left(1 - \sigma^x\right)\right] . \tag{3.28}$$

We can use this identity to replace the last term of the second line in Eq. (3.27) by

$$\prod_n \left\langle \{\sigma^{z,(n)}\} \left| \{\sigma^{x,(n)}\}\right\rangle \left\langle \{\sigma^{x,(n)}\}\right| \{\sigma^{z,(n-1)}\}\right\rangle , \tag{3.29}$$

where $|\{\sigma^\alpha\}\rangle = \otimes_e |\sigma^\alpha_e\rangle$, with e labelling the space-like edges of the cubic lattice. The index n labels the time-slice, corresponding to the r^0 co-ordinate in Eq. (3.27). With care, one can replace appearances of σ^z, σ^x in $\mathcal{B}, \mathcal{Q}$ in Eq. (3.27) with operator insertions of $\hat{\sigma}^z, \hat{\sigma}^x$ between the bras and kets in Eq. (3.29). Effectively the classical variables σ^z_i, σ^x_i are promoted to the quantum mechanical operators $\hat{\sigma}^z_i, \hat{\sigma}^x_i$, obeying the familiar Pauli-matrix commutation relations. Making these replacements, the partition function is a Trotter decomposition of a quantum mechanical problem with Hamiltonian acting on a Hilbert space consisting of a $\sigma^z = \pm 1$ degree of freedom on each edge of a cubic lattice. As explained in Sec. B.1.3, without changing any physics, we can extend this Hilbert space (and the definition of the Hamiltonian) to one living on the point-split lattice, as in Sec. 2.2. On this Hilbert space, the Hamiltonian takes the form

$$\hat{H}_{\rm eff}\Delta\tau = -\epsilon_v \sum_V \underbrace{\prod_{e\in s(V)} \hat{\sigma}^z_e}_{\hat{B}_V} - \epsilon_P \sum_P \underbrace{\prod_{e\in\partial P} \hat{\sigma}^x_e \times \hat{\sigma}^z_{U(P)}\hat{\sigma}^z_{O(P)}}_{\hat{B}_P} , \tag{3.30}$$

where V, P run over all the vertices and plaquettes respectively of the point-split lattice. $\hat{B}_V$ is the same as it was for the toric code in Eq. (2.1). Given a plaquette P, ∂P denotes the ten edges within the boundary of P. There are also two privileged edges $U(P), O(P)$ which depend on whether the plaquette lies in the 12, 23 or 31-plane as shown in Fig. 2.5. $\hat{B}_P$ flips the spins on each of the ten edges in ∂P, and multiplies by a phase $\hat{\Theta}_P = \hat{\sigma}^z_{U(P)}\hat{\sigma}^z_{O(P)}$ which depends on the state of the two $U(P), O(P)$ edges. It is straightforward to verify that Eq. (3.30) is completely equivalent to the Walker-Wang Hamiltonian based on category $\mathbb{Z}_2^{(1)}$ (see Fig. 3.3).

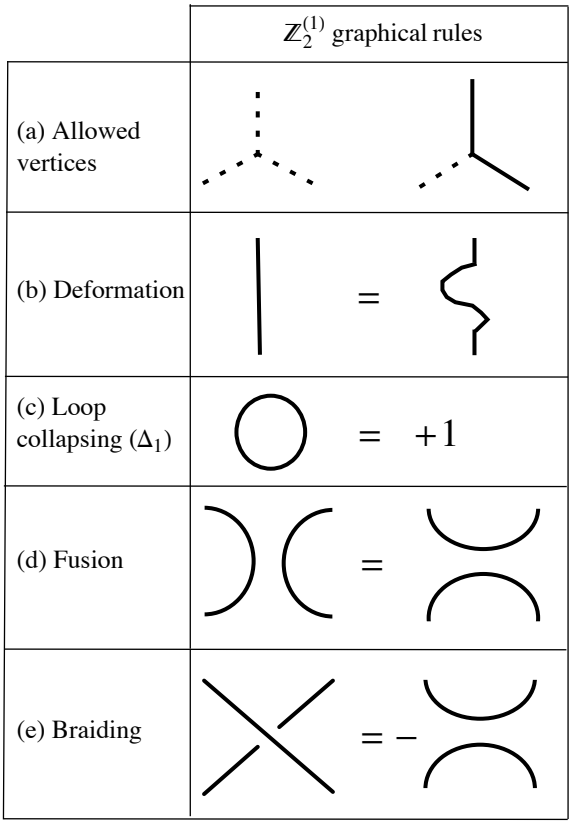


Figure 3.3: This figure shows the graphical rules for the $\mathbb{Z}_2^{(1)}$ category, corresponding to the fermionic toric code Walker-Wang model. (a) represents the fact that the ground state only involves vertices with $B_V = 1$. The diagrams in (b)-(e) tell us the relative amplitudes of loop gas configurations in the fermionic toric code ground state.

3.3 A case study: Relating the $k = 1, p = 2$ dyon condensate to the fermionic toric code.

In the previous section we showed that the $k = 1, p = 2$ $bF + bb$ action exactly describes the Walker-Wang Hamiltonian based on category $\mathbb{Z}_2^{(1)}$ shown in Fig. 3.3. After reviewing some of the properties of the ground states and excitations of this model, we verify that it behaves like the $\theta = 2\pi, p = 2$ dyon condensate described in Sec. 3.1.2.2. Then in Sec. 3.3.4 we connect the ground states of the fermionic toric code to a picture of the bosonic topological insulator ground state derived from a non-linear σ-model [47].

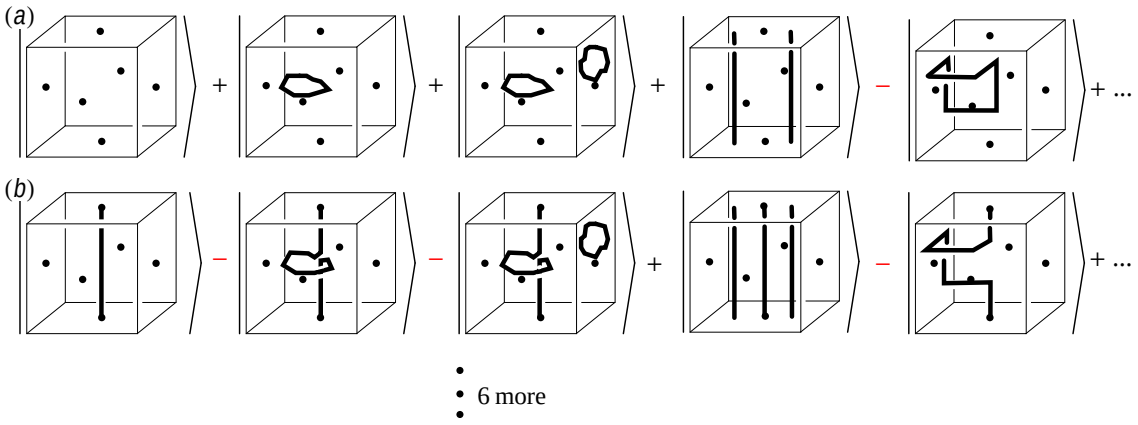


Figure 3.4: This figure shows two of the 2^3 FTC ground states on the 3-torus, with the underlying lattice not drawn, for simplicity. The ground states are distinguished by whether an even or odd number of loops wind around the non-contractible cycles of the torus. Configurations with an odd 'over-crossing parity' appear with -1 amplitude in the ground state superposition.

3.3.1 Ground states

Following our method in Chapter 2, the ground states of the $\mathbb{Z}_2^{(1)}$ Walker-Wang model contain an equal sum superposition of closed loops, with amplitudes determined by the graphical rules Fig. 3.3(b) - (e). These rules are almost equivalent to those of the toric code Fig. 1.3, except for rule (e) which implies that each over-crossing in a loop configuration is associated with a sign of -1. So, to form the ground state, start with any configuration of closed loops $|\{\sigma^z\}\rangle$, and generate related configurations by acting on it with all possible combinations of Fig. 3.3(b) - (e). Sum up all the generated configurations, remembering to weight them with a $+1/-1$ coefficient if they have even/odd number of over-crossings (Fig. 3.4). There is a ground state degeneracy on non-simply connected manifolds because not all closed loop configurations are related by the graphical rules. For example, on the 3-torus, Fig. 3.3(b) - (e) cannot change the number of loops modulo 2 winding around the non-contractible cycles of $\mathbb{T}^3$ (Fig. 3.4). This leads to an 2^3-fold ground state degeneracy on $\mathbb{T}^3$, with each ground state labelled by the three independent winding number parities.

3.3.2 Excitations

Here we briefly overview the properties of the excitations. The Hamiltonian Eq. (3.30) has two types of excitations: pairs of vertex defects where $\hat{B}_V = -1$, and loops of plaquettes defects ('vortex lines') where $\hat{B}_P = -1$. As in the standard toric code [21], vertex defects acquire a π berry phase under encircling a line of plaquette defects.

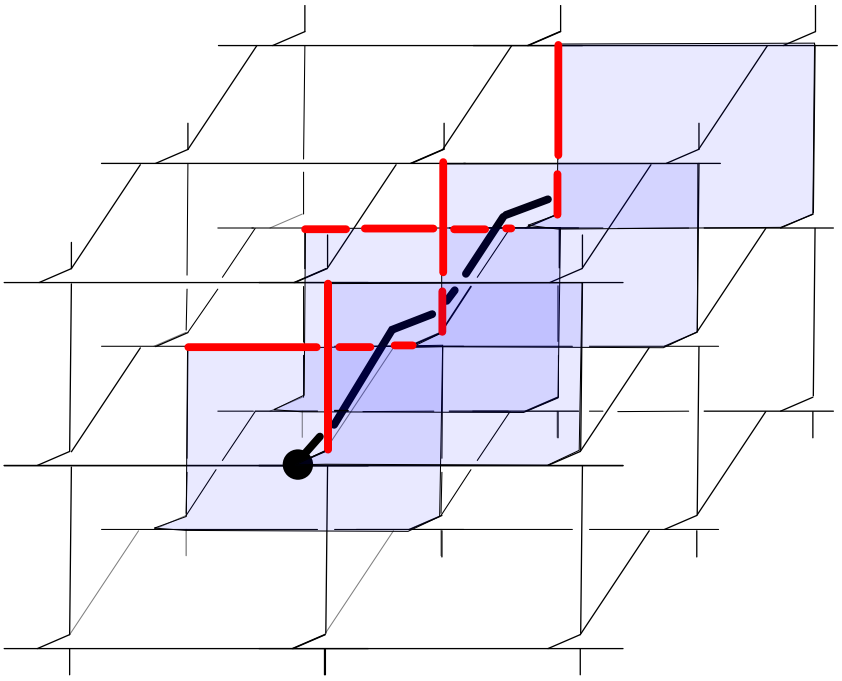


Figure 3.5: The string operator that creates deconfined fermions in the bulk acts with σ^x along the series of edges adjacent to the thick black string. To make this operator commute with the plaquette terms in the Hamiltonian, it must also act with σ^z on an adjoining set of "crossed edges", shown in red. This cancels the possible plaquette defects created by acting with σ^x on the U or O edges of the adjoining plaquettes shaded purple.

The deconfined vertex defects are bosonic in the TC, but fermionic in the FTC. This follows from the form of the operator that creates the deconfined fermionic excitations, which can be deduced using the graphical mnemonic[11] discussed at length in Sec. 2.4.1:

$$W_V^f(\mathcal{C}) = \prod_{j\in\mathcal{C}} \hat{\sigma}_j^x \underbrace{\prod_{\text{crossed edges}} \hat{\sigma}_i^z}_{\hat{\Phi}(\mathcal{C})} . \tag{3.31}$$

The excitations lie at the endpoints of the path $\mathcal{C}$. The first term in $W_V^f(\mathcal{C})$ is the same operator that creates deconfined bosonic excitations in the toric code, by flipping all the edges along the path $\mathcal{C}$. The second term $\hat{\Phi}(\mathcal{C})$ is required to make this operator commute with the FTC plaquette term. One can check that $W_V^f(\mathcal{C})$ commutes with the Hamiltonian everywhere except near its endpoints. However, the additional phases due to $\hat{\Phi}(\mathcal{C})$ also imbue the vertex defects with fermionic statistics, in agreement with the qualitative field theoretic argument in Sec. 3.1.2.2.

[11] That is, draw a string on the lattice, and fuse it into the edges using the graphical rules.

3.3.3 Connection to $k = 1, p = 2$ dyon condensate degrees of freedom

In Sec. 3.1.2.2, we saw that the dyon condensed $k = 1, p = 2$ axion theory had fermionic $(-1, 1)$ deconfined excitations, and $E_i = 1/2$ electric flux defects. These can be identified with the vertex defects, and lines of plaquette defects respectively in the fermionic toric code.

Let us establish a concrete dictionary between the degrees of freedom in the axion theory and those in the Walker-Wang model. First, the $\hat{\sigma}_i^x$ operator in the WW model is associated with $e^{i\hat{A}_i}$ in the $bF + bb$ theory, which is also associated with $e^{i\hat{A}_i}$ in the axion theory. Second, notice that the operator that measures whether or not an edge contains a string $(\hat{\sigma}_i^z)$ is associated with $e^{\frac{i\pi}{2}\epsilon_{ijk}\hat{b}_{jk}}$ in the $bF + bb$ field theory. This field, in turn, is associated with $e^{-i\pi\hat{\mathcal{E}}_i}$ in the axion gauge theory as noted below Eq. (3.12). To the extent that our derivation of the $bF + bb$ theory from the axion theory is valid, we can associate $\hat{\sigma}_i^z$ with $e^{-i\pi\hat{\mathcal{E}}_i}$ in the axion field theory.

With the dictionary established, let us interpret WW model plaquette operator (Eq. (3.30)) in the axion model language. The plaquette operator consists of two parts. The first part measures $\prod_{e\in\partial P}\hat{\sigma}^x$, which in the axion model is just the value of $e^{i\hat{B}_i}$ where $\hat{B}_i = \epsilon_{ijk}\hat{F}_{jk}/2$ is the magnetic flux through the plaquette P. The second part is a phase $\hat{\sigma}^z_{U(P)}\hat{\sigma}^z_{O(P)} = \pm 1$, which, in the axion model can be interpreted as the total $e^{-i\pi\hat{\mathcal{E}}_i}$ flux transverse to the plaquette $\exp\left[-i\pi\left(\mathcal{E}_{U(P)} + \mathcal{E}_{O(P)}\right)\right]$.[12] On net, the fermionic toric code plaquette operator B_p corresponds to the measurement $e^{-i2\pi\hat{E}_i^{\rm PS}}$, where

$$\hat{E}_i^{\rm PS} \equiv \frac{\hat{\mathcal{E}}_{U(P)} + \hat{\mathcal{E}}_{O(P)}}{2} - \frac{\theta}{4\pi^2}B_i \tag{3.32}$$

can be interpreted as a lattice regularised or point-split (PS) version of the electric flux $\hat{E}_i$ in Eq. (3.4). In the present case note that $\frac{\theta}{4\pi^2} = \frac{1}{2\pi}$. The ground state of the fermionic toric code has $B_p = 1$, which corresponds to $\hat{E}_i^{\rm PS} = 0 \mod 1$. The plaquette line defects, on the other hand, are associated with $B_p = -1$, or electric flux $\hat{E}_i^{\rm PS} = \frac{1}{2} \mod 1$ in the axion model. These two statements are in full agreement with the discussion in Sec. 3.1.2.2.

What about the vertex defects? Within the Walker-Wang model, the operator creating these defects is explained in Eq. (3.31). Using the dictionary established above, we can think of a vertex defect creation operator as

$$e^{i\int_C \hat{A}_i} \times e^{-i\pi\sum_{\text{crossed edges}}\hat{\mathcal{E}}_i} \tag{3.33}$$

[12] There are other ways to define this total flux, but the point-splitting convention chosen in Eq. (3.19) demands we adopt this definition.

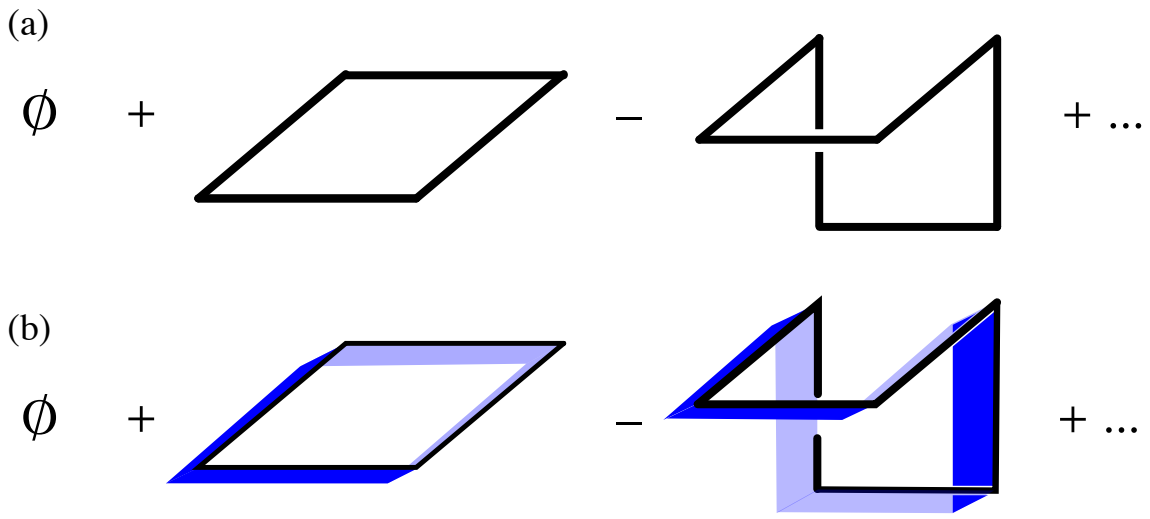


Figure 3.6: This picture shows how the loops in the Walker-Wang model ground state (a) can be made into ribbons (b) by first duplicating each loop, and then dragging the copies in the **n** direction. The -1 phases arise in the ground state precisely when these ribbons are twisted an odd number of times. In the final configuration in b this twist manifests itself in the fact that one end of the ribbon links the other end precisely once, leading to phase -1. The ribbon has two sides, which are light/dark blue.

in the axion gauge theory. The first part of this operator toggles $\hat{\mathcal{E}}_i$ by -1 along the path $\mathcal{C}$. The second part creates two $-\pi$ magnetic flux tubes on plaquettes adjacent to $\mathcal{C}$ (precisely the shaded plaquettes in Fig. 3.5). This can be viewed as creating a point-split flux tube carrying magnetic flux -2π. The tube connecting the point defects has no net electric flux because, averaged over a few plaquettes, the electric field is $E_i^{\mathrm{PS}} = \mathcal{E}_i - \frac{\theta}{4\pi^2} B_i = -1+1 = 0$ modulo 1. In the axion field theory, the neutral monopole $(-1, 1)$ point defect has exactly the same property — it exudes no electric flux, but carries magnetic flux 2π. In the axion field theory, the fermionic statistics of this excitation follow from an argument in [54].

3.3.4 Connection to wave function of bosonic topological insulators

In [47], the authors present the ground state of the bosonic topological insulator as a condensate of vortex "ribbons" in which phase factors (-1) appear when the ribbon is twisted an odd number of times. In this section, we show that this picture of the ground states persists in the FTC, which describes the dyon condensed phase of the same system.

We briefly review the picture of [47]. The point of departure is to view a bosonic insulator in the phase basis $|\{\phi\}\rangle$, using the standard number-phase representation of the Bose operators $\hat{b}_i = \sqrt{\hat{\rho}_i} e^{i\hat{\phi}_i}$. In the strongly insulating limit $\hat{\rho}$ fluctuates little, and so the conjugate phase variables $\hat{\phi}$ are maximally disordered. Indeed, we can think of the insulating state as being a condensate of 2π vortex defects in the phase variables.

The bosonic topological insulator is conveniently understood in this language. The $\mathrm{U}(1) \rtimes \mathbb{Z}_2^T$ BTI is most easily described using two species of bosons, and therefore two species of vortex defects, which always appear in tightly bound pairs to give a U(1) (rather than $\mathrm{U}(1) \times \mathrm{U}(1)$) symmetry. In such a bound state, the two vortex loops can be thought of as defining two edges of a ribbon. Any given ribbon will twist by some multiple of 2π radians over its length. The ground state of the BTI differs from a trivial insulator in that it has a -1 phase whenever the ribbons twist by an odd multiple of 2π radians in total.

To obtain the fermionic toric code, we gauged the BTI considered in [47] and set $g^2 \to \infty$ in the presence of background charge 2 matter, gapping the gauge field to leave the residual $\mathbb{Z}_2$ theory discussed in Sec. 3.1. As discussed above (see Fig. 3.6), we can view the ground state of the fermionic toric code as a superposition of closed loops, weighted by $(-1)^{\text{over-crossings}}$ where over crossings are determined by viewing the lattice from the $(1,1,1)^T$ direction. To make contact with Senthil-Xu's 'ribbon' picture, imagine turning a configuration of loops in the WW ground state into a configuration of ribbons by first duplicating each loop, and then shifting the duplicate loops by $(1,1,1)^T/2$ as in Fig. 3.6(b). If a loop has an odd number of over-crossings, it turns out that the ribbon thus defined has an odd number of twists. Thus, the phase of the configuration in the ground state superposition is $(-1)^{\text{over-crossings}} = (-1)^{\text{self-twists}}$ as shown in Fig. 3.6(a) and (b).

To make the correspondence more concrete, note that the $\sigma^z = -1$ loops in the WW model correspond to the edges on which $b_{ij} = 1 \pmod 2$ in the field theory (Eq. (3.21)). In the ground state (where $\Sigma_{0i} = 0$), however, the sum over b_{0i} imposes the constraint

$$\frac{1}{\pi} F_{ij}(x + \hat{i} + \hat{j}) = b_{ij}(x + \hat{n}) + b_{ij}(x) \mod 2 \,. \tag{3.34}$$

This equation tells us that a single edge with $b_{ij}(x) = 1$ is associated with a pair of $F = \pi \mod 2\pi$ magnetic flux tubes on plaquettes $(x+\hat{i}+\hat{j}, \hat{i}, \hat{j})$ and $(x+\hat{i}+\hat{j}-\hat{n}, \hat{i}, \hat{j})$. Hence the $\sigma^z = -1$ loops in the WW ground state are associated with pairs of π magnetic flux tubes (i.e. pairs of line-like plaquette defects for which $\prod_{e \in \partial P} \hat{\sigma}^x = -1$)

separated by the vector $\hat{n}$. The pair of π flux tubes can be viewed as depicting a point split 2π flux tube. So, the ground state looks like a superposition of 2π flux tubes, bound to a $b_{ij} = 1$ loop. The resulting ribbon-like objects are weighted by the phase $(-1)^{\text{self-twisting}}$, exactly as in the BTI [47]. While the ribbons in [47] are bound states of two vortex loops corresponding to two species of bosons, the WW ribbons are bound states of two π magnetic flux loops, and the $b_{ij} = 1$ loops.

3.4 Deconfined surface anyons at the boundary between confining phases

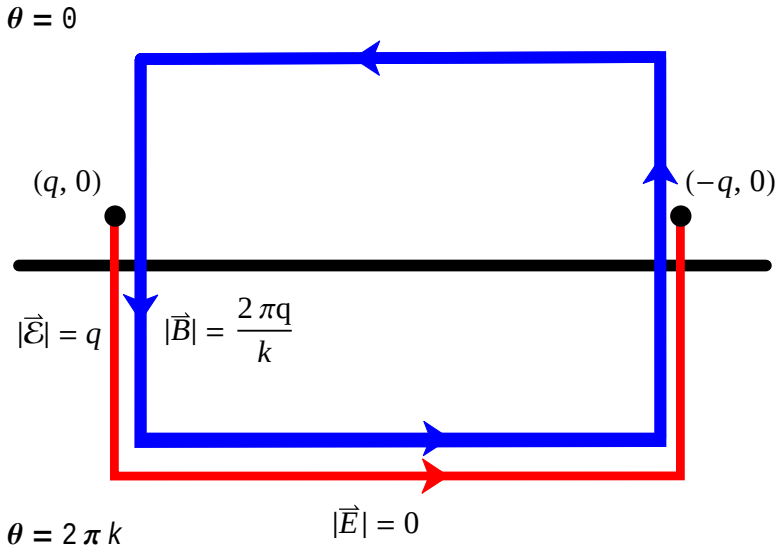


Figure 3.7: This figure shows the interface (black) between the $\theta = 2\pi k$ dyon condensed phase, and the $\theta = 0$ confined phase. The black dots are charge $q = 1, \ldots, p-1$ test charges near the interface. Electric flux $E_i = \mathcal{E}_i - \frac{\theta}{4\pi^2} B_i$ is linearly confined in both phases. As a result, the q charges are dressed with a $2\pi q/k$ magnetic flux tube (blue). The red lines denote $\mathcal{E}_i$ flux, defined below Eq. (3.4).

One of the defining features of the Walker-Wang models that we consider (with the exception of the fermionic toric code) is that they have excitations with anyonic statistics pinned to their surfaces. How do these anyonic excitations arise in the gauge theory? The correspondence that we have established between axion electrodynamics and Walker-Wang Hamiltonians suggests that the Walker-Wang boundary of Sec. 2.3 is equivalent to the interface between the dyon condensed phases at $\theta = 2\pi k, \theta = 0$.

We can support this claim by examining the effective Lagrangian Eq. (3.12) at large g^2

$$\mathcal{L} = \begin{cases} -\frac{i\pi}{k} b \wedge b - ib \wedge F & : \theta = 2\pi k \neq 0 \\ +\frac{g^2}{2} b_{\mu\nu}^2 - ib \wedge F & : \theta = 0 \end{cases}$$

where $b \in \{0, 1, \ldots, p-1\}$ and $F \in \frac{2\pi}{p}\{0, 1, \ldots, p-1\}$. The $bF+bb$ field theory arising for $\theta = 2\pi k \neq 0$ we showed (rigorously in some cases) is the same as a $\mathrm{U}(1)_k$ Walker-Wang model. These models have ground states involving a superposition of loops of all lengths, encoded by b. The second case $\theta = 0$ represents a trivial phase with no (or short) loops (i.e., $b = 0$). Thus it is plausible that a boundary between the $\theta = 2\pi k$ and $\theta = 0$ large g^2 phases is akin to a boundary between a Walker-Wang model and a trivial (no loop) phase. Such a boundary condition is reminiscent of the 'smooth' boundary in Sec. 2.3, for which the Walker-Wang models under consideration admit deconfined surface anyons.

In this section, we argue heuristically for the existence of these deconfined anyons starting from the continuum action Eq. (3.2). A more concrete field theoretic companion calculation appears in [2]. To understand the deconfinement in the continuum setting, it is useful to consider what happens when we bring an integer charge $(q, 0)$ with $q = 1, 2, \ldots, p-1$ near the surface, just outside of the $\theta = 2\pi k$ region (Fig. 3.7). Such an object will source a field line $\mathcal{E} = q$. Outside of the sample, this corresponds to an electric $E = q$ field line which is linearly confined. Inside of the sample, this corresponds to an electric field value of $E = q - \frac{k}{2\pi} B$. Thus, within the sample, the field line need not be confined provided there is a nearby parallel magnetic field line $B = 2\pi q/k$. We do not require that k divides q, so generically this magnetic field line cannot terminate on a monopole. It will form a closed loop. A loop of purely magnetic flux and $\mathcal{E} = 0$ is confined in the $\theta = 2\pi k$ bulk (because $E = \mathcal{E} - \frac{k}{2\pi} B$), but not within the $\theta = 0$ bulk. Thus, a pair of $(q, 0)$ charges are not confined near the surface because the $\mathcal{E}$ field line connecting $(q, 0)$ charges can be screened by a magnetic flux loop as shown in Fig. 3.7.

The statistics of point excitations near the surface follow readily from this flux attachment picture. Surface $(q, 0)$ particles are associated with closed $B = 2\pi q/k$ flux tubes, part of which lie in the $\theta = 2\pi k$ region as shown in Fig. 3.7. The exchange of any two $(q, 0)$ excitations is thus associated with the intersection of two $\frac{2\pi q}{k}$ flux tubes in the $\theta = 2\pi k$ region. However such an intersection of flux tubes is associated with a phase of $\pi q^2/k$, by virtue of the $\frac{ik}{4\pi} F \wedge F$ term. However, there is also a phase

of $-2\pi q^2/k$ due to the Berry phases of the q charges with the $2\pi q/k$ magnetic flux tubes. Thus, the $(q, 0)$ particles behave like anyons with a self-statistic of $e^{-i\pi q^2/k}$ [2].

3.5 Discussion and conclusions

In this chapter, we have argued heuristically that the dyon condensed phases of axion electrodynamics with integer $k = \theta/2\pi$ (and appropriate dynamical matter fields) are captured by topological field theories of the form Eq. (3.14). We then showed, rigorously in many cases, that these topological field theories can be expressed in Hamiltonian form as Walker-Wang models. (We have discussed the specific example $k = 1$ in the main text, but in App. B.1 we show how these arguments apply more generally). We now discuss what conclusions about the phases realised by these lattice Hamiltonians can be drawn from this relation.

Begin by considering the phase diagram of axion electrodynamics for $k = 1$. In the limit that $g^2 \to 0$ (when the U(1) gauge field is weakly fluctuating) and the dynamical charge 2 matter is heavy (so that it cannot condense and break this global U(1)), this field theory describes the electromagnetic response of the bosonic topological insulator. As [46] points out, one of the distinctive features of this phase is that the fundamental electrically neutral object (or 'neutral monopole') of the compact U(1) gauge field is a fermion.

[46] emphasises that the fermionic nature of the neutral monopoles is necessary to cancel a statistical anomaly at the surface, where by Laughlin's argument we find that inserting a flux of 2π creates a fermion. Since these fermionic neutral monopoles must pair to condense, this leads to $\mathbb{Z}_2^{(1)}$ topological order as we take the theory to strong coupling. Hence the fact that the weak-coupling SPT insulator becomes a topologically ordered phase at strong coupling is a symptom of the statistical anomaly.

Though we have focused exclusively on abelian categories, there are also non-abelian categories with a similar surface statistical anomaly in which an appropriate flux insertion produces a "trivial" fermion. The corresponding Walker-Wang models also have bulk $\mathbb{Z}_2^{(1)}$ topological order, and can also potentially be viewed as the strong-coupling limit of weakly gauged symmetry-protected phases. One example is the model based on $\mathrm{SO}(3)_6$ used by [40] to discuss fermionic symmetry-protected phases. (To do so they eliminate the $\mathbb{Z}_2^{(1)}$ topological order by introducing extra fermions into the problem).

Next, we consider the family of models with k even. It is instructive to scrutinise the surface states of these models: for even k our surface states have the same

anyon content as the bosonic Laughlin states at filling fraction $\nu = 1/k$, or as 2D $U(1)_k$ Chern-Simons gauge theory. Hence for even k, in the absence of extra symmetries, our models are neither topologically ordered nor SPT. This suggests that the corresponding Walker-Wang Hamiltonians are adiabatically connected to the trivial confined phase with $\theta = 0$.

The field theory's phase diagram suggests a path whereby this might happen: it is well known that the trivial confined phase with $\theta = 0$ is adiabatically connected to the trivial Higgs phase (in which a charge 1 dynamical matter field has condensed) [31]. In the Higgs phase, where magnetic monopoles are confined, θ can be changed arbitrarily without closing the gap. In particular we can shift θ by 4π to obtain a new version of the trivial Higgs phase, in which our neutral monopole is a bound state of a monopole with two charges. The thermodynamics, however, should be independent of the form of this neutral monopole; hence for $\theta = 4\pi$ (more generally $\theta = 4\pi n$), we expect to be able to adiabatically continue the system from the trivial Higgs phase to the $\theta = 4\pi$ dyon condensed phase. Though (with appropriate boundary conditions) this will certainly close the gap at the surface, it should not require a bulk phase transition. The same line of reasoning suggesting that all models with even k are adiabatically connected to the trivial confined phase suggests that all models with odd k are adiabatically connected to the model with $k = 1$ (i.e., the fermionic toric code).

In summary, we have established that the dyon condensed phases of axion electrodynamics with integer $k = \theta/2\pi$ (and appropriately selected dynamical matter fields) are described by the Walker-Wang topological lattice models. We have argued qualitatively that the spectra of the dyon condensates and the lattice models should be the same; more importantly, we have supported these arguments by showing that the partition function of a related gauge theory on the lattice can be viewed as the path integral of the Walker-Wang Hamiltonian. As well as being pertinent to related work in the high-energy literature [43, 44, 48], this has allowed us to understand the relationship between the lattice models built from "fermionic" quantum Hall states and SPT phases. It also suggests a route to adiabatically connect Hamiltonians constructed from bosonic quantum Hall states to the trivial confined phase.

Chapter 4

Conclusions

We examined the properties of a new set of topological Walker-Wang lattice models; in Chapter 2 we listed their spectra, and criteria for when they exhibit long-range entanglement. Additionally, we examined the $(2+1)$D boundaries of these models, where in certain cases they possessed deconfined chiral anyonic excitations.

We then showed that certain Walker-Wang models can arise in more familiar systems of particles and gauge fields. In particular, in Chapter 3 we argued that the $\mathrm{U}(1)_k$ type Walker-Wang models capture the physics of the dyon condensed phases of axion electrodynamics. In the process, we proved a rigorous correspondence between topological discrete $bF + bb$ theory and certain $\mathrm{U}(1)_k$ Walker-Wang models, which allowed us to make contact with interesting recent work in the high-energy literature [43, 44, 48]. Connecting Walker-Wang models and axion electrodynamics suggests that WW models may well describe the physics of certain condensed matter systems. One can (with varying degrees of plausibility) argue that certain Mott insulating phases with strong spin-orbit coupling permit a description in terms of axion electrodynamics [34]. Thus, we hope that the work performed here gives an insight into what kinds of bulk and boundary phenomena might arise in these systems.

We now return to the question of whether Walker-Wang models realise a new phase of matter and in particular whether their surface states can be realised in purely 2D systems. For this discussion we restrict attention to the $\mathbb{Z}_p$ type confined abelian Walker-Wang models (e.g., 3DSem).

In Chapter 3, we saw that the abelian confined Walker-Wang models are 'twisted' versions of $\mathbb{Z}_p$ gauge theories, with p different kinds of plaquette fluxes, and correspondingly the excitations have a $\mathbb{Z}_p$ Potts-like charge and conservation law. So, in this sense, we can view the surfaces of these Walker-Wang models as $\mathbb{Z}_p$ gauge theories with chiral excitations. In 2D, however, a rigorous and complete classification of discrete topological gauge theories [10] shows that all discrete $\mathbb{Z}_p$ gauge theories

are achiral (or 'doubled'). So, it appears as though within the realm of discrete topological gauge theories, the surfaces of the Walker-Wang models cannot be realised as purely 2D systems. Recently, [57] has suggested a generalisation of the result of [10]: It is believed that no 2D "fixed-point" (i.e., zero correlation length) Hamiltonian has chiral topological order. Thus within the wider sphere of fixed-point Hamiltonians, one can make a strong case that the topological order of the surface of the Walker-Wang models cannot be realised in 2D.

Despite this, one might still argue that the surfaces of Walker-Wang models are unremarkable, given that there exist 2D quantum Hall systems with the same anyon content. However the two kinds of systems exhibit very different physics. First, the fractional quantum Hall effect is traditionally viewed as a theory of U(1) charges coupled to a U(1) Chern-Simons gauge theory. In contrast, in relation to the previous point, the Walker-Wang surfaces host $\mathbb{Z}_p$ Potts-like charges.

Second, while Walker-Wang models are fixed-point models, the Hall states necessarily have a nonzero intrinsic scale (the magnetic length); it seems that chiral topological order in 2D is always accompanied by a nonzero correlation length. Furthermore, the fractional Hall state has topologically protected gapless boundary modes, meaning that when the 2D system has a boundary, the correlation length at the boundary must be infinite. Third, and perhaps most strikingly, chiral 2D topologically ordered states seemingly always exhibit a universal antisymmetric viscosity (or "Hall viscosity" [58]) and response to temperature gradients [59], neither of which are present on the surface of the Walker-Wang models.

We now make a conjecture as to why this is the case. 2D states with chiral topological order are thought to be governed by chiral Chern-Simons theory in $(2+1)$D. This field theory, it turns out, despite being naively topological, requires extra structure like a metric for its safe regularisation. For instance in [60], the final effective Chern-Simons Lagrangian involves metric dependent Chern-Simons gravity counterterms.

This field theoretic perspective suggests that physical systems realising, say, U(1) Chern-Simons topological order have a metric dependence governed by Chern-Simons gravity. This statement is reinforced by noting that a Chern-Simons gravity type response theory accurately captures the universal Hall viscosity, and thermal conductivity of the abelian FQH states [61]. In contrast, the 3D Walker-Wang models are manifestly regularised, and realise all the anyons in the Chern-Simons theory without requiring the introduction of a metric. Correspondingly, they do not exhibit the

universal Hall viscosity or thermal transport, which are associated with responses to changes in the metric (governed by Chern-Simons gravity).

On a related note, recent work [43, 44, 48] has shown that the dyon condensed regimes of compact U(1) have a precise mathematical characterisation as non-trivial elements (cocycles) of a '2-group cohomology' $H^4(B^2\mathbb{Z}_p, \mathrm{U}(1))$, where p coincides with the charge of the background boson in Chapter 3. Using results from the present work, we can argue that the confined Walker-Wang models provide realisations of precisely these non-trivial cocycles. That the confined Walker-Wang models appear in such a classification scheme is highly suggestive that they realise a new phase of matter. However a concrete physical characterisation of these phases – in particular the conditions under which they are robust – is still lacking.

It is not at all clear that any of the string-net models considered here are realised in known real materials or whether they can practicably be simulated in optical lattices, and much work will need to be done to ascertain the answer to these questions. There are still also open questions as to under what circumstances different string-net models are adiabatically connected to one another. If not, what is the nature of the phase transitions between them? We have made some progress on this question in separate publications in both 2D [62], and 3D [3], but the question is nowhere near settled.

Appendix A

Appendices for Chapter 2

A.1 MTC's are non-degenerate on manifolds without boundary

In this section we show that all confined Walker-Wang models have a single ground state on the 3-torus, although this method of proof generalises to other simple manifolds without boundary. This can also be viewed as a proof that there are no deconfined excitations in the three dimensional bulk. In Sec. 2.4.1 we reasoned that all confined Walker-Wang models are based on modular tensor categories. One of the key features of modular tensor categories is the 'Flux killing property', described in Fig. 2.14(c): A loop of the string-type ω_0 (used to define plaquette operators) projects anything it encloses onto zero flux. In the following proof we will make heavy use of this fact, as well as the handle-slide property Fig. 2.14(a) of ω_0 strings (which holds in all premodular categories).

This proof is structured as follows. In order to show there is just one ground state, we need only show that $\mathcal{P} \mid \psi\rangle \propto \mathcal{P} \mid 0\rangle$ holds for any string-net configuration, where $\mid 0\rangle$ is the configuration with no edges coloured in (meaning all edge bonds have label $i = 0$) and $\mathcal{P}$ is the ground state projector. We do this in three parts. First, we show that

$$\mathcal{P} \mid \psi\rangle = \sum_i a_i \mathcal{P} \mid \psi_{xy}\rangle_i \,, \tag{A.1}$$

where $\mid \psi_{xy}\rangle_i$ are configurations with edges coloured only in the xy plane. We will then apply the same procedure to show that, for any of the configurations lying in the xy plane,

$$\mathcal{P} \mid \psi_{xy}\rangle = \sum_i b_i \mathcal{P} \mid \psi_{y\text{-axis}}\rangle_i \tag{A.2}$$

where $\mid \psi_{y\text{-axis}}\rangle$ are configurations with edges coloured only along the y-axis. Applying the procedure one last time we will show that, for any of the configurations along the y-direction

$$\mathcal{P} \mid \text{y-axis}\rangle = c\mathcal{P} \mid 0\rangle \,. \tag{A.3}$$

Hence, feeding this all into (A.1), we get

$$\mathcal{P} \mid \psi\rangle \propto \mathcal{P} \mid 0\rangle \tag{A.4}$$

for all $\mid \psi\rangle$, as required. Let us first prove Eq. (A.1). Consider the sequence of diagrams Fig. A.1, which show a section of the xy plane on the 3-torus. Fig. A.1(a) represents some string-net configuration acted on by the ground state projector $\mathcal{P} \mid \psi\rangle$. We remind the reader that the ground state projector $\mathcal{P} = \prod_v \mathcal{P}_v \prod_p \mathcal{P}_p$ is just a product of all vertex and plaquette projectors, and that a plaquette projector $\mathcal{P}_p$ can be represented by drawing a ω_0 string in plaquette p. In (b) we act on this state with ω_0 loops on the vertical edges sticking up and out of the xy plane. We call the operator $\mathcal{K}_z$, and so we have formed a state $\mathcal{K}_z \mid \psi\rangle$. We then act with a set S_1 of plaquette projectors just above the xy plane, each lying in a xz plane, to form the state $\prod_{p\in S_1} \mathcal{P}_p \mathcal{K}_z \mathcal{P} \mid \psi\rangle$ in (c). Using the plaquette projectors in the original expression $\mathcal{P} \mid \psi\rangle$, we can handle-slide the plaquette projectors in $\prod_{p\in S_1} \mathcal{P}_p$ to form the figure in (d), which is another graphical representation of $\prod_{p\in S_1} \mathcal{P}_p \mathcal{K}_z \mathcal{P} \mid \psi\rangle$. We can then use the flux killing property of ω_0 strings (in MTC's) to show that this state is diagrammatically represented by (e).

We are now near the end of the proof. We act on (e) with a set S_2 of plaquette projectors just above the xy plane to form the state $\prod_{p\in S_1\cup S_2} \mathcal{P}_p \mathcal{K}_z \mid \psi\rangle$ shown in (f); we colour the new plaquette strings red for clarity. We can again use the handle slide properties of the plaquette projectors in $\mathcal{P} \mid \psi\rangle$ to manipulate the red strings into the equivalent form shown in (g). Using the flux killing properties of the red strings, we can close up the black plaquette strings to form (h). But (h) simply represents the state $\prod_{p\in xy} \mathcal{P}_p \mathcal{P} \mid \psi\rangle$ which is equal to $\mathcal{P} \mid \psi\rangle$. Hence, we have proved the following equation:

$$\prod_{p\in S_1\cup S_2} \mathcal{P}_p \mathcal{K}_z \mathcal{P} \mid \psi\rangle = \mathcal{P} \mid \psi\rangle \tag{A.5}$$

Acting on this equation with $\mathcal{P}$, we get the following equation:

$$\mathcal{P}\mathcal{K}_z \mathcal{P} \mid \psi\rangle = \mathcal{P} \mid \psi\rangle \,. \tag{A.6}$$

This equation is the main result of this section because the state $\mathcal{P}\mathcal{K}_z\mathcal{P} \mid \psi\rangle$ has an interesting property: The operator $\mathcal{K}_z$ kills all the flux on the vertical legs just above the xy plane. This implies that the string-net configurations in $\mathcal{K}_z\mathcal{P} \mid \psi\rangle$ are contractible, at least around the z-cycle of the torus. So the string-net configurations in $\mathcal{K}_z\mathcal{P} \mid \psi\rangle$ can be deformed to lie in the xy plane. Hence

$$\mathcal{P}\mathcal{K}_z\mathcal{P} \mid \psi\rangle = \sum_i a_i \mathcal{P} \mid \psi_{xy}\rangle_i \,, \tag{A.7}$$

and using Eq. (A.6) we get Eq. (A.1). We now repeat the process. Define an operator $\mathcal{K}_x$ by putting ω_0 loops around edges leaving the yz plane and note the result Eq. (A.6) also holds for $\mathcal{K}_x$. As the operator $\mathcal{K}_x$ kills all the flux on the legs just to the right of the yz plane, the string-net configurations in $\mathcal{K}_x\mathcal{P} \mid \psi_{xy}\rangle$ are contractible around the x-cycle of the torus (as well as the z-cycle). So the string-net configurations in $\mathcal{K}_x\mathcal{P} \mid \psi_{xy}\rangle$ can be deformed to lie along the y-axis. Hence

$$\mathcal{P}\mathcal{K}_x\mathcal{P} \mid \psi_{xy}\rangle = \sum_i b_i \mathcal{P} \mid \psi_{y\text{-axis}}\rangle_i \,, \tag{A.8}$$

and using Eq. (A.6) we get the result Eq. (A.2). Now to the final stage of the argument. Define an operator $\mathcal{K}_y$ by putting ω_0 loops around edges leaving the zx plane and note the result Eq. (A.6) also holds for $\mathcal{K}_y$. As the operator $\mathcal{K}_y$ kills all the flux on the legs leaving the zx plane, the string-net configurations in $\mathcal{K}_y\mathcal{P} \mid y\text{-axis}\rangle$ are contractible around the y-cycle of the torus (as well as the z-cycle and x-cycle). So the string-net configurations in $\mathcal{K}_x\mathcal{P} \mid \psi_{y\text{-axis}}\rangle$ can be deformed to $\mid 0\rangle$. Hence

$$\mathcal{P}\mathcal{K}_x\mathcal{P} \mid \psi_{y\text{-axis}}\rangle = c\mathcal{P} \mid 0\rangle \,, \tag{A.9}$$

and using Eq. (A.6) we get the result Eq. (A.3). The statement Eq. (A.4) follows from this. Thus we have shown that the flux killing property of MTC's implies that Walker-Wang models based on MTC's are non-degenerate on the 3-torus.

A.2 All string operators are confined in MTC's

In this section we prove that for all MTC's, any vertex types string operators (obeying mild constraints) produce plaquette violations along their length. Indeed if there were to be deconfined string operators in MTC's, they would have multiple ground states on $\mathbb{T}^3$ contradicting the result of the previous section. This result supplements the discussion in the text, where we considered a special type of string operator ($\hat{W}_V(\mathcal{C})$) and showed that it fails to commute with the plaquettes along its length.

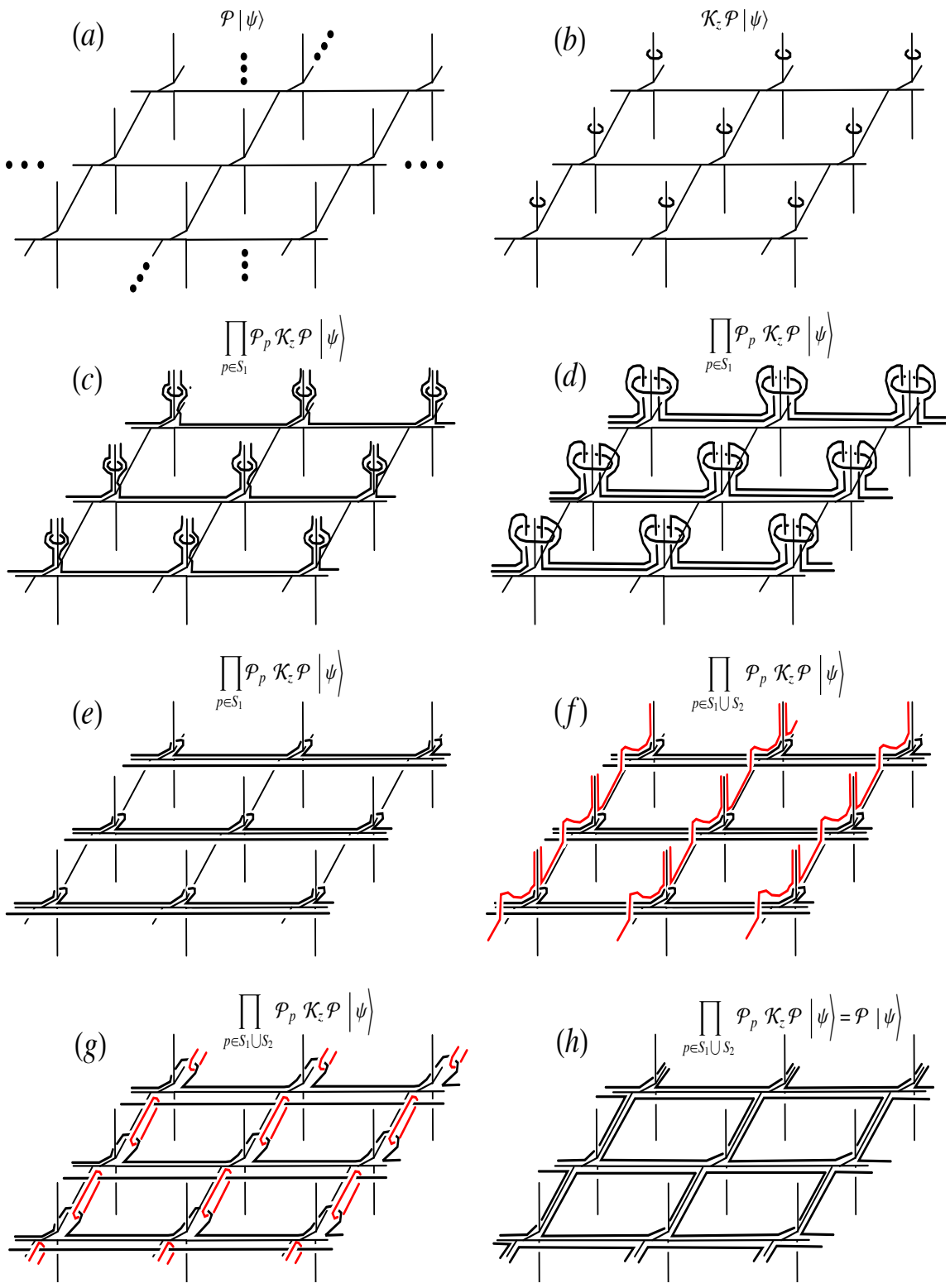


Figure A.1: This figure shows the sequence of steps used in proving that Walker-Wang models based on MTC's are non-degenerate on the 3-torus.

Suppose we construct a string operator $\hat{\mathcal{V}}(\mathcal{C})$ with the following qualities. It can change the colour of edges along a path $\mathcal{C}$, and assign a configuration dependent phase to edges touching the path $\mathcal{C}$. Furthermore, we assume that if the edges on $\mathcal{C}$ have label $i = 0$, $\hat{\mathcal{V}}(\mathcal{C})$ will flip the edges to some superposition of states, some of which have all the edges on the path $\mathcal{C}$ in a state $i \neq 0$. In this section we will show that such an operator necessarily fails to commute with plaquettes along its length.

Suppose that $\mathcal{C}$ pierces the xy plane once. Take a sufficiently large set S of plaquettes in the xy plane with the condition that $\mathcal{C}$ pierces the set, but the plaquettes near the boundary of S are not acted on by $\hat{\mathcal{V}}(\mathcal{C})$ (see Fig. A.2). We will show that, with the above conditions, $\hat{\mathcal{V}}(\mathcal{C})$ will fail to commute with some plaquettes in S. This shows that the defects created by $\hat{\mathcal{V}}(\mathcal{C})$ are necessarily linearly confined.

With these above assumptions about $\hat{\mathcal{V}}(\mathcal{C})$, we can say that upon acting on the empty ket $\mid 0\rangle$ (all edges carry label $i = 0$), the string operator flips all the edges along $\mathcal{C}$ to some superposition of labels $s = \sum_i s_i \hat{i} \neq 0$. Without loss of generality (by subtracting a multiple of the identity operator from $\hat{\mathcal{V}}(\mathcal{C})$) we can assume that $s_0 = 0$. This implies that

$$\hat{W}_V^{\omega_0}(\partial S) \prod_{p \in S} \mathcal{P}_p \hat{\mathcal{V}}(\mathcal{C}) \mid 0\rangle = 0 \tag{A.10}$$

where $\hat{W}_V^{\omega_0}(\partial S)$ is a string operator with the special handle-slide property, and ∂S is some path on the boundary of the set of plaquettes in the xy plane (see Fig. A.2). This equation follows simply from the fact we can handle-slide the perimeter string ∂S inwards so that it encloses the edges on path $\mathcal{C}$ which carry label s. As we are in a MTC based model and $s_0 = 0$, we can use the flux killing property of the Fig. 2.14(b) to get zero in Eq. (A.10).

If we assume that $\prod_{p \in S} \mathcal{P}_p$ and $\hat{\mathcal{V}}(\mathcal{C})$ commute then we are led to a contradiction. Continuing from the previous equation:

$$\begin{aligned} 0 &= \hat{W}_V^{\omega_0}(\partial S) \prod_{p \in S} \mathcal{P}_p \hat{\mathcal{V}}(\mathcal{C}) \mid 0\rangle \\ \text{“} &= \text{”} \hat{W}_V^{\omega_0}(\partial S) \hat{\mathcal{V}}(\mathcal{C}) \prod_{p \in S} \mathcal{P}_p \mid 0\rangle \\ &= \hat{\mathcal{V}}(\mathcal{C}) \hat{W}_V^{\omega_0}(\partial S) \prod_{p \in S} \mathcal{P}_p \mid 0\rangle \end{aligned} \tag{A.11}$$

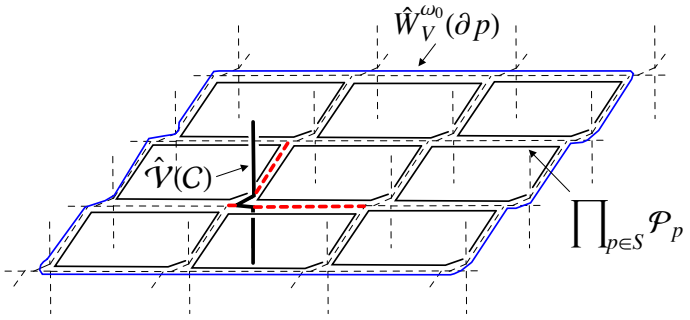


Figure A.2: This figure represents a string operator $\mathcal{V}(\mathcal{C})$ piercing the xy plane. The black loops are the plaquette operators in a set S, pierced by the string operator, while $\hat{W}_V^{\omega_0}(\partial p)$ (blue line) is another string operator (with label ω_0) which encircles the perimeter of the set S). In the text we show that $\hat{\mathcal{V}}(\mathcal{C})$ fails to commute with some of the plaquettes in S, with fairly mild assumption on the form of $\hat{\mathcal{V}}(\mathcal{C})$.

To get to the second line, we assumed that the plaquettes commute with $\hat{\mathcal{V}}(\mathcal{C})$. In the third line, we used the fact that $\left[\hat{\mathcal{V}}(\mathcal{C}), \hat{W}_V^{\omega_0}(\partial S)\right] = 0$ because they do not act on the same edges. Now, $\hat{W}_V^{\omega_0}(\partial S)\prod_{p\in S}\mathcal{P}_p \mid 0\rangle = \mathcal{P}_p \mid 0\rangle$ because we can handle-slide the string over the plaquette operators to get a ω_0 loop enclosing no flux. Therefore,

$$\begin{aligned} 0 &= \hat{\mathcal{V}}(\mathcal{C})\prod_{p\in S}\mathcal{P}_p \mid 0\rangle \\ &= \prod_{p\in S}\mathcal{P}_p\hat{\mathcal{V}}(\mathcal{C}) \mid 0\rangle \end{aligned} \tag{A.12}$$

But this state is just a cluster of plaquette projectors acting on a ket with some edges in superposition s. It can be shown that such a state is not zero by expanding out the plaquette projectors in terms of plaquette string operators $W_V^j(\partial p)$. Consider a string configuration where all edges have label 0 except for those on $\mathcal{C}$ (which are in superposition s). This configuration can be shown to occur once in the expansion of $\prod_{p\in S}\mathcal{P}_p\hat{\mathcal{V}}(\mathcal{C}) \mid 0\rangle$, and with a non-zero coefficient. Hence the expression $\prod_{p\in S}\mathcal{P}_p\hat{\mathcal{V}}(\mathcal{C}) \mid 0\rangle$ cannot be zero. Thus, the assumption that $\prod_{p\in S}\mathcal{P}_p$ and $\hat{\mathcal{V}}(\mathcal{C})$ commute leads to a contradiction.

A.3 Explicit forms for operators in the 2D DSem model

In our main treatment of the DSem model, we defined the plaquette operators only in the absence of vertex defects. Furthermore, we never explicitly showed the form

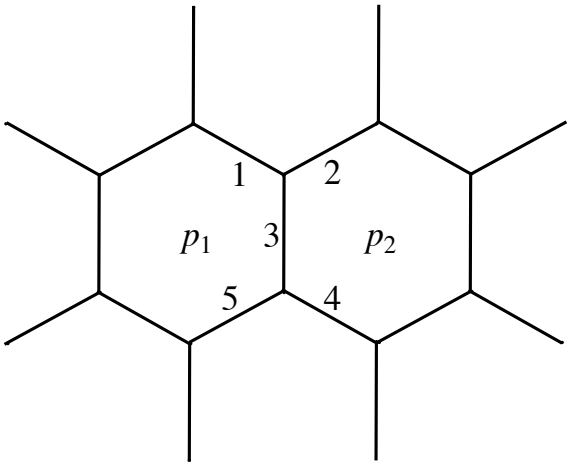


Figure A.3: The figure shows an adjacent pair of plaquettes (p_1 and p_2), used to show that adjacent plaquette operators in the DSem model (as defined in Eq. (1.4)) do not commute if vertex defects are present.

of string operators near their end-points. In this appendix, we address some of these issues. In the main text we defined the plaquette operators as

$$B_p = (\prod_{i\in\partial p} \sigma_i^x) \prod_{j\in s(p)} i^{(1-\sigma_j^z)/2} . \tag{A.13}$$

The difficulty with Eq. (A.13) is that as operators, B_{p_1} and B_{p_2} do not commute when acting on neighbouring plaquettes. Specifically, on the 5 edges on which both operators act (see Fig. A.3) we have

$$\begin{aligned} B_{p_1}B_{p_2} &= \left(\sigma_1^x\sigma_3^x\sigma_5^x e^{i\frac{\pi}{4}(1-\sigma_2^z)}e^{i\frac{\pi}{4}(1-\sigma_4^z)}\right) \\ &\quad \left(\sigma_2^x\sigma_3^x\sigma_4^x e^{i\frac{\pi}{4}(1-\sigma_1^z)}e^{i\frac{\pi}{4}(1-\sigma_5^z)}\right) \\ &= -\sigma_1^x\sigma_2^x\sigma_4^x\sigma_5^x e^{i\theta_{1245}} \\ B_{p_2}B_{p_1} &= -\sigma_1^x\sigma_2^x\sigma_4^x\sigma_5^x e^{-i\theta_{1245}} \end{aligned} \tag{A.14}$$

or

$$\frac{1}{2}[B_{p_1}, B_{p_2}] = -i\sigma_1^x\sigma_2^x\sigma_4^x\sigma_5^x \sin\theta_{1245} \tag{A.15}$$

where

$$\theta_{1245} = \frac{\pi}{4}(\sigma_2^z + \sigma_4^z - \sigma_1^z - \sigma_5^z) \tag{A.16}$$

In the ground state, where

$$B_v = \prod_{i\in\partial V} \sigma_i^z = 1 \quad , \tag{A.17}$$

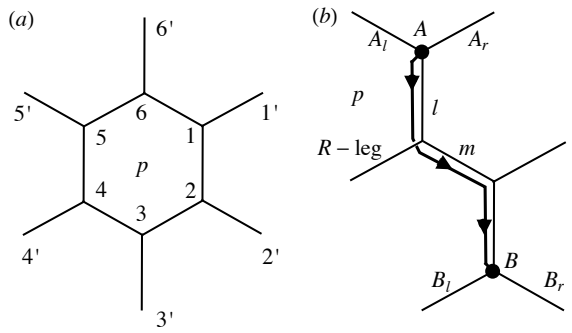


Figure A.4: (a) Shows a labelled plaquette, used to define the complete plaquette operator. (b) Shows a graphical representation of the string operator defined in the text.

θ_{1245} is a multiple of π, and the two products are equal. Thus the plaquette operators (A.13) commute only when acting on states without vertex violations. In states with vertex violations, θ_{1245} is an even or odd multiple of $\pi/2$, depending on whether there is an even or odd number of vertex violations on the two vertices (123), (345).

We can amend the definition of B_p such that the adjacent plaquettes commute in the presence of vertex excitations. For the following definition of B_p it is more convenient to label the vertices of p rather than edges (Fig. A.4(a)), and denote edges by the pair of vertices connecting them. Edges are now labelled by the pair of vertices they connect:

$$
\begin{aligned}
B_p = & \prod_{j=1}^{6} \sigma^x_{j\,j+1} (-1)^{n_{j-1\,j}(1-n_{j\,j+1})} \\
& i^{-(1-Q_1)n_{11'}\Lambda_1} i^{(1-Q_2)n_{22'}\Lambda_2} \\
& i^{(1-Q_3)(1-n_{33'})(n_{23}-n_{34})} i^{-(1-Q_4)n_{44'}\Lambda_4} \\
& i^{(1-Q_5)n_{55'}\Lambda_5} i^{(1-Q_6)n_{66'}(n_{56}-n_{61})}
\end{aligned}
\tag{A.18}
$$

We have defined $Q_v = (I - B_v)/2$, and $\Lambda_v = \sum_{e \in s(v)} n_e$ where e runs over the edges connected to vertex v e.g. $\Lambda_1 = n_{61} + n_{11'} + n_{12}$. This plaquette term represents a rather complicated twelve spin interaction term, although we remind the reader that this reduces to the somewhat simpler form (the first line of Eq. (A.18)) in the absence of vertex defects.

A.3.1 String operators, and their endpoints.

In this section we present a formalism for introducing pairs of vertex defects into the DSem model. We will write down the form of an open vertex-type string operator,

near and away from its endpoints. We use the convention that positive (negative) chirality particles are associated with an over (under) crossing type string. Positive chirality particles can be interpreted as a bound state of a negative chirality particle and a plaquette defect. For Fig. A.4(b), we make the negative chirality string operator take the following form if acting on a state without vertex violations:

$$\prod_{i\in\mathcal{C}}\sigma_i^x \prod_{\langle jk\rangle\in\mathcal{C}}(-1)^{n_j(1-n_k)} \prod_{\langle \mathbf{lm}\rangle \text{ at R vertex}} i^{n_m-n_l}\phi_A\phi_B\,. \tag{A.19}$$

Here the ϕ_A, ϕ_B factors are associated with the precise state of the string endpoints. The phases are defined $\phi_A = i^{(1-n_{A_r})n_{A_l}}$ while $\phi_B = (-i)^{(1-n_{B_r})n_{B_l}}$, where A_l, A_r, B_l, B_r are the edges marked in Fig. A.4(b). The reader should be warned that the exact forms of these phases will depend on which direction the string approaches the vertex. To produce a defect of opposite chirality, we conjugate the operator, except the ϕ_A, ϕ_B parts.

A.4 Topological entanglement entropy in 3DSem

Here we show that unlike its 2D counterpart, the 3D semion model has no topological entanglement entropy. As described in Ref. [63], there are two sensible prescriptions for defining topological entanglement entropy in 3D. We will use one of these for our calculation, but the result is independent of the choice of prescription. Both prescriptions operate on the same principle, generalising the approach of Levin and Wen[8] for 2D systems: we add together the entanglement entropies of several possible partitions of a system into subsystems A and B, with coefficients such that the net boundary and corner terms all cancel. Fig. A.5 shows the combination of four partitions that we will use. We will always cut the two subsystems along the middle of a set of edges, so that the two subsystems must share a set of edge labels along the boundary. The topological component of the entanglement entropy is then given by

$$S_{\text{Top}} = -\left(S^{(1)} - S^{(2)} - S^{(3)} + S^{(4)}\right)\,, \tag{A.20}$$

where $S^{(i)}$ denotes the entanglement entropy associated with region $i = 1, 2, 3, 4$ in Fig. A.5. It is useful to briefly recall the source of the topological entanglement entropy in the toric code. The toric code ground state is a superposition of all configurations of closed loops, with a relative amplitude of 1. Thus, for any partition of the system into two subsystems A and B, we may write

$$|\Psi_0\rangle = \sum_{i_c} \alpha_{i_c} |\Psi_A^{(i_c)}\rangle |\Psi_B^{(i_c)}\rangle \tag{A.21}$$

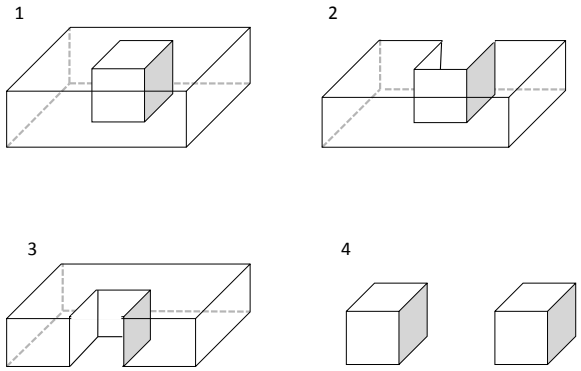


Figure A.5: The combination of partitions used to calculate the entanglement entropy. The figure shows the boundary of the regions A and B.

where i_c denotes a particular choice of edge labels on the boundary between A and B, for which the total number of occupied edges crossing the boundary is even. $|\Psi_A^{(i_c)}\rangle$ and $|\Psi_B^{(i_c)}\rangle$ are themselves superpositions of different loop configurations, agreeing with the configuration i_c of spins on the edge. $|\Psi_0\rangle$ factorises according to Eq. (A.21) because the relative coefficient of all elements in the superposition is always 1.

Because configurations in which the edge labels are different are orthogonal, it is easy to compute the reduced density matrix:

$$\begin{aligned}\rho_A &= \mathrm{Tr}_B \sum_{i_c} |\alpha_{i_c}|^2 |\Psi_A^{(i_c)}\rangle |\Psi_B^{(i_c)}\rangle \langle \Psi_A^{(i_c)}| \langle \Psi_B^{(i_c)}| \\ &= \sum_{i_c} N_B(i_c) |\alpha_{i_c}|^2 |\Psi_A^{(i_c)}\rangle \langle \Psi_A^{(i_c)}|\end{aligned}$$

where $N_B(i_c)$ is the number of configurations in B with boundary conditions i_c. Since $\langle \Psi_A^{(i'_c)} | \Psi_A^{(i_c)} \rangle \propto \delta_{cc'}$, ρ_A is diagonal, and we may read off the entanglement entropy:

$$S_{AB} = \sum_{i_c} N_B(i_c) N_A(i_c) |\alpha_{i_c}|^2 \log \left[N_B(i_c) N_A(i_c) |\alpha_{i_c}|^2 \right] \tag{A.22}$$

subject to

$$\sum_{i_c} N_B(i_c) N_A(i_c) |\alpha_{i_c}|^2 = 1 \tag{A.23}$$

In practise $N_A(i_c), N_B(i_c)$ will be independent of the particular boundary configuration, as will $|\alpha_{i_c}|^2$, so that $N_A(i_c) N_B(i_c) |\alpha_{i_c}|^2 = 1/\mathcal{N}_i$, where $\mathcal{N}_i$ is the number of possible boundary conditions. In a loop gas, if the total number of edges on the boundary between A and B is n_i, then

$$\mathcal{N}_i = 2^{n_i - N_A^{(0)}} \tag{A.24}$$

where $N_A^{(0)}$ is the number of connected components of the boundary of region A. The entanglement entropy is thus :

$$S = \sum_{i=1}^{\mathcal{N}_i} \frac{1}{\mathcal{N}_i} \log \mathcal{N}_i = (n_i - N_A^{(0)}) \log 2 \tag{A.25}$$

The topological entanglement entropy is given by the combination of subdivisions shown in Fig. A.5. In the first three, A consists of a single component and $N_A^{(0)} = 1$; in the last term $N_A^{(0)} = 2$. Since the regions are chosen such that $n_i^{(1)} - n_i^{(2)} - n_i^{(3)} + n_i^{(4)} = 0$, we obtain:

$$\begin{aligned} S_{\text{Top}} &= -\Big[(n_i^{(1)} - 1) - (n_i^{(2)} - 1) \\ &- (n_i^{(3)} - 1) + (n_i^{(4)} - 2)\Big] \log 2 = \log 2 \end{aligned}$$

For the doubled semion model, if A is simply connected then we may use exactly the same reasoning as for the toric code to calculate the entanglement entropy (whether or not A has multiple boundary components). That is, in this case the ground state wave function can be decomposed according to Eq. (A.21), with $|\Psi_A^{(i_c)}\rangle$ a superposition of all loop configurations in A with the boundary spin configuration i_c, and similarly for $|\Psi_B^{(i_c)}\rangle$. Explicitly, when A is simply connected every loop configuration in A with a fixed boundary i_c can be obtained from every other such configuration by acting with some number of plaquette projectors on plaquettes that are entirely inside A. Unlike in the toric code, there are non-trivial relative phases between these different loop configurations; however, these phases are entirely dictated by the action of the plaquette projectors within A, and are independent of the loop configuration in B, such that the wave function still factorises. The rest of the calculation is identical to that for the toric code; hence if A is simply connected, the entropy is again given by Eq. (A.25).

If A is not simply connected, in general the factorisation (A.21) fails because the doubled semion ground state contains phases that are sensitive to the linking number of loops in A with loops in B. The case of interest is where A is topologically a doughnut. Let us separate the wave function $|\Psi_A^{(i_c)}\rangle$ according to:

$$|\Psi_A^{(i_c)}\rangle = \frac{1}{\sqrt{2}} \left[|\Psi_A^{(i_c)}\rangle_{\text{o}} + |\Psi_A^{(i_c)}\rangle_{\text{e}} \right] \tag{A.26}$$

Here e and o refer to whether the total number of down spins measured along a slice through the doughnut is even or odd. $|\Psi_A^{(i_c)}\rangle_{\text{e}}$ (and similarly $|\Psi_A^{(i_c)}\rangle_{\text{o}}$) is a superposition of many different loop configurations with different relative phases, which are related

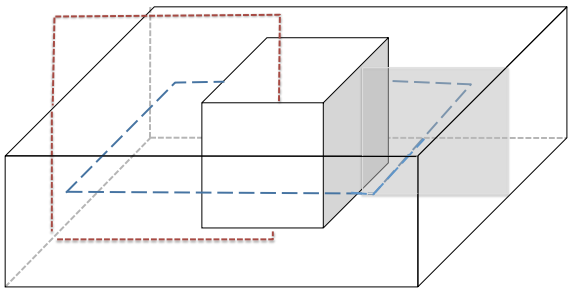


Figure A.6: The scenario if A is not simply connected. If the total number of down spins crossing the cut through the doughnut is odd, then there is a loop that is not contractible within region A. Similarly, if the number of down spins through the centre of the doughnut is odd, then there is a loop that is not contractible within region B. When both of these loops are present, the wave-function has an extra phase -1 due to their linking.

by the action of some number of plaquette projectors acting entirely inside A. To get from a configuration in the even set to one in the odd set, however, one must act with plaquette projectors in region B as well. Thus $|\Psi_A^{(i_c)}\rangle_{\rm o}$ and $|\Psi_A^{(i_c)}\rangle_{\rm e}$ need not appear in the ground state with the same phases, for a given loop configuration in B.

To see the implications of this, let us separate the loop configurations in region B according to whether the number of down spins through the hole in the middle of the doughnut is even or odd (i.e., according to whether or not there is a loop in B that is not contractible within B):

$$|\Psi_B^{(i_c)}\rangle = \frac{1}{\sqrt{2}}\left[|\Psi_B^{(i_c)}\rangle_{\rm o} + |\Psi_B^{(i_c)}\rangle_{\rm e}\right] \tag{A.27}$$

The ground state of 3DSem is given by

$$\begin{aligned} |\Psi_0\rangle &= \sum_{i_c} \frac{\alpha_{i_c}}{2}\Big[|\Psi_A^{(i_c)}\rangle_{\rm e}|\Psi_B^{(i_c)}\rangle_{\rm e} + |\Psi_A^{(i_c)}\rangle_{\rm e}|\Psi_B^{(i_c)}\rangle_{\rm o} \\ &+ |\Psi_A^{(i_c)}\rangle_{\rm o}|\Psi_B^{(i_c)}\rangle_{\rm e} - |\Psi_A^{(i_c)}\rangle_{\rm o}|\Psi_B^{(i_c)}\rangle_{\rm o}\Big] \end{aligned} \tag{A.28}$$

The extra $-$ sign in front of the last term (in addition to any relative phases present in the definitions of $|\Psi_A^{(i_c)}\rangle_{\rm e,o}, |\Psi_B^{(i_c)}\rangle_{\rm e,o}$) arises because when both odd components are taken, the non-contractible loops in A and B are linked, which produces an extra $-$ sign in the wave function.

Because of this extra sign, Eq. (A.28) cannot be expressed in the form Eq. (A.21); rather, we have:

$$\begin{aligned} |\Psi_0\rangle &= \sum_{i_c} \frac{\alpha_{i_c}}{2}\Big\{\left(|\Psi_A^{(i_c)}\rangle_{\rm e} + |\Psi_A^{(i_c)}\rangle_{\rm o}\right)|\Psi_B^{(i_c)}\rangle_{\rm e} \\ &+ \left(|\Psi_A^{(i_c)}\rangle_{\rm e} - |\Psi_A^{(i_c)}\rangle_{\rm o}\right)|\Psi_B^{(i_c)}\rangle_{\rm o}\Big\} \end{aligned} \tag{A.29}$$

so that

$$\begin{aligned}\rho_A &= \sum_{i_c} \frac{|\alpha_{i_c}|^2}{4} N_B(i_c) \\ &\Big\{\Big(|\Psi_A^{(i_c)}\rangle_{\rm e} + |\Psi_A^{(i_c)}\rangle_{\rm o}\Big)\Big(\langle\Psi_A^{(i_c)}|_{\rm e} + \langle\Psi_A^{(i_c)}|_{\rm o}\Big) \\ &+ \Big(|\Psi_A^{(i_c)}\rangle_{\rm e} - |\Psi_A^{(i_c)}\rangle_{\rm o}\Big)\Big(\langle\Psi_A^{(i_c)}|_{\rm e} - \langle\Psi_A^{(i_c)}|_{\rm o}\Big)\Big\}\end{aligned} \tag{A.30}$$

Here we have used the fact that the number of loop configurations in the even and odd sectors of $|\Psi_B^{(i_c)}\rangle$ are equal. As this also holds for $|\Psi_A^{(i_c)}\rangle$, we have:

$$\Big(\langle\Psi_A^{(i_c)}|_{\rm e} + \langle\Psi_A^{(i_c)}|_{\rm o}\Big)\Big(|\Psi_A^{(i_c)}\rangle_{\rm e} - |\Psi_A^{(i_c)}\rangle_{\rm o}\Big) = 0 \tag{A.31}$$

so that

$$\mathrm{Tr}\rho_A = \sum_{i_c} |\alpha_{i_c}|^2 N_A(i_c) N_B(i_c) = 1 \tag{A.32}$$

Since the coefficients $|\alpha_{i_c}|^2 N_A(i_c) N_B(i_c)$ are independent of the choice of boundary spin configuration, this fixes

$$|\alpha_{i_c}|^2 N_A(i_c) N_B(i_c) = \frac{1}{\mathcal{N}_i} = 2^{1-n_i} \tag{A.33}$$

where n_i is the total number of edges crossing the boundary between A and B. This gives the entanglement entropy:

$$\begin{aligned}S_{AB} &= -\sum_{i_c} |\alpha_{i_c}|^2 N_A(i_c) N_B(i_c) \log\left[\frac{1}{2}|\alpha_{i_c}|^2 N_A(i_c) N_B(i_c)\right] \\ &= \mathcal{N}_i \frac{1}{\mathcal{N}_i} \log 2\mathcal{N}_i = n_i \log 2\end{aligned}$$

for the solid doughnut.

Since the other three regions in Fig. A.5 are simply connected, their entanglement entropy is identical to that of the toric code. The topological entanglement entropy of the 3D semion model is thus:

$$\begin{aligned}S_{\rm Top} &= -\Big[(n_i^{(1)}) - (n_i^{(2)} - 1) - (n_i^{(3)} - 1) + (n_i^{(4)} - 2)\Big]\log 2 \\ &= 0\end{aligned}$$

as one would expect for a system with no bulk topological order.

A.5 Surface plaquette operators of the 3D semion model with rough boundary

The choices of boundary conditions in 3D are similar to those in 2D, which have been discussed at length in [23, 24]. In the main text we always assumed a "smooth" boundary. Here we consider a "rough" boundary with "dangling" edges sticking out of the surface, on which open strings can terminate.

For the toric code [23, 24] one can create "partial-plaquette" operators which flip the values of two neighbouring dangling edges as well as the bulk edge connecting them. These partial-plaquette operators commute with the Hamiltonian and have the effect of allowing open string ends to move freely along the surface.

The situation with the 3DSem model is different. We will similarly be able to construct such partial-plaquette operators which commute with the bulk Hamiltonian, however, they will not commute with each other and the model is no longer exactly solvable. This is to be expected since the ends of strings on the surface should have semionic statistics with respect to each other.

The form of such a partial plaquette is show in Fig. A.7. The plaquette operator acts by flipping a pair of neighboring dangling edges (labeled 1 and 13 in the figure), together with the bulk edges connecting them ($3, 5, 7, 9$, and 11). In order that this operator commutes with the bulk plaquettes that also act on these bulk edges, we must include the usual phases depending on the edges bordering those that are flipped ($2, 4, 6, 8, 10$, and 12 in the figure), together with an extra phase depending on the value of some of the flipped edges before flipping. (In the bulk plaquette operator (2.5), these are the red and blue edges. For the surface plaquette drawn here, only one red edge (3) and one blue edge (1) are included). This gives

$$B_{p0}^{\text{surf}} = \sigma_1^x \sigma_3^x \sigma_5^x \sigma_7^x \sigma_9^x \sigma_{11}^x \sigma_{13}^x i^{n_2+n_4+n_6+n_8+n_{10}+n_{12}} i^{n_3-n_1} \tag{A.34}$$

where

$$n_i = \frac{1}{2}\left(1 - \sigma_i^z\right) \tag{A.35}$$

However, there is a problem here: B_{p0} is not Hermitian if $n_1 - n_{13}$ is odd. To compensate for this, we must add an extra phase factor $(-1)^{n_1 n_{13}}$. The final form of the surface plaquette operator shown is:

$$B_{p0}^{\text{surf}} = \sigma_1^x \sigma_3^x \sigma_5^x \sigma_7^x \sigma_9^x \sigma_{11}^x \sigma_{13}^x i^{n_2+n_4+n_6+n_8+n_{10}+n_{12}} i^{n_3-n_1} (-1)^{n_1 n_{13}} \tag{A.36}$$

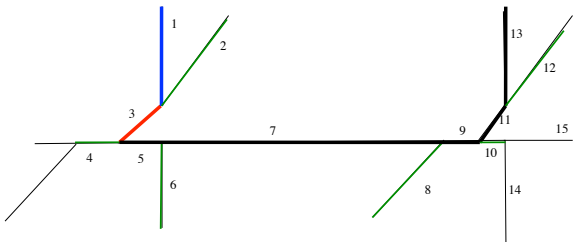


Figure A.7: A surface plaquette. The surface plaquette operator described in the text flips the thickened edges $(1, 3, 5, 7, 9,$ and $13)$. It has a phase that depends on n_i on he edges bordering those that are flipped $(2, 4, 6, 8, 10,$ and 12, shown here in green), as well as an extra phase depending on the occupancy of link 3 (red) and link 1 (blue). In this figure the dangling edges are 1 and 13.

More generally, we have

$$B_{p0}^{\text{surf}} = (\prod_{i\in\partial p} \sigma_i^x) \prod_{i\in s(p)} i^{n_i} \times i^{\sum_{j \text{ red}} n_j - \sum_{j \text{ blue}} n_j} (-1)^{\prod_{j \text{ dangling}} n_j} \tag{A.37}$$

with red and blue edges defined differently for the different plaquette orientations, as in the bulk.

A.6 Trace methods

In this section we give a more standard derivation of the ground state degeneracies of the toric code and 3DSem models: We will prove that the 3D toric code has ground state degeneracy 2^{b_1} on a manifold without boundary (and b_1 independent non-contractible cycles), whist the 3D semion model has a single ground state. For example the 3D toric code and semion model on the 3-torus have ground state degeneracies 2^3 and 1 respectively. In Sec. A.6.1 we introduce a standard method used to calculate ground state degeneracy and apply it to the 2D models. Then, in Sec. A.6.2, we generalise the method to the 3DSem model.

A.6.1 2D ground state degeneracies via trace method

In this section we algebraically deduce the ground state degeneracy of the toric-code and DSem model embedded on some 2D surface without boundary; we have already discussed the ground state degeneracy using a loop gas picture in Sec. 1.1, but we opt here for a more concrete method. This section should be viewed as preparation for the work in 3D in the next section, where we use a similar method. We define a projector onto the ground state

$$\mathcal{P} = \prod_{v \in V} \mathcal{P}_v \prod_{p \in P} \mathcal{P}_p \,, \tag{A.38}$$

where V is the set of all vertices, and P is the set of all plaquettes. In the toric code $\mathcal{P}_p = (1 + B_p)/2$ where B_p is defined in Eq. (1.1). In the DSem model $\mathcal{P}_p = (1 - B_p)/2$ where B_p is defined in Eq. (1.4). In both models $\mathcal{P}_v = (1 + B_v)$ is the same. To calculate the ground state degeneracy $\mathrm{Tr}\,(\mathcal{P})$ we write the trace as

$$\mathrm{Tr}\,(\mathcal{P}) = 2^{-V-F}\,\mathrm{Tr}\left[\prod_{v \in V}(1 + \mathcal{K}_v)\prod_{p \in P}(1 + \mathcal{K}_p)\right] \tag{A.39}$$

$$= 2^{-V-F}\sum_{S_V \subseteq V}\sum_{S_P \subseteq P}\mathrm{Tr}\left[\prod_{v \in V}\mathcal{K}_v \prod_{p \in P}\mathcal{K}_p\right] \tag{A.40}$$

where $\mathcal{K}_v = 2\mathcal{P}_v - 1$ and $\mathcal{K}_p = 2\mathcal{P}_p - 1$. Here S_V and S_P are subsets of the set of all vertices and plaquettes respectively. For the toric code and DSem model, all of the terms in the sum are zero except for the four corresponding to $(S_V, S_P) \in \{(\emptyset, \emptyset)\,, (V, \emptyset)\,, (\emptyset, P)\,, (V, P)\}$. For each of these $2^2 = 4$ choices, $\prod_{v \in S_V}\mathcal{K}_v \prod_{p \in S_P}\mathcal{K}_p = \mathbf{1}$, and so

$$\begin{aligned}\mathrm{Tr}\,(\mathcal{P}) &= 2^{2-V-F}\mathrm{Tr}\,[\mathbf{1}] \\ &= 2^{2-\chi}\end{aligned} \tag{A.41}$$

where $\chi = V - E + F$ is the Euler characteristic of the surface tiled by the lattice. Therefore the ground state degeneracy of the 2D toric code, and DSem is $2^{2-\chi} = 2^g$ on a surface of genus g.

To see how the above argument works in detail for the toric code note that $\mathcal{K}_p = B_p$ acts on each edge of plaquette p with a σ^x i.e. it flips the spin on each edge of p. Therefore the product $\prod_{p \in S_P}\mathcal{K}_p$ acts in the following way. Edges that do not belong to a plaquette in S_P are unchanged, and those that belong to two plaquettes are also left unchanged because they are flipped twice. However, those edges belonging to just one plaquette in S_P are flipped once by $\prod_{p \in S_P}\mathcal{K}_p$; we will call these boundary edges. If the operator has boundary edges then for any state $\mid \psi\rangle$ in our $\sigma^z = \pm 1$ spin basis $\langle\psi \mid \prod_{v \in S_V}\mathcal{K}_v \prod_{p \in S_P}\mathcal{K}_p \mid \psi\rangle = 0$, because $\prod_{p \in S_P}\mathcal{K}_p$ will flip at least one edge in $\mid \psi\rangle$ to an orthogonal state, and $\prod_{v \in S_V}\mathcal{K}_v$ cannot undo this. Therefore we need only worry about terms for which $\prod_{p \in S_P}\mathcal{K}_p$ has no boundary edges, which occurs when $S_P = \emptyset$ or P. In both cases $\prod_{p \in S_P}\mathcal{K}_p = 1$, therefore

$$\mathrm{Tr}\left(\mathcal{P}\right) = 2^{-V-F} \times 2 \times \sum_{S_V \subseteq V} \mathrm{Tr}\left[\prod_{v \in S_V} \mathcal{K}_v\right] \tag{A.42}$$

We use a similar line of reasoning to show that only two terms survive the remaining sum. Note that $\mathcal{K}_v$ is -1 if vertex v has an odd number of 1-strings entering it, and -1 otherwise. Therefore the product $\prod_{v \in S_V} \mathcal{K}_v$ acts in the following way. Edges that do not belong to a vertex in S_V are unchanged, and those that belong to two vertices in S_V are also unchanged because $\left(\sigma^z\right)^2 = 1$. However, those boundary edges belonging to just one vertex in S_V are acted on with σ^z. The fact that σ^z is traceless implies that $\mathrm{Tr}\left[\prod_{v \in S_V} \mathcal{K}_v\right] = 0$ unless $\prod_{v \in S_V} \mathcal{K}_v$ has no boundary edges i.e. unless $S_V = \emptyset$ or V. In both cases $\prod_{v \in S_V} \mathcal{K}_V = 1$, therefore

$$\begin{aligned} \mathrm{Tr}\left(\mathcal{P}\right) &= 2^{2-V-F} \mathrm{Tr}\left[\mathbf{1}\right] \\ &= 2^{2-(V-E+F)} \\ &= 2^{2-\chi} \end{aligned} \tag{A.43}$$

where χ is the Euler characteristic of the surface that the lattice tiles, and so the ground state degeneracy of the toric code is 2^{2g} where the integer g is the genus of the surface. Indeed the answer is the same in the case of DSem because the $\mathcal{K}_v$ are the same and the $\mathcal{K}_p = -B_p$ still flip edges; the only non-trivial fact to check is that $\prod_{p \in P} \mathcal{K}_p = 1$. To act with $\prod_{p \in P} \mathcal{K}_p = (-1)^F \prod_{p \in P} B_p$ we can first fuse the B_p operators on each edge (which gives a factor of -1 for each edge). All that remain are the closed 1-loops on each vertex, which give a factor of -1 for each vertex. In total, $\prod_{p \in P} \mathcal{K}_p = (-1)^{V-E+F} = (-1)^{2g} = 1$. Hence we have proved the statement in Eq. (A.43).

A.6.2 3D ground state degeneracies via trace method

Having calculated the ground state degeneracies of the 2D models, we now apply similar methods to the 3D toric code and 3DSem on manifolds without boundary. We will confirm the results presented in Sec. 2.2.1.1: The 3D toric code has degeneracy 2^{b_1} where b_1 (the first Betti number) is the number of independent non-contractible cycles in the closed 3-manifold, while the semion model has a single ground state.

Following our work in 2D Sec. A.6.1, we cast the ground state degeneracy in the form

$$\mathrm{Tr}\,(\mathcal{P}) = 2^{-V-F} \sum_{S_V \subseteq V} \sum_{S_P \subseteq P} \mathrm{Tr}\left[\prod_{v \in V} \mathcal{K}_v \prod_{p \in P} \mathcal{K}_p \right], \tag{A.44}$$

where $\mathcal{K}_v = 2\mathcal{P}_v - 1$ and $\mathcal{K}_p = 2\mathcal{P}_p - 1$. We evaluate terms in the above sum, first for the toric code and then for the semion model.

3D toric code: $\mathcal{K}_p = B_p$ flips the spin on each edge of plaquette p. Therefore the product $\prod_{p \in S_P} \mathcal{K}_p$ acts in the following way. Edges that do not belong to a plaquette in S_P are unchanged, and those that belong to an even number of plaquettes are also left unchanged because they are flipped twice. However, those edges belonging to an odd number of plaquettes in S_P are on net flipped once by the operator $\prod_{p \in S_P} \mathcal{K}_p$; we again call these boundary edges. If the operator has boundary edges then for any state $\mid \psi \rangle$ in our $\sigma^z = \pm 1$ spin basis

$$\langle \psi \mid \prod_{v \in S_V} \mathcal{K}_v \prod_{p \in S_P} \mathcal{K}_p \mid \psi \rangle = 0\,, \tag{A.45}$$

because $\prod_{p \in S_P} \mathcal{K}_p$ will flip at least one edge in $\mid \psi \rangle$ to an orthogonal state, and $\prod_{v \in S_V} \mathcal{K}_v$ cannot undo this. Therefore (A.45) is zero, except possibly when S_P has no boundary edges. It can be shown (see below) that there are 2^{b_1+C-1} sets S_P with no boundary edges, where C is the number of cubes on the lattice. Furthermore $\prod_{S_P} \mathcal{K}_p = 1$ for S_P with no boundary edges. This leaves us with a ground state degeneracy of

$$\begin{aligned} \mathrm{Tr}\,(\mathcal{P}) &= 2^{-V-F} \times 2^{b_1+C-1} \times \sum_{S_V \subseteq V} \mathrm{Tr}\left[\prod_{v \in S_V} \mathcal{K}_v \right] \\ &= 2^{-V-F} \times 2^{b_1+C-1} \times 2^{1+E} \\ &= 2^{b_1-\chi} \\ &= 2^{b_1} \end{aligned} \tag{A.46}$$

where $\chi = C - F + E - V$ is the Euler characteristic, which is zero for closed 3-manifolds (Poincaré duality). To show the second equality we used the fact that $\prod_{v \in S_V} \mathcal{K}_v$ is traceless unless $S_V = \emptyset$ or V (see Sec. A.6.1). In both cases $\prod_{v \in S_V} \mathcal{K}_v = 1$.

To justify the factor of 2^{b_1+C-1} above, note that a set S_P without boundary can be visualised as a set of possibly intersecting surfaces without boundary. Consider first those S_P with surfaces that can be contracted to a point. Such an S_P can be said to form the boundary of one of two sets of cubes: S_C or its complement $C - S_C$, where

C is the set of all cubes. Therefore those S_P whose surfaces can be contracted to a point can be put into 1:2 correspondence with the set of subsets of C, and so there are 2^{C-1} such S_P. But not all S_P have surfaces that can be contracted to a point. In fact there are 2^{b_2} topological classes of surface where b_2 is the second Betti number (which for oriented closed three manifolds obeys $b_2 = b_1$). Each of these classes of surface can be shown to contain 2^{C-1} elements in the same way we showed above for surfaces that could be contracted to a point.

3D semion: Having found that the ground state is degenerate for the toric code on closed 3-manifolds, we now show that the ground state is non-degenerate for the semion model on any oriented closed 3-manifold. We start again with (A.44) recasting it as

$$\mathrm{Tr}\left(\mathcal{P}\right) = 2^{-F} \times \sum_{S_P \subseteq P} \mathrm{Tr}\left[\prod_{v\in V} \mathcal{P}_v \prod_{p\in S_P} \mathcal{K}_p\right]. \tag{A.47}$$

The $\mathcal{K}_p = -B_p$ operators in the 3DSem flip each edge of the plaquette p (albeit with possible phases), so we can use the same reasoning as for the toric code to show that $\prod_{p\in S_P} \mathcal{K}_p$ is traceless unless S_P has no boundary edges. We found before that there were b_2 types of S_P without boundary edges by remembering that any such S_P can be visualised as a set of possibly intersecting surfaces without boundary. This has not changed. However we will find that only one of these b_1 types of surface gives non-zero trace: $\prod_{p\in S_P} \mathcal{K}_p$ is traceless unless S_P has no boundary edges and can be represented as a contractible surface.

To see how this works we recall the result shown in Eq. (2.9) that $P_{n(S_P)_\perp} = \prod_{p\in S_P}(-B_p)$, where $P_{n(S_P)_\perp}$ is the parity ± 1 of the number of loops crossing the non-contractible closed surface defined by S_P, which we say has normal $n(S_P)$. Therefore

$$\mathrm{Tr}\left[\prod_{v\in V} \mathcal{P}_v \prod_{p\in S_P} \mathcal{K}_p\right] = \mathrm{Tr}\left[\prod_{v\in V} \mathcal{P}_v P_{n(S_P)_\perp}\right] \tag{A.48}$$

However, consider the invertible operator $\hat{S} = \prod_{i\in\mathcal{C}_n} \sigma_i^x$, where $\mathcal{C}_n$ is a closed path cutting S_P once perpendicularly. Notice that $\hat{S}$ commutes with $\mathcal{P}_v$ but anti-commutes with the parity $P_{n(S_P)_\perp}$ so that

$$\begin{aligned}\mathrm{Tr}\left[\prod_{v\in V} \mathcal{P}_v P_{n(S_P)_\perp}\right] &= \mathrm{Tr}\left[\hat{S}^{-1}\prod_{v\in V} \mathcal{P}_v P_{n(S_P)_\perp}\hat{S}\right] \\ &= -\,\mathrm{Tr}\left[\prod_{v\in V} \mathcal{P}_v P_{n(S_P)_\perp}\right]\end{aligned} \tag{A.49}$$

Hence, the trace must be zero for S_P non-contractible. If S_P is contractible, then an odd number of fluxes pierce it only if it encloses vertex violations, but such states are projected out by $\prod_{v\in V}\mathcal{P}_v$. Therefore

$$\begin{aligned}
\mathrm{Tr}\left(\mathcal{P}\right) &= 2^{-F}\times\sum_{S_P\in\mathcal{E}}\mathrm{Tr}\left[\prod_{v\in V}\mathcal{P}_v\prod_{p\in S_P}\mathcal{K}_p\right]\\
&= 2^{-F}\times|\mathcal{E}|\times\mathrm{Tr}\left[\prod_{v\in V}\mathcal{P}_v\right]\\
&= 2^{-F}\times 2^{C-1}\times 2^{1-V}\mathrm{Tr}\left[\mathbf{1}\right]\\
&= 2^{-\chi}\\
&= 1
\end{aligned}\tag{A.50}$$

where χ is the Euler characteristic (which disappears for closed 3-manifolds), and $\mathcal{E}$ is the set of closed and contractible S_p's which has size 2^{C-1} (as reasoned in the case of the toric code).

Appendix B

Appendices for Chapter 3

B.1 Hamiltonian formulation of $bF + bb$ theory for $k \in \mathbb{Z}, p = 2k$

Here we identify a Hamiltonian for the $k \in \mathbb{Z}, p = 2k$ dyon condensed phases starting from the $bF + bb$ theory in Eq. (3.14). First we express the partition function for the field theory as a Trotter decomposition (Sec. B.1.1), and deduce from this the effective Hamiltonian (Sec. B.1.2). The Hamiltonian obtained is that of the $\mathbb{Z}_{2k}^{(1)}$ Walker-Wang model [3]. The special case $k = 1, p = 2$ corresponds to the fermionic toric code covered in Sec. 3.2.2. When $k > 1$ is odd, the surface has the topological order of a $\nu = 1/k$ Laughlin state and the bulk has fermionic toric code $\mathbb{Z}_2^{(1)}$ topological order. When k is even, the surface has the topological order of a $\nu = 1/(k/2)$ Laughlin state coupled to a bulk bosonic $\mathbb{Z}_2$ gauge theory.

B.1.1 Trotter decomposition

The $bF + bb$ Lagrangian density, in the presence of static charges and line defects (j^0, Σ^{0i}), can be written

$$-ib \wedge F - \frac{i2\pi}{p} b \wedge b - iJ^0 A_0 - i\Sigma^{0i} b_{0i} + \epsilon_V \mathcal{G}(e^{i\frac{2\pi}{p} j^0}) + \epsilon_P \mathcal{F}(e^{i\Sigma^{0i}}) \tag{B.1}$$

where $F = dA$, and $A \in \{0, 1, \ldots, p-1\}\frac{2\pi}{p}$, and where $b_{0i}, \frac{1}{2}\epsilon_{ijk} b_{jk} \in \{0, 1, \ldots, p-1\}$. We remind the reader that A lives on the edges of the 4D lattice, while b lives on the faces of the dual lattice (Sec. 3.2.1). The fields $J^0, \Sigma^{0i}\frac{p}{2\pi}$ take values in $\{0, 1, 2, \ldots, p-1\}$. The $\mathcal{F}, \mathcal{G}$ functions endow these defects with an energy cost. As neither function has an explicit A, b dependence, we will ignore them for now. To begin, sum out A_0 to get partition function

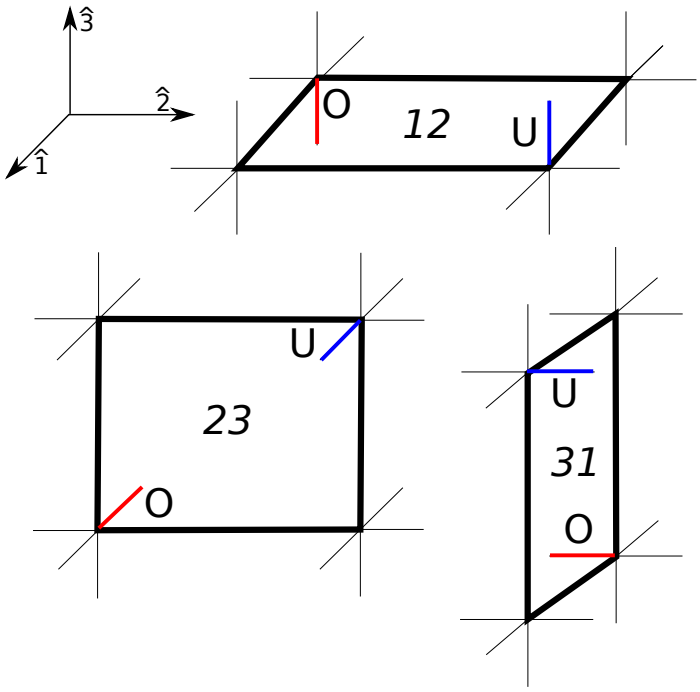


Figure B.1: For each of the three types of plaquettes (in the 12, 23 and 31 planes) this figure denotes two privileged edges used to define the operator $\hat{B}_P$ in Eq. (3.30).

$$\sum_{\{b\}}{}' \sum_{\{\tilde{A}\}} \exp\left[\sum_r (ib \wedge d\tilde{A} + \frac{i2\pi}{p} b \wedge b + \Sigma^{0i} b_{0i})\right] , \tag{B.2}$$

where $\tilde{A}_\mu$ contains only the remaining space-like components of A, and where $\sum'$ is a sum over b configurations constrained by $\epsilon_{ijk}\partial_i b_{jk} = J_0 \mod p$. Now sum out the time-like components of b (i.e. b_{0k}), to get

$$\begin{aligned} &\sum_{\{A_i,s_i\}}{}' \exp\left[\sum_{r,i} -i\left(s_{r,i} - s_{r-\hat{0},i}\right) A_{r,i}\right] \\ &\times \prod_{(r,\hat{i},\hat{j})} \left[\sum_{l=0}^{p-1} e^{il\Sigma^{0k}(r)} \left(\Phi_{(r,\hat{i},\hat{j})} \times T_{r+\hat{i}+\hat{j},k} T_{r-\hat{k}-\hat{0},k}\right)^l\right] \end{aligned} \tag{B.3}$$

where we have relabelled the variables $b_{jk}(r) \to \epsilon_{ijk} s_{r,i}$ for the remaining space-like components of b, and $A_i(r) \to A_{r,i}$ for the remaining space-like components of A. The product in the second line is over all space-like plaquettes at all times, $(r, \hat{i}, \hat{j})$, where $ij = 12, 23$ or 31. Within this product, the index $k = 1, 2, 3$ is fixed by the requirement $\epsilon_{ijk} = 1$. We have used the definitions

$$\Phi_{(r,\hat{i},\hat{j})} = e^{iF_{ij}(r)}$$
$$T_{r,i} = e^{\frac{i2\pi}{p}s_{r,i}}$$

in Eq. (B.3). In terms of the new s_i variables, $\sum'$ means we only consider configurations of s_i obeying vertex constraint $\partial_i s_{r,i} = J_0(r) \mod p$ at each vertex r of the lattice within each time slice. To form the effective Hamiltonian, we express the partition function Eq. (B.3) as a product over space-like slices indexed by time co-ordinate $r^0 = n$

$$\sum_{\{A_e,s_e\}}{}' \prod_n \left\{ \exp\left[\sum_e -i\left(s_e^{(n)} - s_e^{(n-1)}\right) A_e^{(n)}) \right] \right.$$
$$\left. \times \prod_P \left[\sum_{l=0}^{p-1} e^{il\Sigma_P} \left(\Phi_P^{(n)} \times T_{U(P)}^{(n)} T_{O(P)}^{(n-1)} \right)^l \right] \right\} \tag{B.4}$$

where the P labels oriented $12, 23, 31$ plaquettes on a 3D cubic lattice. On the other hand, e, V label edges and vertices respectively of the cubic lattice. The edges are by default oriented in the $+\hat{1}, +\hat{2}, +\hat{3}$ directions. In Eq. B.4, $\Phi_P^{(n)}, \Sigma_P$ is shorthand for the value of Φ, Σ on a plaquette P of the cubic lattice at time slice n; note Σ_P does not require a time slice co-ordinate as it represents a static line defect. $T_{U(P)}^{(n)}, T_{O(P)}^{(n-1)}$ denote the values of T on two edges $U(P), O(P)$ at time-slices $n, n-1$ respectively. If P is the $ij \in 12, 23, 31$ plaquette on the 3D cubic lattice at vertex $\mathbf{r}$, then $U(P)$ is the edge $(\mathbf{r} + \hat{i} + \hat{j}, \hat{k})$ while $O(P)$ is the edge $(\mathbf{r} - \hat{k}, \hat{k})$, where k is uniquely specified by $\epsilon_{hij} = 1$; see Fig. B.1. $s_e^{(n)}, A_e^{(n)}$ denote the values of s, A on the space-like edge e, at time-slice n.

Now notice that the second line of Eq. (B.4) imposes a constraint

$$\mathcal{B}_P^{(n)} \equiv \Phi_P^{(n)} \times T_{U(P)}^{(n)} T_{O(P)}^{(n-1)} = e^{-i\Sigma_P} \,. \tag{B.5}$$

We remind the reader that the Φ, T depend only on A, s respectively. Moreover, the Gauss constraint which holds at each vertex V and time slice n, can be written

$$\mathcal{Q}_V^{(n)} \equiv \prod_{e \in s(V)} \left(T_e^{(n)}\right)^{\nu_{e,V}} = e^{\frac{i2\pi}{p} J_0(V)} \,, \tag{B.6}$$

where $s(V)$ denotes the six edges attached to a vertex V, and $\nu_{e,V} = \pm 1$ depending on whether e is oriented towards or away from V. We can now reintroduce the $\mathcal{F}, \mathcal{G}$

functions from Eq. (B.1); these depended on static sources J^0, Σ^{0i}, but we can use the constraints Eq. (B.5) and Eq. (B.6) to remove all explicit dependence on J^0, Σ^{0i}

$$\sum_{\{A_e, s_e\}}{}' \prod_n \left\{ \exp\left[\sum_e -i \left(s_e^{(n)} - s_e^{(n-1)} \right) A_e^{(n)} \right) \right] \times \exp\left[\epsilon_v \sum_V \mathcal{G}\left(\mathcal{Q}_V^{(n)} \right) + \epsilon_p \sum_P \mathcal{F}\left(\mathcal{B}_P^{(n)} \right) \right] \right\} . \tag{B.7}$$

B.1.2 The effective Hamiltonian

Having expressed the classical partition function as Eq. (B.4), it is relatively straightforward to rewrite it as $\operatorname{Tr} e^{-\hat{H}_{\text{eff}}\tau}$ where $\hat{H}_{\text{eff}}$ is a 3D quantum Hamiltonian. In Eq. (B.4), $s_i, \frac{pA_i}{2\pi} = 0, 1, 2, \ldots p-1$ are classical variables, but they become quantum mechanical operators $\hat{s}_i, \hat{A}_i$ in the Hamiltonian formulation of this problem. These operators obey commutation relations

$$\left[\hat{A}_{r',j'}, \hat{s}_{r,j} \right] = i\delta_{r,r'}\delta_{j,j'} \mod p , \tag{B.8}$$

and the local Hilbert space on an edge e of the cubic lattice has two obvious bases with p elements

$$\hat{A}_e |A_e\rangle = A_e |A_e\rangle , A_e \in \frac{2\pi}{p} \{0, 1, \ldots, p-1\}$$
$$\hat{s}_e |s_e\rangle = s_e |s_e\rangle , s_e \in \{0, 1, \ldots, p-1\} .$$

It is convenient to construct operators $\hat{W}_e = e^{i\hat{A}_e}, \hat{T}_e = e^{\frac{i2\pi}{p}\hat{s}_e}$, and pick a phase convention for the bases such that

$$\hat{W}_e |s_e\rangle = |s_e + 1\rangle$$
$$\hat{T}_e |A_e\rangle = \left| A_e - \frac{2\pi}{p} \right\rangle .$$

We are now ready to quantise Eq. (B.4). It follows from Eq. B.8 that

$$\langle s_e'|\ A_e\rangle \langle A_e|\ s_e\rangle = e^{-i(s_e' - s_e)A_e}$$

which allows us to re-express the partition function as

$$\sum_{\{A_e,s_e\}}{}' \prod_{n=r^0} \left\{ \left[\prod_e \left\langle s_e^{(n)} \right| A_e \rangle \left\langle A_e \right| s_e^{(n-1)} \right\rangle \right] \times \exp\left[\epsilon_v \sum_V \mathcal{G}\left(\mathcal{Q}_V^{(n)}\right) + \epsilon_p \sum_P \mathcal{F}\left(\mathcal{B}_P^{(n)}\right) \right] \right\} .$$

We can collect the products over bras and kets to form

$$\sum_{\{A_e,s_e\}}{}' \prod_n \Bigg\{ \left\langle \{s^{(n)}\} \right| \prod_P e^{\epsilon_p \sum_P \mathcal{F}\left(\Phi_P^{(n)} \times T_{U(P)}^{(n)} T_{O(P)}^{(n-1)}\right)} \times \left| \{A^{(n)}\} \right\rangle \left\langle \{A^{(n)}\} \right| \left\{s^{(n-1)}\right\} \rangle \times e^{\epsilon_v \sum_V \mathcal{G}\left(\mathcal{Q}_V^{(n)}\right)} \Bigg\}$$

where $\left|\{s^{(n)}\}\right\rangle = \otimes_e \left|s_e^{(n)}\right\rangle$ and $\left|\{A^{(n)}\}\right\rangle = \otimes_e \left|A_e^{(n)}\right\rangle$. We have also moved the $\mathcal{F}$ terms between the kets. We can now replace $\Phi_P^{(n)}$ by the operator $\hat{\Phi}_P$ by substituting $A_e^{(n)} \to \hat{A}_e$

$$\sum_{\{A_e,s_e\}}{}' \prod_n \Bigg\{ \left\langle \{s^{(n)}\} \right| \prod_P e^{\epsilon_p \sum_P \mathcal{F}\left(\hat{\Phi}_P \times T_{U(P)}^{(n)} T_{O(P)}^{(n-1)}\right)} \times \left| \{A^{(n)}\} \right\rangle \left\langle \{A^{(n)}\} \right| \left\{s^{(n-1)}\right\} \rangle \times e^{\epsilon_v \sum_V \mathcal{G}\left(\mathcal{Q}_V^{(n)}\right)} \Bigg\} .$$

Summing over A_e, and using $\hat{I} = \sum_{A_e^{(n)}} \left|\{A^{(n)}\}\right\rangle \left\langle \{A^{(n)}\}\right|$ gives

$$\sum_{\{s_e\}}{}' \prod_n \left\langle \{s^{(n)}\} \right| \prod_P e^{\epsilon_p \sum_P \mathcal{F}\left(\hat{\Phi}_P \times T_{U(P)}^{(n)} T_{O(P)}^{(n-1)}\right)} \left| \{s^{(n-1)}\} \right\rangle \times e^{\epsilon_v \sum_V \mathcal{G}\left(\mathcal{Q}_V^{(n)}\right)} \tag{B.9}$$

where the T variables are currently still numbers depending on the s variables, rather than operators. The product between the kets in Eq. (B.9) Taylor expands to a sum of expressions of the form

$$\left\langle \{s^{(n)}\} \right| \prod_{P \in S} \left[T_{U(P)}^{(n)} T_{O(P)}^{(n-1)} \hat{\Phi}_P \right]^{j_P} \left| \{s^{(n-1)}\} \right\rangle , \tag{B.10}$$

where the $j'_P s$ are some integers and S is some set of space-like plaquettes P. Now, we can replace the $s, T = e^{\frac{i2\pi}{p} s}$ variables by $\hat{s}, \hat{T} = e^{\frac{i2\pi}{p} \hat{s}}$ operators respectively to rewrite Eq. (B.10) as

$$\left\langle \{s^{(n)}\} \right| \left(\prod_{P \in S} \hat{T}_{U(P)}^{j_P} \right) \left(\prod_{P \in S} \hat{\Phi}_P^{j_P} \right) \left(\prod_{P \in S} \hat{T}_{O(P)}^{j_P} \right) \left| \{s^{(n-1)}\} \right\rangle \ . \tag{B.11}$$

This, we will show, can be rearranged to

$$\left\langle \{s^{(n)}\} \right| \prod_{P \in S} \left[\hat{T}_{U(P)} \hat{T}_{O(P)} \hat{\Phi}_P \right]^{j_P} \left| \{s^{(n-1)}\} \right\rangle \ . \tag{B.12}$$

One might worry about the phases accrued in permuting the $\hat{T}, \hat{\Phi}$ operators to go between Eq. (B.11) and Eq. (B.12). If $e \in \partial P$ then note that

$$\hat{T}_e \hat{\Phi}_P = \hat{\Phi}_P \hat{T}_e e^{\frac{i2\pi}{p} \nu_{e,P}}$$

where $\nu_{e,P}$ is the orientation of e in the boundary of P. But all of these phases cancel, and the underlying reason is that the operators $\hat{T}_{U(P)} \hat{T}_{O(P)} \hat{\Phi}_P$ commute amongst themselves. In more detail, to rearrange Eq. B.12 to form Eq. B.11 we need to move every $\hat{T}_U$ operator to the left of the product and every $\hat{T}_O$ operator to the right of the product. Consider two plaquettes P, Q. If e is in the boundary of P (i.e. $e \in \partial P$) with orientation ν but is also an U edge of Q ($e = U(Q)$, it follows by inspection of Fig. B.1 that there exists a unique $f \in \partial Q$ with $\nu_{f,Q} = \nu$ such that f is a O edge of p i.e., $f = O(P)$. This tells us the following. We need to move $\hat{T}_e$ to the left of Eq. B.12 because e is an U edge, and we also need to move $\hat{T}_f$ to the right because it is a O edge. If, in Eq. B.12, Q lies to the left of P, $\hat{T}_e$ will not meet the plaquette operator at Q and $\hat{T}_f$ will not meet the plaquette operator at P. If Q lies to the right of P, $\hat{T}_e$ encounters the P plaquette operator and it will accrue a net $e^{-\frac{i2\pi}{p} \nu_{e,P} j_P j_Q}$ sign because $e \in \partial P$. However as Q is to the right of P, we will also need to move the O edge f of plaquette P to the right of Eq. B.12. It will need to move through the Q plaquette operator, and because $f \in \partial P$ it will acquire a $e^{\frac{i2\pi}{p} \nu_{f,Q} j_P j_Q}$ phase as it does so. In either case, there is no net phase because $\nu_{e,P} = \nu_{f,Q}$. We can proceed inductively, to prove that Eq. B.12 equals Eq. B.11. Having shown this, we can go back to our expression for the partition function and recast it as

$$\begin{aligned} \sum_{\{s_e\}}{}' \prod_n \Big\langle \{s^{(n)}\} \Big| \prod_P e^{\epsilon_p \sum_P \mathcal{F}\left(\hat{\Phi}_P \times \hat{T}_{O(P)} \hat{T}_{U(P)}\right)} \Big| \{s^{(n-1)}\} \Big\rangle \\ \times e^{\epsilon_v \sum_V \mathcal{G}\left(\mathcal{Q}_V^{(n)}\right)} \ . \end{aligned} \tag{B.13}$$

We can now move the $\mathcal{Q}_V^{(n)}$ fields in-between the kets and replace them by operators

$$\hat{B}'_V \equiv \prod_{e\in s(V)} \hat{T}_{e,\nu_{e,V}} = e^{\frac{i2\pi}{p}J_0(V)}\,. \tag{B.14}$$

where $s(V)$ are the six edges incoming to vertex V, and $\nu_{e,V} = \pm 1$ depending on whether e is oriented towards/away from V respectively. This gives

$$\sum_{\{s_e\}}{}' \prod_n \left\{ \left\langle \{s^{(n)}\} \right| e^{-\hat{H}_{\text{eff}}\Delta\tau} \left| \{s^{(n-1)}\} \right\rangle \right\} ,$$

where we define $\hat{H}_{\text{eff}}$ implicitly through

$$e^{-\hat{H}_{\text{eff}}\Delta\tau} = \exp\left[\epsilon_P \sum_P \mathcal{F}\left(\hat{B}'_P\right)\right] \exp\left[\epsilon_V \sum_V \mathcal{G}\left(\hat{B}'_V\right)\right] \tag{B.15}$$

and we defined

$$\begin{aligned}
\hat{B}'_P &\equiv \left(\hat{\Phi}_P \hat{\Theta}_P\right)^l \\
\hat{\Phi}_P &\equiv \prod_{e=(\mathbf{r},\hat{i})\in\partial P} \hat{W}_e^{\nu_{e,P}} \\
\hat{\Theta}_P &\equiv \hat{T}_{U(P)} \hat{T}_{O(P)}\,.
\end{aligned} \tag{B.16}$$

Here $U(P), O(P)$ are shorthand for the edges $(r+\hat{i}+\hat{j},\hat{k}), (r-\hat{k},\hat{k})$ transverse to the plaquette $P = (x,\hat{i},\hat{j})$ where $\epsilon_{hij} = 1$; see Fig. B.1. Also, $\nu_{e,P}$ is the orientation of the edge $e = (\mathbf{r},\hat{i})$ in the plaquette boundary ∂P. It is straightforward to verify that the operators $\hat{B}'_V$ and $\hat{B}'_P$ commute amongst themselves so we can combine the exponents in Eq. (B.15) to get

$$\hat{H}_{\text{eff}}\Delta\tau = -\epsilon_V \sum_V \mathcal{G}\left(\hat{B}'_V\right) - \epsilon_P \sum_P \mathcal{F}\left(\hat{B}'_P\right) \tag{B.17}$$

We now specify functions $\mathcal{G}, \mathcal{F}$. We want both functions to penalise configurations with non-vanishing Σ^{0i} and J^0. A simple option is to take $\mathcal{G}(\kappa) = \mathcal{F}(\kappa) \equiv p\delta_{\kappa,1} - 1$, which penalises all non-vanishing defects equally, and leads to the Hamiltonian

$$H\Delta\tau = -\epsilon_v \sum_V \hat{B}_V - \epsilon_p \sum_P \hat{B}_P\,, \tag{B.18}$$

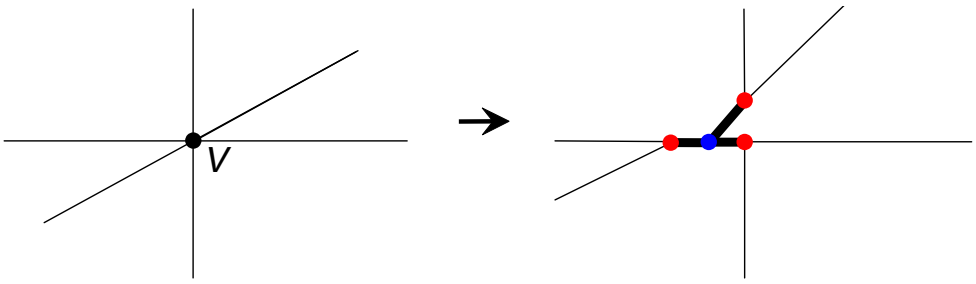
where

$$\begin{aligned}
\hat{B}_V &= \sum_{l=1}^{p-1} \left(\hat{B}'_V\right)^l \\
\hat{B}_P &= \sum_{l=1}^{p-1} \left(\hat{B}'_P\right)^l .
\end{aligned} \tag{B.19}$$

The ground states and topological properties of excitations do not depend on the precise form of $\mathcal{F}, \mathcal{G}$, provided these functions are maximised for configurations with $\hat{B}'_V = \hat{B}'_P = 1$.

B.1.3 Connection to $\mathbb{Z}_p^{(1)}$ Walker-Wang models on the point-split lattice

The Hamiltonian defined in Eq. (B.18) acts on a Hilbert space made up of all the edges on a cubic lattice. It is straightforward to extend the definition of the Hamiltonian, so that it acts on a trivalent point-split lattice Fig. 2.1. Introduce three new (bold black) edges at each vertex



. (B.20)

The Hilbert space of the new lattice is larger than that of the cubic lattice, although in practice this has no significant effect on the physics. Every vertex is trivalent, and plaquettes now have ten edges in their boundaries. The Hamiltonian on this new lattice is very similar to Eq. (B.18). First fix orientations for the new edges. Each vertex has a vertex operator defined as in Eq. (B.14) but where $s(V)$ now denotes just three edges instead of six. The plaquette operators are formed in the same way as Eq. (B.16), except ∂P now contains ten edges instead of four.

The resulting Hamiltonian is precisely the Walker-Wang model constructed from the $\mathbb{Z}_p^{(1)}$ category on the point-split lattice, using the graphical construction detailed in Sec. 2.4.1.[1] When $p = 2k$ and k is odd, this category is $\mathbb{Z}_p^{(1)} = \mathbb{Z}_k^{(2)} \times \mathbb{Z}_2^{(1)}$ [28]. For example, when $p = 2k = 6$ we get the Walker-Wang model based on category $\mathrm{U}(1)_3 = \mathbb{Z}_3^{(2)} \times \mathbb{Z}_2^{(1)}$, which has the anyons of a $\nu = 1/3$ Laughlin state on its surface Sec. 2.5.2.

B.2 $k = \mathbf{even}, p = k$

In the previous section, we showed that the $k \in \mathbb{Z}, p = 2k$ $bF + bb$ theory is precisely the $\mathbb{Z}_{2k}^{(1)}$ Walker-Wang model. However, our heuristic discussion in Sec. 3.1 also sug-

[1] See section 5.1 of [28] for a definition of this category.

gests that the $\mathbb{Z}_k^{(1/2)}$ Walker-Wang model (constructed from the $\mathrm{U}(1)_k$ Chern-Simons theory) is described by the same $bF + bb$ field theory with $k = \text{even}, p = k$. In this case, however, we run into a technical obstacle in making the $bF + bb \leftrightarrow WW$ correspondence rigorous. In particular, for a lattice version of the field theory to be equivalent to the $\mathbb{Z}_k^{(1/2)}$ Walker-Wang model, we would expect the action to be periodic modulo 2π under $b \to b + k\eta$ for arbitrary integer two-form η, reflecting the fact that label k strings in the WW ground state are trivial. However, this fails to be true if we use the definition of $b \wedge b$ in Eq. (3.19).

The work in [43] suggests we adopt a different definition of the wedge product. They define their field theories (which are related to $bF + bb$ theories) on a simplicial manifold, and they use the 'Pontryagin square' operation to define $b \wedge b$. The Pontryagin square is a simple extension of the standard cup product $b \cup b$ in simplicial cohomology to $b \cup b + b \cup_1 db$, where $\cup_1$ is a mathematical operation called a 'Steenrod square'. (The cup product is the simplicial manifold analogue of the wedge product that we use here). We expect that with a similar refinement of the wedge product on the hypercubic lattice Eq. (3.19), one could use the methods of App. B.1 to derive the $\mathbb{Z}_k^{(1/2)}$ Walker-Wang models from the $p = k$ even $bF + bb$ action.

Bibliography

[1] C. W. von Keyserlingk, F. J. Burnell, and S. H. Simon, Phys. Rev. B **87**, 045107 (2013).

[2] C. W. von Keyserlingk and F. J. Burnell, arXiv preprint arXiv:1405.2988 (2014).

[3] F. J. Burnell, C. W. von Keyserlingk, and S. H. Simon, Phys. Rev. B **88**, 235120 (2013).

[4] D. C. Tsui, H. L. Stormer, and A. C. Gossard, Phys. Rev. Lett. **48**, 1559 (1982).

[5] G. Prange and S. M. Girvin, The Quantum Hall Effect, Graduate texts in contemporary Physics, 1987.

[6] X.-G. Wen, Physical Review B **40**, 7387 (1989).

[7] X.-G. Wen, International Journal of Modern Physics B **4**, 239 (1990).

[8] M. Levin and X.-G. Wen, Physical review letters **96**, 110405 (2006).

[9] A. Kitaev and J. Preskill, Phys. Rev. Lett. **96**, 110404 (2006).

[10] R. Dijkgraaf and E. Witten, Communications in Mathematical Physics **129**, 393 (1990).

[11] A. Y. Kitaev, Annals of Physics **303**, 2 (2003).

[12] M. A. Levin and X.-G. Wen, Phys. Rev. B **71**, 045110 (2005).

[13] A. Y. Kitaev, Annals of Physics **321**, 2 (2006).

[14] M. Freedman, C. Nayak, K. Shtengel, K. Walker, and Z. Wang, Annals of Physics **310**, 428 (2004).

[15] J. C. Y. Teo and C. L. Kane, Phys. Rev. Lett. **104**, 046401 (2010).

[16] M. Freedman, M. B. Hastings, C. Nayak, X.-L. Qi, K. Walker, and Z. Wang, Phys. Rev. B **83**, 115132 (2011).

[17] M. Levin, F. J. Burnell, M. Koch-Janusz, and A. Stern, Phys. Rev. B **84**, 235145 (2011).

[18] J. Maciejko, X.-L. Qi, A. Karch, and S.-C. Zhang, Phys. Rev. Lett. **105**, 246809 (2010).

[19] B. Swingle, M. Barkeshli, J. McGreevy, and T. Senthil, Phys. Rev. B **83**, 195139 (2011).

[20] K. Walker and Z. Wang, Front. Phys. **7**, 150 (2012).

[21] A. Hamma, P. Zanardi, and X.-G. Wen, Phys. Rev. B **72**, 035307 (2005).

[22] C. Castelnovo and C. Chamon, Phys. Rev. B **78**, 155120 (2008).

[23] S. B. Bravyi and A. Y. Kitaev, arXiv preprint quant-ph/9811052 (1998).

[24] A. Kitaev and L. Kong, Communications in Mathematical Physics **313**, 351 (2012).

[25] X.-G. Wen, Quantum Field Theory of Many-body Systems from the Origin of Sound to an Origin of Light and Electrons. Published in the United States by Oxford University Press Inc., New York, 2004. ISBN 019853094. **1**, (2004).

[26] F. A. Bais and J. K. Slingerland, Phys. Rev. B **79**, 045316 (2009).

[27] Z. Wang, *Topological Quantum Computation*, *Conference Board of the Mathematical Sciences. CBMS regional conference series in mathematics* (American Mathematical Soc., ADDRESS, 2010).

[28] P.H. Bonderson, Ph.D. thesis, California Institute of Technology, 2007.

[29] A. Sikora, Ser. Knots Everything **24**, 436 .

[30] G. Moore and N. Read, Nuclear Physics B **360**, 362 (1991).

[31] E. Fradkin and S. H. Shenker, Phys. Rev. D **19**, 3682 (1979).

[32] M. d. W. Propitius and F. A. Bais, arXiv preprint hep-th/9511201 (1995).

[33] A. P. Schnyder, S. Ryu, A. Furusaki, and A. W. Ludwig, Physical Review B **78**, 195125 (2008).

[34] J. Maciejko, V. Chua, and G. A. Fiete, Phys. Rev. Lett. **112**, 016404 (2014).

[35] X.-L. Qi and S.-C. Zhang, Reviews of Modern Physics **83**, 1057 (2011).

[36] X. Chen, Z.-C. Gu, Z.-X. Liu, and X.-G. Wen, Phys. Rev. B **87**, 155114 (2013).

[37] A. Vishwanath and T. Senthil, Phys. Rev. X **3**, 011016 (2013).

[38] C. Wang and T. Senthil, Phys. Rev. B **87**, 235122 (2013).

[39] X. Chen, Y.-M. Lu, and A. Vishwanath, Nat Commun **5**, 4507 (2014).

[40] L. Fidkowski, X. Chen, and A. Vishwanath, Phys. Rev. X **3**, 041016 (2013).

[41] F. Burnell, X. Chen, L. Fidkowski, and A. Vishwanath, arXiv preprint arXiv:1302.7072 (2013).

[42] X. Chen, F. J. Burnell, A. Vishwanath, and L. Fidkowski, arXiv preprint arXiv:1403.6491 (2014).

[43] A. Kapustin and R. Thorngren, arXiv preprint arXiv:1308.2926 (2013).

[44] A. Kapustin and R. Thorngren, arXiv preprint arXiv:1309.4721 (2013).

[45] X. Chen, Z.-C. Gu, Z.-X. Liu, and X.-G. Wen, Phys. Rev. B **87**, 155114 (2013).

[46] M. A. Metlitski, C. L. Kane, and M. P. A. Fisher, Phys. Rev. B **88**, 035131 (2013).

[47] C. Xu and T. Senthil, Phys. Rev. B **87**, 174412 (2013).

[48] S. Gukov and A. Kapustin, arXiv preprint arXiv:1307.4793 (2013).

[49] J. L. Cardy and E. Rabinovici, Nuclear Physics B **205**, 1 (1982).

[50] J. L. Cardy, Nuclear Physics B **205**, 17 (1982).

[51] C. C. Jr., R. Dashen, and D. Gross, Physics Letters B **63**, 334 (1976).

[52] R. Jackiw and C. Rebbi, Phys. Rev. Lett. **37**, 172 (1976).

[53] X.-L. Qi, T. L. Hughes, and S.-C. Zhang, Phys. Rev. B **78**, 195424 (2008).

[54] A. S. Goldhaber, Phys. Rev. Lett. **36**, 1122 (1976).

[55] T. H. Hansson, V. Oganesyan, and S. L. Sondhi, Annals of Physics **313**, 497 (2004).

[56] A. M. Polyakov, Physics Letters B **59**, 82 (1975).

[57] C.-H. Lin and M. Levin, arXiv preprint arXiv:1402.4081 (2014).

[58] J. E. Avron, R. Seiler, and P. G. Zograf, Phys. Rev. Lett. **75**, 697 (1995).

[59] C. L. Kane and M. P. A. Fisher, Phys. Rev. B **55**, 15832 (1997).

[60] E. Witten, Communications in Mathematical Physics **121**, 351 (1989).

[61] A. Gromov and A. G. Abanov, arXiv preprint arXiv:1403.5809 (2014).

[62] S. Morampudi, C. W. von Keyserlingk, and F. Pollmann, arXiv preprint arXiv:1403.0768 (2014).

[63] C. Castelnovo and C. Chamon, Phys. Rev. B **77**, 054433 (2008).